

High Resolution Force Measurement System for Lorentz Force Velocimetry

Dissertation

zur Erlangung des akademischen Grades

Doktoringenieur (Dr.-Ing.)

vorgelegt der

Fakultät für Maschinenbau

der Technischen Universität Ilmenau

von Frau

M.Sc. Na Yan

geboren am 11.08.1988 in Heilongjiang, China

Gutachter: Herr Univ.-Prof. Dr.-Ing. habil. Thomas Fröhlich, TU Ilmenau
Herr Univ.-Prof. Dr.-Ing. habil. Eberhard Manske, TU Ilmenau
Frau Dr.-Ing. Dorothea Knopf, PTB Braunschweig

eingereicht am: 07.11.2018

verteidigt am: 26.02.2019

urn:nbn:de:gbv:ilm1-2019000068

Acknowledgments

At first I sincerely would like to express my thanks to Prof. Thomas Fröhlich for his encouragement and supervision. From him, I have learned the correct way to do scientific researches. Many thanks to Dr. Suren Vasilyan, Dr. Michael Kühnel, Dr. Ilko Rahneberg and Dr. Jan Schleichert for the discussions at the earlier stages of the work. I would like to thank Dr. Uwe Gerhardt for providing many electronic components. I am also grateful for my colleagues from the Institute of Process Measurement and Sensor Technology for providing me a supportive working environment for developing this thesis. The appreciation is also extended to Mathias Röser and Jürgen Bretschneider for their technical supports, to Helge Mammen, Vinzenz Ullmann, Norbert Rogge and Dr. Marc Schalles for lending me the devices. Without the people mentioned above, this work would never have been successfully finished within these three years.

Moreover, I would like to express my special appreciation to my parents (Xiulan and Peisheng) and all the family members (especially Bingyu and Kegong) for their support and guidance during all my life. Sincerely thanks to my husband Kuan for always being my strong backup since I started my work as a PhD student.

Additionally, I would like to thank everyone who have encouraged me, smiled to me after my talks and during the conferences...

Finally, I would like to express my thanks to my colleagues from the whole research training group "Lorentz Force Velocimetry and Lorentz Force Eddy Current Testing" supported by Deutsche Forschungsgemeinschaft (DFG).

Kurzfassung

Die Lorentzkraft-Anemometrie wurde als neuartige Methode für die berührungslose Geschwindigkeitsmessungen leitfähiger Strömungen entwickelt. Die induzierte Lorentzkraft ist proportional zur Strömungsgeschwindigkeit. Mit einem Kraftmesssystem kann die Reaktionskraft der induzierten Lorentzkraft, die auf das integrierte Magnetsystem wirkt, gemessen werden. Dadurch kann die Strömungsgeschwindigkeit bestimmt werden. Die Eigenschaften der Geschwindigkeitsmessung hängen von den Eigenschaften des Kraftmesssystems ab. Bei Fluiden mit geringer elektrischer Leitfähigkeit, wie z.B. Elektrolyten, liegt die erzeugte Lorentzkraft im Bereich von Mikronewton und darunter. Das Kraftmesssystem unterstützt eine Masse eines Magnetsystems von ca. 1 kg. Deshalb ist das Ziel dieser Arbeit ein Kraftmesssystem zu entwickeln, welches auf der einen Seite eine verbesserte Kraftauflösung in horizontaler Richtung für niedrigleitende Elektrolyte aufweist und auf der anderen Seite die Tragfähigkeit der Eigenlast von über 1 kg zur Unterstützung des integrierten Magnetsystems gewährleistet.

In vorherigen Arbeiten wurde die Wägezelle nach dem Prinzip der elektromagnetischen Kraftkompensation (EMK-Wägezelle) in aufgehängter Konfiguration mit dem 1 kg Magnetsystem zur Messung der Lorentzkraft verwendet. Basierend auf verschiedenen Experimenten in dieser vorgestellten Arbeit wird festgestellt, dass aufgrund des mechanischen Aufbaus sowohl Neigungsempfindlichkeit als auch Steifigkeit der EMK-Wägezelle stark von der genutzten Konfiguration und dem Gewicht der unterstützten Eigenlast abhängig sind. Um die durch diese Abhängigkeiten verursachten Einflüsse zu minimieren, wird ein Torsionskraftmesssystem basierend auf dem Prinzip der Torsionswaage entwickelt. Diese ist theoretisch neigungsunempfindlich und behält bei unterschiedlichen Eigenlasten eine konstante Steifigkeit bei.

Die Auslenkungsmessungen werden verwendet, um die Ausgangsspannung des Torsionskraftmesssystems sowohl in Positionswerten als auch in Kraftwerten zu kalibrieren. Ein Closed-Loop-Betriebsmodus wird mithilfe eines PID-Reglers aufgebaut, mit dem die Grenzfrequenz von 0,002 Hz auf 0,1 Hz verbessert wird. Ein spezialanfertiger kapazitiver Aktor wird entwickelt, um eine rückführbare elektrostatische Kraft zu erzeugen, die anstelle der elektromagnetischen Kraft verwendet werden kann. Um die elektrostatische Kraft zu kalibrieren, werden drei Methoden genutzt: (a) durch Messung des Kapazitätsgradienten; (b) durch Vergleich mit einer elektromagnetischen Kraft und (c) durch Messung des induzierten Stroms in einem Velocity-Modus. Bei der Datenauswertung wird eine numerische Verarbeitung mit Newton-Polynominterpolation durchgeführt, um die thermischen und seismischen Störungen und Driften während der Messungen zu schätzen und zu korrigieren. Im Vergleich zu vorherigen Arbeiten, wo die Kraftauflösung auf 20 nN und die Eigenlast auf 3 kg begrenzt waren, ist das Torsionskraftmesssystem in der Lage, Kräfte bis zu 2 nN aufzulösen und eine Eigenlast bis zu 10 kg zu tragen.

Schließlich wird die sogenannte Halb-Trocken-Kalibrierung am Torsionskraftmesssystem durchgeführt. Die Messempfindlichkeit wird für unterschiedliche Leitfähigkeiten ermittelt. Basierend auf den experimentellen Ergebnissen, zeigt das Torsionskraftmesssystem das Potential, um Messungen mit weiter geringerer Leitfähigkeit bis hinunter zu 0.0064 S m^{-1} durchzuführen.

Abstract

The Lorentz force velocimetry (LFV) was introduced as a novel method for non-contact velocity measurements of electrically conducting flows. The induced Lorentz force is proportional to the flow velocity. Using the force measurement system (FMS), the reaction force of the induced Lorentz force that acts on the integrated magnet system can be measured, the velocity of the moving flow can be thereby determined. The characteristics of the measured flow velocity depend on the properties of the FMS. For weakly electrically conducting fluids like electrolytes, the induced Lorentz force is in the range of micronewton and below. The mass of the magnet system supported by the FMS is approximately 1 kg. Therefore, the aim of this work is to develop a FMS with the improved force resolution in horizontal direction for weakly conducting electrolytes, and also with the dead load capacity of over 1 kg for supporting the integrated magnet system.

In previously developed FMSs, the electromagnetic force compensation (EMFC) weighing cell was used in its suspended configuration carrying the 1 kg magnet system to measure the Lorentz force. Based on various experiments in the presented work, it is found that due to its mechanical structure, the tilt sensitivity and the stiffness of the EMFC system are strongly dependent from the configuration it is used and the weight of dead load it supports. In order to minimize the influences caused by the dependency, the torsion force measurement system (TFMS), which is theoretically tilt-insensitive as well as retains a constant stiffness with different applied dead load values, is developed in this work based on the principle of torsion balance.

The deflection measurement as a traceable method is introduced to calibrate the output of the TFMS into positioning as well as force values. The closed-loop operation mode is built based on PID-controller, by which the cutoff frequency is improved from lower than 0.002 Hz to 0.1 Hz. A customized capacitive actuator is set up to create traceable electrostatic force (ESF), which is a reasonable replacement of the electromagnetic force (EMF). Then, the ESF is calibrated using three methods: (a) by measuring capacitance gradient; (b) by comparing with the EMF and (c) by measuring the induced current in a velocity mode. Numerical processing using Newton's polynomial interpolation is carried out in the data evaluation to estimate and compensate the thermal and seismic drifts during the measurements. In comparison with previous work where the force measurement resolution was limited to 20 nN and dead load up to 3 kg, the TFMS is able to resolve forces down to 2 nN and also makes it possible to carry the dead load up to 10 kg.

Finally, the so-called semi-dry calibration is carried out on the TFMS. The measuring sensitivity is obtained in respect to different conductivity values. Based on the experimental results, the TFMS shows a potential to implement velocity measurements with further lower conductivity down to 0.0064 S m^{-1} .

Contents

- 1. Introduction 1
 - 1.1 Lorentz Force Velocimetry..... 1
 - 1.2 State-of-the-Art of the FMSs..... 2
 - 1.2.1 Background 2
 - 1.2.2 FMSs developed for Lorentz force velocimetry 6
 - 1.3 Summary and scope of the work 8
- 2. Investigation on the EMFC weighing cell..... 10
 - 2.1 Tilt sensitivity of the EMFC weighing cell 11
 - 2.2 Stiffness of the EMFC weighing cell 18
 - 2.3 Summary 24
- 3. Design concept of torsion force measurement system 26
 - 3.1 Initial idea and theoretical calculation..... 26
 - 3.2 Plane wheel with dead load 29
 - 3.3 Flexible bearing support..... 29
 - 3.3.1 Flexible bearing hinge 29
 - 3.3.2 Conical coupling..... 30
 - 3.4 Positioning sensor..... 31
 - 3.5 Adjustment and safety components..... 33
 - 3.6 Summary 33
- 4. TFMS in the open-loop operation mode 35
 - 4.1 Position calibration using deflection method 35
 - 4.1.1 Force/ motion actuation using deflection method 36
 - 4.1.2 Experimental facility 37
 - 4.1.3 Measurements..... 38
 - 4.2 Force calibration using deflection method 40
 - 4.2.1 Adjustment of the tilt sensitivity 40
 - 4.2.2 Force calibration..... 42

4.2.3	Uncertainty discussion.....	45
4.3	System identification.....	46
4.4	Summary	48
5.	TFMS in the closed-loop operation mode	50
5.1	Setting up PID-controller using electromagnetic force	51
5.2	Setting up electrostatic force generator	55
5.3	Calibration of electrostatic force	57
5.3.1	Three methods to calibrate the electrostatic force	58
5.3.2	Discussion and uncertainty budget.....	62
5.4	Test of the dynamic behavior	64
5.5	Test of force resolution.....	66
5.6	Summary	69
6.	Lorentz force measurement	72
6.1	Experimental facility	72
6.2	Semi-dry calibration of the TFMS	75
6.3	Summary	79
7.	Conclusions and Outlook	81
	Appendix A Calibration of the NI9239	85
	Appendix B Geometrical parameters	86
	Bibliography.....	88
	Erklärung.....	93

Nomenclature

Acronyms

AFM	Atomic Force Microscopy
COG	Center of Gravity
DFMS	Differential Force Measurement System
EFB	Electrostatic Force Balance
ESF	Electrostatic Force
EMF	Electromagnetic Force
EMFC	Electromagnetic Force Compensation
FMS	Force Measurement System
HTS	High-Temperature Superconducting
LFV	Lorentz Force Velocimetry
NPI	Newton's Polynomial Interpolation
PCB	Printed Circuit Board
PFMS	Pendulum Force Measurement System
PP	Pivot Point
TFMS	Torsion Force Measurement System

Variables

F_L	[N]	Lorentz force
F_L'	[N]	Reaction force of the Lorentz force
σ	[S m ⁻¹]	Electrical conductivity
v	[m s ⁻¹]	Flow velocity
B	[T]	Magnetic flux density
F_m	[N]	Deadweight force
F_c	[N]	Compensation force

I_c	[A]	Compensation current
l	[m]	Length of the coil wire
F_a	[N]	Actuation force
F_t	[N]	Tilt force
F_{es}	[N]	Electrostatic force
F_{em}	[N]	Electromagnetic force

EMFC

m_1	[kg]	Deadweight at the position of weighing pan of the EMFC weighing cell
m_2	[kg]	Deadweight at the position of counterweight of the EMFC weighing cell
Δm	[kg]	Additionally applied mass on the weighing cell
α	[rad]	Tilt angle of the system
L_1	[m]	Arm length of the deadweight m_1
L_2	[m]	Arm length of the deadweight m_2
γ	[rad]	Misalignment angle of the EMFC on the tilt stage
L_s	[m]	Distance between the pivot and positioning sensor
L_m	[m]	Distance between the pivot and the voice coil actuator
s	[m]	Linear displacement at the positioning sensor
β	[rad]	Angular deflection of the lever arm
M_s	[N m]	Torque caused by the spring constant of the weighing cell C_p and the angular deflection β
C_s	[N m ⁻¹]	Linear stiffness of the weighing cell
C_r	[N rad ⁻¹]	Rotational stiffness of the weighing cell
C_p	[N m rad ⁻¹]	Spring constant of the mechanical structure of the weighing cell

TFMS

L_{T1}	[m]	Distance between the rotational axis and the non-magnetic dummy
L_{T2}	[m]	Distance between the rotational axis and the magnet system (or replacement dummy)

R	[m]	Distance between the rotational axis and the positioning sensor
C_i	[N m ⁻¹]	Effective stiffness of the TFMS for measuring Lorentz force
C_b	[N m rad ⁻¹]	Spring constant of the commercial flexible bearing hinge
f_n	[Hz]	Undamped natural frequency
J	[kg m ²]	The moment of inertia
θ	[rad]	Rotational angle of the TFMS
U_P	[V]	Output voltage of positioning sensor
K_{ps}	[rad V ⁻¹]	Position calibration factor
L_x	[m]	Displacement of COG from the PP in x -direction
L_y	[m]	Displacement of COG from the PP in y -direction
α_x	[rad]	Tilt angle around x -axis
α_y	[rad]	Tilt angle around y -axis
M_t	[N m]	Torque caused by the tilt sensitivity
T_x	[rad rad ⁻¹]	Tilt sensitivity around x -axis
T_y	[rad rad ⁻¹]	Tilt sensitivity around y -axis
K_m	[N m V ⁻¹]	Convert factor transferring the voltage value into torque value
K_F	[N V ⁻¹]	Force calibration factor
T_P	[s]	Peak time
ζ	--	Damping ratio
ω_n	[rad s ⁻¹]	Undamped natural frequency (angular)
ω_d	[rad s ⁻¹]	Damped natural frequency (angular)
τ	[s]	Settling time
U_{P0}	[V]	Defined voltage value, given in the PID-controller, used to define the null position of the plane wheel
K_{vc}	[N A ⁻¹]	Force constant of the commercial voice coil actuator
K_{es}	[N V ⁻²]	Calibration factor of electrostatic force
U_a	[V]	Actuation voltage across the two electrodes of the customized capacitor
A	[mm ²]	Effective cross section area of the capacitor
C	[pF]	Capacitance value
d_x	[μ m]	Distance between the two electrodes of the customized capacitor
d_0	[μ m]	Distance between the two electrodes of the customized capacitor when $U_{P0} = 0$

d_s	[μm]	Change of the distance between the two electrodes of the customized capacitor
\dot{d}_s	[$\mu\text{m s}^{-1}$]	Moving velocity of one electrode of the customized capacitor
U_{a0}	[V]	Pre-voltage supplied across the customized capacitive actuator
D_a	[mm]	Diameter of the annular pipe

1. Introduction

In this chapter, the principle and application of the Lorentz Force Velocimetry (LFV) are introduced briefly in section 1.1. In section 1.2, systems showing the state-of-the-art in force metrology are presented and several other related force measurement systems (FMSs) developed especially for the LFV are reviewed. In section 1.3, the scope of the work presented in the thesis is demonstrated.

1.1 Lorentz Force Velocimetry

The Lorentz Force Velocimetry (LFV) has been introduced in many works [1-8] as a non-contact technique to measure the mean flow velocity of electrically conducting fluid flows. Compared to optical, magneto-inductive and ultrasound techniques of flowmeters, the LFV as a contactless method is more desirable for applications in cases when the pipes are opaque and hot and/or the fluids are aggressive. The LFV setup is made up of three main parts as illustrated with the simplified principle sketch in figure 1.1, they are: ① flow channel with moving conducting fluid inside, the mean flow velocity v is expected to be determined; ② magnet system to generate the required magnetic field over the channel and ③ force measurement system (FMS) carrying the magnet system and measuring the reaction force of the induced Lorentz force. The channel is exposed in the magnetic field with the magnetic flux density B . In the channel moves the conducting fluid with velocity v and electrical conductivity σ across magnetic field lines. The interaction of the magnetic field with the induced eddy current leads to the braking force F_L in the direction to slow down the motion of the fluid. The force F_L is proportional to the velocity v , the electrical conductivity σ and the second power of the magnetic flux density B^2 , and can be described with the equation (1.1) as introduced in [1].

$$F_L = c \cdot \sigma \cdot v \cdot B^2 = K \cdot v \quad (1.1)$$

The factor c is a constant which depends on the geometry of the magnet system and the geometry of the flow. According to the Newton's Third Law, a force equals to the braking force F_L acting in the opposite direction is generated upon the magnet system. As illustrated in figure 1.1, the reaction force F_L' can be detected by the FMS. When the factor K in equation (1.1) is known, namely, after the system is calibrated with known velocity values, the flow velocity v can be obtained by the measured force from FMS. Moreover, this principle presented by equation (1.1) can also be applied in testing defects in materials by measuring conductivity σ when the velocity is a constant value [9].

The focus of this work is to develop the FMS to improve the Lorentz force measurement with electrolytes, whose electrical conductivity are in the range of 10^{-6} S m⁻¹ to 10^2 S m⁻¹. The currently used magnet system is a Halbach-array with the mass of approximately 1 kg causing the deadweight force of approximately 10 N [10]. The flow velocity in practical application is lower than 5 m s⁻¹ with the magnetic field up to 1.5 T [2, 7, 11]. Thus, the induced Lorentz force is approximately in the range of micronewton and below. Hence, the aim of this work is to improve the force resolution of the FMS

in horizontal direction in order to perform measurement with electrolytes, and maintain the dead load capacity of over 1 kg for carrying the unavoidable dead load caused by the magnet system.

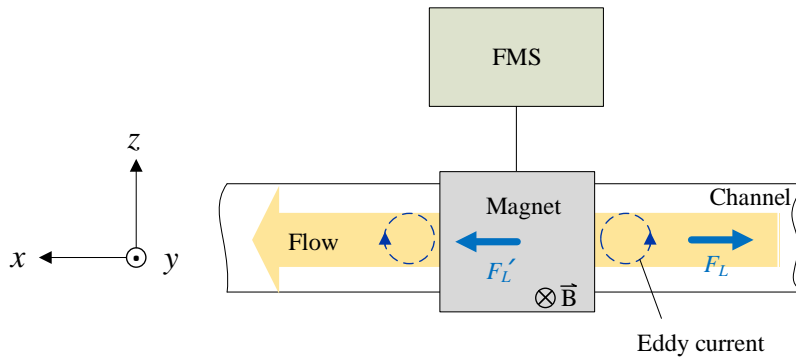


Figure 1.1: Simplified principle sketch of Lorentz Force Velocimetry with integrated channel, magnet system and FMS (side view).

1.2 State-of-the-Art of the FMSs

1.2.1 Background

Nowadays growing trend for measurement and calibration of small forces is in the field of nanotechnology and nanometrology [12]. Apart from the LFV framework, the investigations of the force in micro- and nanonewton are also being in the active focus of most of the national metrological institutes (NMIs). In this section several FMSs related closely to this work and showing the state-of-the-art are introduced.

Force is one of the derived units in the International System of Units (SI Units), using the combination of base SI units of mass ([kg]) and local gravity ([m] and [s]). At present the unit of mass is defined by the artefact international prototype of kilogram (IPK), which is conserved at the International Bureau of Weights and Measures (BIPM) since 1889. In comparisons with the IPK through a hierarchical system, the unit of mass is disseminated throughout the world to NMIs, to laboratories, to industries, to instruments and sensors, as well as to trades. Multiples and submultiples of one kilogram are also realized by artefacts manufactured in different shapes and sizes, which are well known as mass standards. By using mass standards, deadweight forces can be created and calibration measurements can be performed on different type of sensors. However, there is a limit for providing small forces using deadweight force such as the traceable mass artefact in the US National Institute of Standard and Technology (NIST) is down to 0.5 mg corresponding to approximately $5 \mu\text{N}$ [12], which is still three orders of magnitude larger than the demand for measuring and calibration of forces in nanonewtons. Thus, systems are being developed in most NMIs for realization and measuring small force values.

a) Electrostatic force balance

In 2003, NIST reported on the realization of micro force below $5 \mu\text{N}$ using electrostatic force balance (EFB), by which the comparison between mechanically and electrically divided forces up to $300 \mu\text{N}$ with the resolution of 15 nN is possible [13]. In 2016, with the same principle of the EFB, NIST

reported force resolution on the order of piconewtons [14]. The National Physical Laboratory in UK (NPL) designed a primary low force balance via electrical and dimensional measurements and achieved the resolution of 50 pN [15]. The mechanical structures of EFB facilities differ from each application but the main parts remain similar as illustrated in figure 1.2. The parallelogram balance structure (1) carries the inner cylinder electrode (3), to which the outer cylinder electrode (4) is aligned coaxially. As the inner electrode is free to translate together with the parallelogram mechanism along z -axis, while the outer electrode is fixed rigidly on the base frame, the overlap of the two electrodes varies and leads to the electrostatic force F_{es} with the voltage U applied across the two electrodes, as equation (1.2) shows:

$$F_{es} = \frac{1}{2} \cdot \frac{dC}{dz} \cdot U^2 = K_{es} \cdot U^2 \quad (1.2)$$

dC/dz indicates the capacitance gradient. When the two cylindrical electrodes are perfectly aligned coaxially, the capacitance C is linear to the overlap by using this kind of geometrical structure, which indicates that the capacitance gradient is a constant value and is described by K_{es} as the constant force factor.

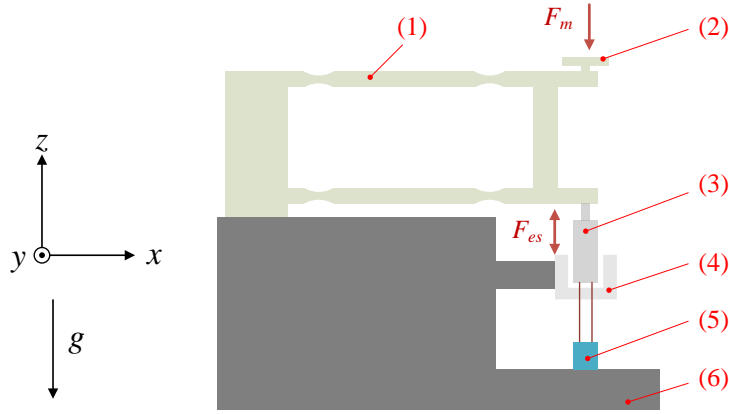


Figure 1.2: Schematic of electrostatic force balance components: (1) Parallelogram balance mechanism; (2) Mass/load pan; (3) Inner cylindrical electrode (cross section); (4) Outer cylindrical electrode (cross section); (5) Interferometer for measuring displacement and (6) base frame. The structure is drawn according to the facilities described in [14-15].

The EFB operates with null balance principle. Deadweight forces F_m acting on the mass/load pan (2) causes the displacement of the inner electrode, which can be detected by the interferometer (5). Due to this displacement, the voltage value U across the two electrodes is able to be calculated and applied to the capacitor to generate the electrostatic force F_{es} compensating F_m and maintaining the balance at its null position. Thus, the electrostatic force between the two electrodes indicates the force F_m as described by equation (1.3), where m is the applied mass causing deadweight force, g is the local gravitational acceleration, U_N and U_L indicate the required electrical voltage to maintain the balance at null position before and after loading respectively.

$$F_m = m \cdot g = F_{es} = K_{es} \cdot (U_L^2 - U_N^2) \quad (1.3)$$

Base on the common structure, derived setups were developed to adapt to local conditions. In [16], an auxiliary capacitor is assembled on the parallelogram linkage for controlling the motion of the balance during measuring the capacitance gradient of the main capacitor. Instead of using inner and outer cylindrical electrodes, plate-shaped electrodes are used in [17] which enables actuate electrostatic force as well as sense deflection with one structure. While the cylindrical capacitor is kept, the parallelogram balance mechanism is replaced by a high-sensitive lever mechanism with torsion rod in [18] to decrease the stiffness of the system.

b) Electromagnetic force compensation balance

Besides the investigations in the NIMs and other metrological institutes, the technique of small force measurements is also continuously being developed in industries. The commercial electromagnetic force compensation (EMFC) balances are based on the weighing cell illustrated in figure 1.3 with monolithic parallelogram mechanism (2) and operate with null balance principle.

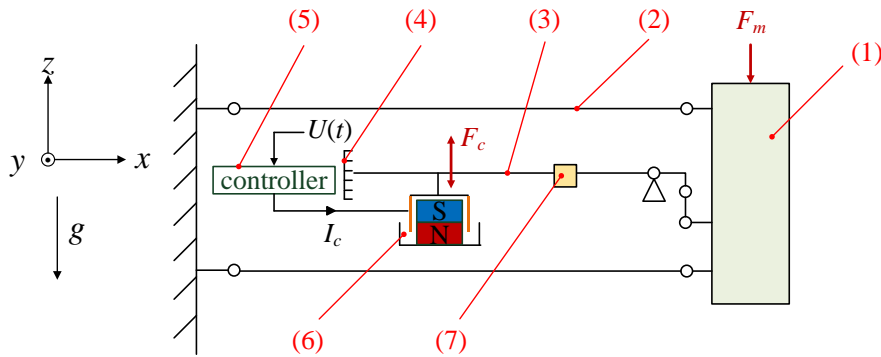


Figure 1.3: Schematic of EMFC weighing cell: (1) Mass/load pan; (2) Parallelogram mechanism with elliptical notch flexures; (3) Transmission lever; (4) Optical positioning sensor; (5) Control system; (6) Electromagnetic actuator; (7) Counterweight.

The deadweight force F_m of the object acts on the load pan (1) and causes the deflection of the transmission lever (3). The movement of the lever is continuously recorded by the positioning sensor (4) with the output voltage $U(t)$. To compensate the deflection, the compensation current I_c is calculated by the controller due to $U(t)$ and then transferred to the coil wire of the electromagnetic actuator (6) to generate the electromagnetic force F_c due to equation (1.4). The electromagnetic force as the compensation force brings the transmission lever back to the null position. l and B indicate the length of the coil wire and the magnetic flux density of the electromagnetic actuator.

$$F_c = I_c \cdot l \cdot B \quad (1.4)$$

Using this principle, the ultra-micro EMFC balances developed in *Sartorius Lab Instrument GmbH* can reach a readability of $0.1 \mu\text{g}$, roughly corresponding to forces of $< 1 \text{ nN}$, at a weighing capacity of 2 g . Apart from comparing with deadweight force as a balance, the EMFC weighing cell is also used in combination with other high-precision mechanisms for other applications. In the National Metrology Institute of Germany (PTB) and Korea (KRISS), piezo actuator deflects the cantilever on

the EMFC weighing cell to determine the stiffness of the cantilever used in atomic force microscopy (AFM) [17]. Another similar mode was also carried out in technical university of Ilmenau: instead of moving the cantilever with the piezo actuator, the load pan is set into controllable motion by the internal voice coil actuator and probes the fixed cantilever. With the deflection measured by interferometer and the force measured by the weighing cell, the stiffness can be ascertained [19]. As a derived application utilizing the tilt sensitivity of the EMFC weighing cell, an inclinometer was developed with the standard deviation of the angle of $3.4 \text{ nrad} \sim 7.1 \text{ nrad}$ depending on the used filter [20].

Although the electrostatic force and electromagnetic force are introduced above with the facilities to measure vertical directed deadweight forces, actuation forces in other directions can also be induced using the principle indicated in equation (1.2) and (1.4), such as forces in the horizontal plane are applied on the system developed in this work. The performance of the electrostatic- and electromagnetic forces related to this work is further described in chapter 5.

Apart from measuring deadweight forces, horizontally directed forces are also under investigation in several metrological institutes. Similar to the facilities introduced above, the horizontal forces are also determined by detecting the displacement caused by external forces using optical metrology. Common mechanisms to enable the displacement in horizontal plane are torsion balance and suspended pendulum.

c) Torsion balance

The concept of torsion balance is well known as the experiment was carried out by Henry Cavendish in 1798 to measure the gravitational force between two masses. Nowadays the mechanisms based on torsion balance principle are still widely used with the aim to improve the uncertainty of the gravitational constant G . At BIPM the apparatus was designed with four source masses, each of which weights approximately 11 kg and four test masses each of which weights approximately 1.2 kg on a torsion disc suspended by a wide torsion strip [21]. The deflection of the test masses is recorded by autocollimators, by which the achieved uncertainty is 25 ppm in the measured G [21]. Similar facility was introduced in [22] where only two test masses and two source masses were used. In that work two methods for generating horizontally directed forces were used, namely, using radiation pressure for generating optical force with maximum force of 10 nN and using capacitive actuator for generating electrostatic force in the range of $\pm 50 \text{ nN}$. In the PhD work of Wagner [23], a rotating torsion balance was used to test the weak equivalence principle. Based on the torsion balance principle, a FMS is developed in this work and is further introduced in chapter 3.

d) Suspended pendulum

Besides of using torsion balance, the gravitational constant G can also be determined using beam balance with an achieved uncertainty of 32.8 ppm [24] or using the pendulum mechanism. In [25] two bobs made of oxygen-free copper as test masses (each 780 g) are suspended with four wires. Four source masses can move to the outer position and inner position with the help of air bearings. As a result, the change of gravitational force on each test masse of 480 nN leads to the separation change, which is detected by the Fabry-Perot interferometer [25]. Using the laser interferometric measurement and such pendulum, the uncertainty of 15 ppm in the measured G value was obtained.

At PTB, a nanonewton force facility with two identical disc-pendulums was introduced, one of which measures the target force and the other one works as the reference to measure and compensate the errors caused by thermal drift/tilt and seismic noise. Using electrostatic force as compensation force, the facility in PTB can measure the force of 1 nN with the measurement uncertainty of 5% [26].

The introduction above is not a full illustration of all systems indicating the state-of-the-art FMSs in small force metrology. There are other high-resolution facilities and researches such as AFM and investigations based on photon pressure forces.

The setups and force measurement principles introduced above are related closely to the FMSs which have been designed for the Lorentz force measurement in the LFV application, later in section 1.2.2 they will be introduced.

1.2.2 FMSs developed for Lorentz force velocimetry

As introduced in section 1.1, to adapt to the LFV application, the FMSs have been continuously developed and improved in the last several years with the following main requirements:

- a) Force measurement in horizontal plane;
- b) High resolution in the range of micro- and nanonewton;
- c) High capacity for supporting dead load of over 1 kg.

Initially in [1], the LFV was introduced with a focus on narrow field of application as in metallurgy, where the electrical conductivity of the fluid is on the order of 10^6 S m^{-1} and the measured Lorentz force is in the range of millinewton and newton. Then, the LFV was transformed into a universal flowmeter which is also applicable for weakly conductive liquids by improving the FMS as well as magnet system. In [3] the FMS was developed with the magnet system carried by a four-wire-suspension pendulum depicted in figure 1.4 (a). The magnet system consists of two identical NdFeB permanent magnets with a total mass of 1.286 kg, which is attached to the supporting frame by four tungsten wires with a diameter of 125 μm and length of 0.55 m. The displacement x of the magnet system caused by the force F_L' is measured by a laser interferometer. The force value can be calculated from the displacement by $F_L' = k \cdot x$, where k indicates the stiffness of the pendulum-FMS (PFMS) depending on the mass and length of the pendulum. Using this PFMS, experiments on salt water with electrical conductivity of 2.3 S m^{-1} , 4.0 S m^{-1} and 6.2 S m^{-1} were carried out, and the measurement results demonstrated agreement with the simulation.

Subsequently, a robust system was introduced by replacing the pendulum with a single commercial EMFC weighing cell (see figure 1.3) with its suspended configuration illustrated in figure 1.4 (b) [27]. The parallelogram mechanism of the EMFC weighing cell has a good effect to restrict the displacement of the magnet system along x -axis. With the EMFC weighing cell, measurements with both open-loop operation mode where force value is calculated from displacement similar to PFMS; and closed-loop operation mode where the displacement caused by the external force is compensated back to null position, can be carried out to measure the reaction force of the Lorentz force. The induced Lorentz forces generated by flows with velocity of $0 < v \leq 2.8 \text{ m s}^{-1}$ and electrical conductivity of $2 \leq \sigma \leq 6 \text{ S m}^{-1}$ were measured with the single EMFC system in combination with

conventional magnet system as well as magnets arranged in Halbach-arrays. The relative uncertainty in the measured force with both magnet systems is lower than $\pm 1\%$ (confidence level $k = 2$).

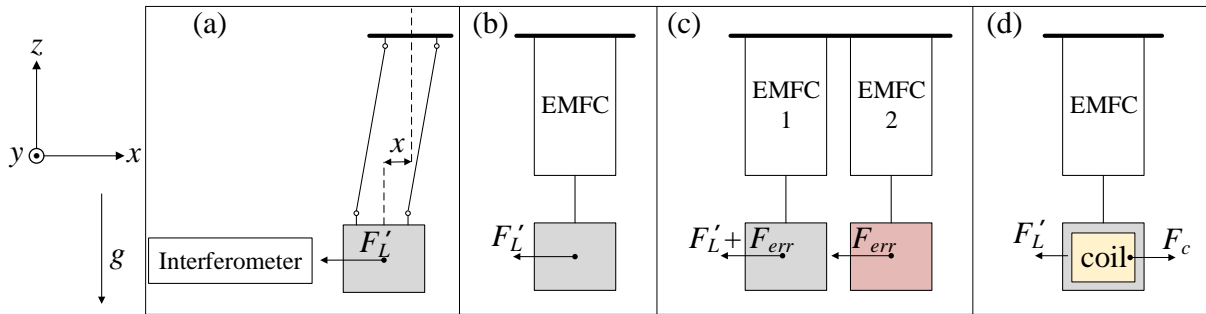


Figure 1.4: Sketch of the development of FMSs for LFV application. (a) Pendulum force measurement system with interferometer to measure displacement x ; (b) Single-EMFC system; (c) Differential FMS; (d) FMS based on direct compensation method.

When measuring the forces in the range of micronewton and below, the target signal can be distorted by the errors mainly caused by thermal drift/tilt and seismic noise. To compensate these errors in small force metrology, differential systems were introduced such as in [26] and [28]. As an advancement of single EMFC system, a second identical EMFC weighing cell was introduced to build up the differential force measurement system (DFMS) illustrated in figure 1.4 (c), aiming to compensate the errors in the measured signal [29]. The first EMFC weighing cell carries the magnet system while the second one supports a non-magnetic copper dummy with a similar weight as well as similar geometrical dimensions, both of which were carefully aligned and assembled on the same frame. As the flow moves in the channel, the measured signal of the second EMFC weighing cell indicates the undesired noise part F_{err} of the measured signal from the first EMFC weighing cell. The difference between them indicates the target force F_L' . By using the DFMS, the undesired errors in the measured signal was inhibited and the force resolution was improved from $1 \mu\text{N}$ to 20 nN in the working range of $\pm 100 \mu\text{N}$ [30]. The LFV based on the DFMS was used in practical measurements to detect Lorentz forces for flows with further extended conductivity down to 0.059 S m^{-1} , and the velocity remained in the similar range as 0.2 to 2.5 m s^{-1} [31].

A further development of the FMS is shown in figure 1.4 (d). By integrating the EMFC weighing cell in the LFV, two magnets work with different functions: the magnet supported by the weighing cell (LFV magnet) aims to generate the magnetic field around the channel and carry the force F_L' ; meanwhile, the magnet integrated inside the EMFC weighing cell (EMFC magnet) together with the voice coil is for providing the electromagnetic compensation force F_c . The improvement was concerning to combine the two functions upon one magnet system. The customized rectangular coil was assembled beside the LFV magnet, in this way by applying compensation current to this coil, the compensation force acts no more on the EMFC magnet but directly on the LFV magnet, which was introduced as direct compensation method [32]. The direct compensation method was also applied on the PFMS to enable the system work in the closed-loop operation mode. By using the direct compensation method, the force factor of the FMS can be increased by increasing the number of turns of the coil. However, no improvement in force resolution was observed as the resolution remains at

1 μN . For further improvement, the direct compensation method (figure 1.4 (d)) could be combined with DFMS (figure 1.4 (c)) to reduce the environmental noises.

1.3 Summary and scope of the work

In this chapter, the principle of the LFV as a non-contact method to measure mean velocity of conducting fluids has been briefly introduced. To perform the velocity measurement with weakly conducting fluids such as electrolyte, the improvement of force measurement resolution in horizontal direction as well as the capacity for supporting dead load was introduced as the focus of the work. The state-of-the-art FMSs developed and used in several research institutes as well as developments in industry were presented. The developments of FMSs for LFV application over the last two generations in our institute were reviewed and summarized with the table 1.1. With the resolution of 20 nN by using the DFMS, measurement on electrolyte with conductivity down to 0.059 S m^{-1} was achieved. Aiming to study the electrolyte with further lower conductivities, the force resolution is expected to be improved further.

As the scope of the work presented in the following sections, the investigation on the EMFC weighing cell is implemented to study the influences caused by different configurations and dead loads on the tilt sensitivity and stiffness of the system in:

Chapter 2: Investigation on the EMFC weighing cell

Based on the results achieved in chapter 2 and considering the mechanical structure of the EMFC weighing cell, a torsion force measurement system (TFMS) based on the principle of torsion balance is developed and introduced, with the aim to improve the force resolution by one order of magnitude, namely from 20 nN to 2 nN, then in the following chapters:

Chapter 3: Design concept of torsion force measurement system: the TFMS is constructed based on the theoretical calculation in respect to the target force resolution; components of the TFMS are introduced.

Chapter 4: TFMS in the open-loop operation mode: Deflection method is introduced as a traceable method for position calibration and force calibration; the system identification is performed to determine dynamic behavior of the TFMS in the open-loop operation mode.

Chapter 5: TFMS in the close-loop operation mode: Setting up the closed-loop operation mode for the TFMS with two different force actuation and compensation mechanisms; in the first case the small forces are produced electromagnetically using commercial voice coil actuator; in the second case electrostatic forces are generated using a customized plate-shaped capacitor. Calibration of the electrostatic force with three principles is introduced. Static and dynamic properties of the TFMS are tested.

Chapter 6: Lorentz force measurement: Practical measurements are carried out with magnet system and electrolytes; semi-dry calibration of the TFMS as the Lorentz force flowmeter is introduced, the sensitivity of velocity measurement is obtained in respect to different conductivity values.

Table 1.1: Summary of the FMSs developed in the previous researches for LFV, and the aims to be achieved with the TFMS developed in this work.

	PFMS	Single EMFC	DFMS	Direct Compensation	TFMS
Force resolution	2 μN	1 μN	20 nN	1 μN	\rightarrow 2 nN
Settling time	12 s	1.5 s	1.4 s	1.4 s	
Dead load capacity	1.286 kg	Approximately 1 kg; theoretically limited by 3 kg [27]			\rightarrow > 3 kg
Comments	Operates only in open-loop; Motion in y direction and rotation in xy plane could influence the measurements.	Motion is well restrained within x direction; Robust and portable; Resolution is restricted by errors caused by thermal and seismic noise.	Second identical EMFC for compensating errors caused by thermal and seismic noise.	PFMS can operate in close-loop; Force factor can be increased by increasing the number of turns of the coil; Without reference system the resolution remains at 1 μN .	
Measurement on electrolyte with conductivity down to	2.3 S m^{-1}	2.03 S m^{-1}	0.059 S m^{-1}	2.7 S m^{-1}	\rightarrow further lower

2. Investigation on the EMFC weighing cell

As mentioned in chapter 1, in the work of C. Diethold [27] and S. Vasilyan [29], single or two identical EMFC weighing cell/cells were used to measure the horizontally directed Lorentz force. As table 2.1 demonstrates, differing from its common usage as a balance, in the previously developed FMSs, the EMFC is adopted in its suspended configuration supporting a 1 kg magnet system as an unavoidable dead load. The work in this chapter aims to investigate the properties of the weighing cell, namely the tilt sensitivity in section 2.1 and the stiffness in section 2.2, in respect to the influence on the measurement caused by different configurations and different dead load values.

Table 2.1: Configurations and supported dead load values of the EMFC weighing cell in its common usage and in previously developed FMSs. Experiments are carried out in this chapter to study the effects on the tilt sensitivity and stiffness caused by different configurations and supported dead load values.

	Configuration	Supported dead load
Common usage as balance	Placed on a flat surface	none
In previous work [27, 30-32]	Suspended with weighing pan downwards	≈ 1 kg
In this work, experiments are carried out with	(a) Common usage	A set of dead load values -10 g ~ 40 g (positive value: dead load applied on weighing pan; negative value: dead load applied on counterweight)
	(b) Sidewise configuration	
	(c) Suspended with weighing pan upwards	
	(d) Suspended with weighing pan downwards	
Tilt sensitivity	Measurement uncertainty can be thereby increased	
Stiffness	Determining the measuring sensitivity of the system	

Effects on tilt sensitivity and stiffness caused by different configurations and dead load values are tested

2.1 Tilt sensitivity of the EMFC weighing cell

In comparison with the system using single EMFC weighing cell, by using a second identical weighing cell in the DFMS, the force resolution is improved from 1 μN to 20 nN by factor 50. This improvement is achieved by using a reference system to measure and compensate the errors caused by thermal drift/tilt and seismic noises which play a significant role in the small force measurement. In order to improve the force resolution, these errors are expected to be further investigated. The tilt/movement of the foundation, on which a FMS is placed, is a summation of factors caused by human activities, motion of machines nearby and the seismic activities of the earth, including earth tides [33]. Moreover, the thermal deformation of support frames leads to the tilt of the FMS. As an obvious outcome of the influences of tilt on the measurement, the tilt sensitivity of the EMFC weighing cell is discussed in this section.

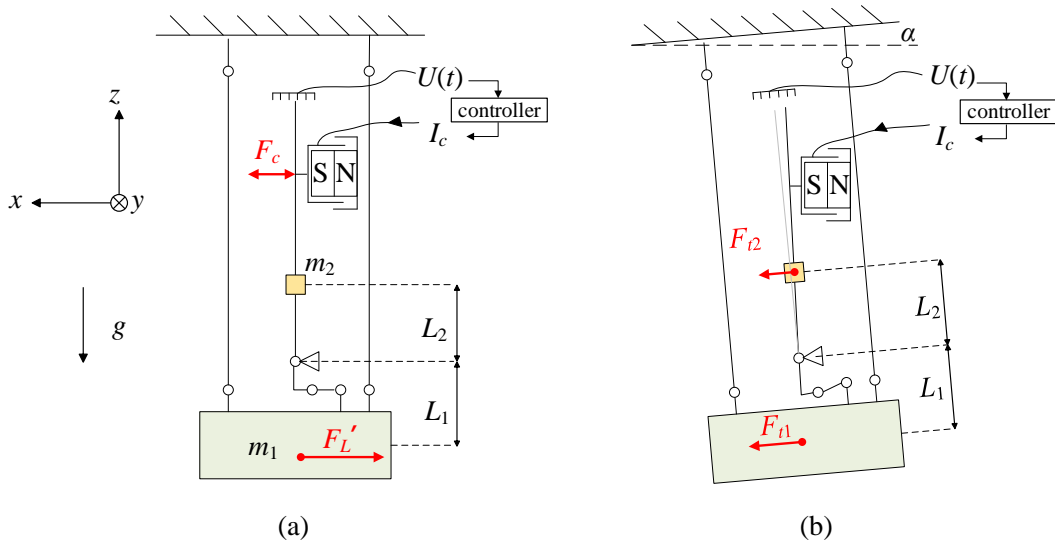


Figure 2.1: The EMFC weighing cell in its suspended configuration: a) In perfectly vertical aligned direction; b) Misaligned with a tilt angle α . The green block indicates the deadweight at the position of the weighing pan m_1 with arm length L_1 ; yellow block indicates the deadweight on the other side of the pivot m_2 with arm length L_2 . Positioning sensor gives voltage $U(t)$ to PID controller and current I_c is applied on the coil for the compensation procedure.

The EMFC weighing cell can be simply sketched as a lever arm with the deadweight at the position of the weighing pan m_1 on one side and m_2 as the counterweight on the other side [34]. In order to measure horizontally directed forces, the EMFC was configured in its suspended position in [27] and [29] as presented in figure 1.4. For an ideal case illustrated in figure 2.1 (a), external force F_L' acts on the weighing pan causing the deflection of the lever arm, which is detected by the positioning sensor giving the continuously measured voltage $U(t)$. Based on a PID-controller, compensation current I_c can be calculated concerning the lever's deflection and be transferred to the voice coil integrated in the weighing cell. With interaction between the coil and magnet, compensation force F_c is generated

against the external force and brings the lever arm back to the null position. In this way, the external force is measured by the compensation force F_c .

However, in real experimental situations, a perfectly aligned vertical configuration as shown in figure 2.1 (a) is difficult to achieve due to the causes of tilt discussed above. Assuming that between the horizontal plane and the frame of the weighing cell there is a tilt angle α illustrated in figure 2.1 (b), as a consequence, tilt forces F_{t1} and F_{t2} caused by deadweight force and the tilt angle will act on m_1 and m_2 respectively. Both tilt forces lead to the torque M_t described in equation (2.1):

$$F_{t1} = m_1 \cdot g \cdot \sin \alpha; F_{t2} = m_2 \cdot g \cdot \sin \alpha \text{ and } M_t = -F_{t1} \cdot L_1 + F_{t2} \cdot L_2 \quad (2.1)$$

When the parameters of the weighing cell do not fulfill the requirement indicated by equation (2.2), the torque M_t drives the lever arm to leave its equilibrium. The positioning sensor detects this displacement, which leads to the change in the output signal, even if no external forces act on the system. The measured force is thereby distorted.

$$M_t = -m_1 \cdot g \cdot \sin \alpha \cdot L_1 + m_2 \cdot g \cdot \sin \alpha \cdot L_2 = 0$$

$$\text{Namely,} \quad m_1 \cdot L_1 = m_2 \cdot L_2 \quad (2.2)$$

Based on equation (2.1) and (2.2), the error signal caused by torque M_t is proportional to sine of the tilt angle α and the value of $(-m_1 \cdot L_1 + m_2 \cdot L_2)$. Because that the weighing cell aims to measure force acting upon the weighing pan, the error signal is expressed in the form of force rather than torque. Therefore, this error signal is described by the tilt force F_t as denoted in equation (2.3).

$$F_t = \frac{M_t}{L_1} = \frac{(m_2 \cdot L_2 - m_1 \cdot L_1) \cdot g \cdot \sin \alpha}{L_1} \quad (2.3)$$

The relationship between the tilt force F_t and the tilt angle α is the tilt dependency of the system. As equation (2.3) indicates, the tilt force can be further amplified in the LFV application where the value of m_1 is enlarged by carrying the 1 kg magnet system.

To investigate how the tilt angle influence the measurement of the EMFC weighing cell with different configurations and dead load values, moreover, with the aim to find a way to minimize the influence caused by tilt, various experimental tests are carried out with the EMFC weighing cell located on a tilt stage. The tilt stage introduced in [35] is driven horizontally by two high precision linear motors in both x - and y -direction, with wedge-form combinations the horizontal movement can be transferred into vertical movement to actuate tilt angles with a resolution of down to 1 μrad in the range of ± 17.4 mrad. The weighing cell, fixed on the tilt stage using additional mechanical support, can be set into controllable stepwise tilt. Synchronously, the compensation force maintaining the lever arm at null position and describing the tilt force F_t is recorded. When the system does not fulfill the requirement of equation (2.2), according to equation (2.3) the tilt force F_t as the output signal from the weighing cell should also be in a stepwise form corresponding to the tilt angles. Although the weighing cell is not designed initially to satisfy equation (2.2) by the manufacturer, this can be

manually achieved by changing the value of m_1 and/or m_2 , which can be realized by adding mass pieces on the weighing pan or on the other side of the lever arm. In order to create a full picture of the tilt sensitivity, the EMFC weighing cell is placed in a set of experiments on the tilt stage in four different configurations as presented in the figure 2.2. Configuration (a) describes the common usage of the weighing cell as a balance while configuration (d) demonstrates the usage of the suspended weighing cell to measure the Lorentz force in previous work [27,29]. Configuration (b) and (c) indicate the rotation of the weighing cell around x -axis counterclockwise from configuration (d) by 90° and 180° respectively.

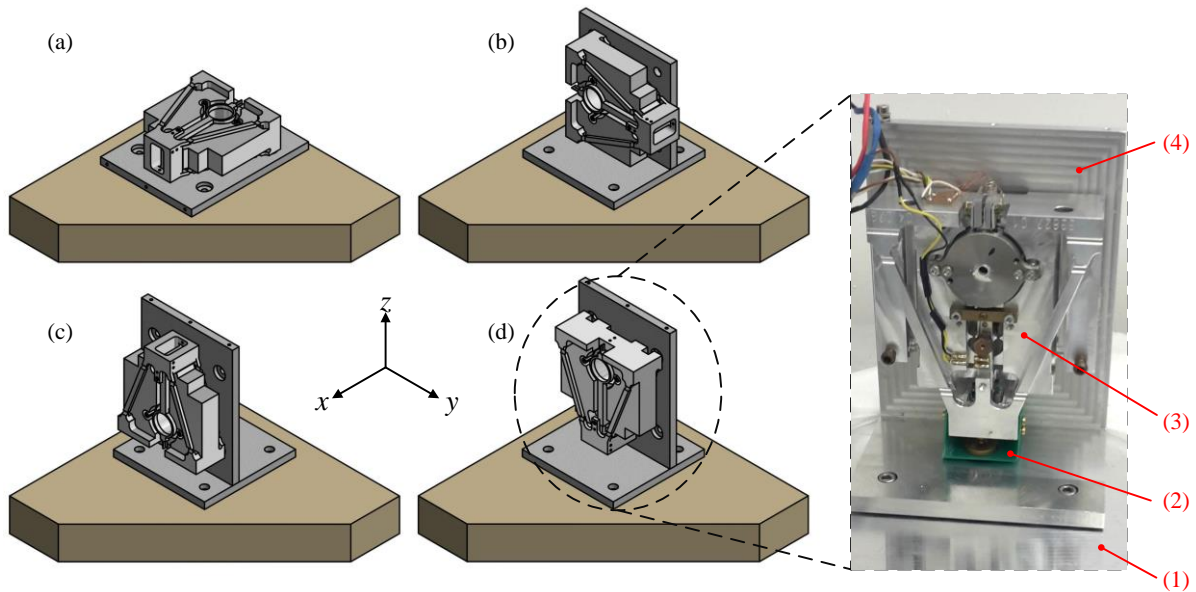


Figure 2.2: Four configurations to locate the EMFC weighing cell on the tilt stage. (a) Common configuration as a balance; (b) Sidewise configuration; (c) Suspended with weighing pan upwards, (d) Suspended with weighing pan downwards. (1) Tilt stage; (2) Assembled mass standard and its carrier; (3) EMFC weighing cell; (4) Mechanical support for fixing the weighing cell on the tilt stage.

The experiments are carried out as follows:

- (1) In each of the four configurations, different dead loads (mass pieces) are assembled to the EMFC weighing cell to change the value of m_1 or m_2 .
- (2) With each dead load value, the tilt sensitivity of the EMFC system is to be determined. The stepwise tilt angles in the range of ± 8 mrad are generated by the tilt stage around x - and then y -axis respectively. The resulted output signal is then recorded.

With the aims to:

- (1) Determine how the dead load affects the tilt sensitivity; and to find the value of the dead load, by which the tilt sensitivity is zero, namely, equation (2.2) is achieved.
- (2) Determine how the configuration affects the tilt sensitivity.

2. Investigation on the EMFC weighing cell

Experimental data of the measurements in configuration (d) is shown in figure 2.3 as an example. Each single line describes the dependency of the tilt forces on the tilt angles with each applied dead load in the range of 0 g to 52 g (in this experiment all the additional dead loads are applied on the weighing pan). With the same applied mass piece as the dead load, a tilt angle around y -axis leads to a significant higher output force than that caused by the same tilt angle around x . The monolithic parallelogram structure with the very fine elliptical notch flexures only enables the weighing cell rotate by its pivot around y -axis while the rotational freedom around x -axis is restricted. Theoretically, the system is thereby insensitive to the tilt around x -axis. The measured tilt dependency around x shown in the left figure of figure 2.3 is a consequence of misalignment, in which the coordinate of the weighing cell ($x'y'$) is not aligned perfectly to the coordinate of the tilt stage (xy). Although in the measurements the tilt is controlled by the tilt stage around its x -axis, tilt of the weighing cell still occurs around its sensitive axis y' when the weighing cell is misaligned from the tilt stage by an angle of γ as demonstrated in figure 2.4. Thereby the output of the weighing cell is also tilt dependent on the tilt around the x of the tilt stage. As γ is a minor angle by careful alignment, the measured tilt dependency around x -axis is much lower than that around y -axis corresponding to the figure 2.3.

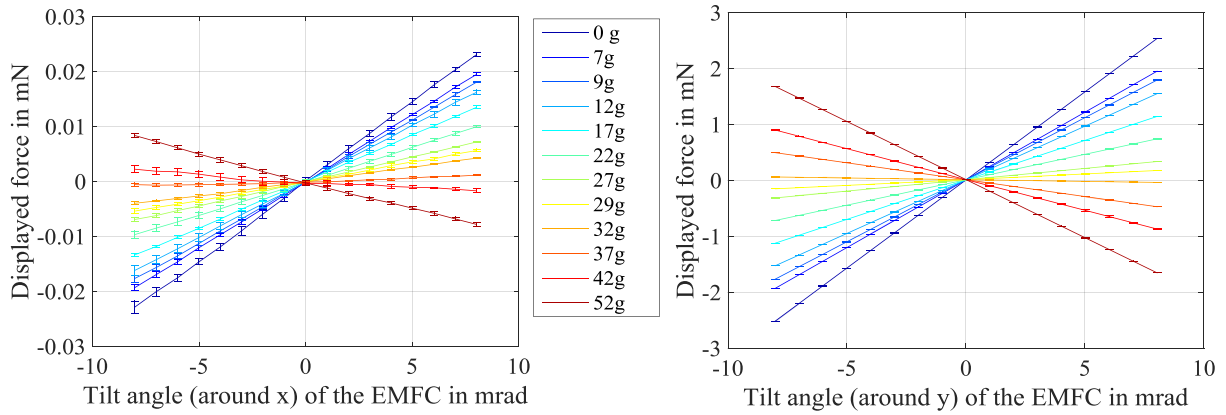


Figure 2.3: Tilt dependency of the EMFC weighing cell: output forces against tilt angles around x -axis (left figure) and around y -axis (right figure) by applying different dead loads. The value of the dead load presented in the middle is the summation of the mass of applied mass piece and its carrier.

By comparing the measured data while the tilt stage tilts around its x - and y -axis, the angle of the misalignment γ can be estimated and correction can be added on the measured data with equation (2.4) and (2.5):

$$P'_1 = P_1 \cdot \cos \gamma - P_2 \cdot \sin \gamma \quad (2.4)$$

$$P'_2 = P_1 \cdot \sin \gamma + P_2 \cdot \cos \gamma \quad (2.5)$$

P_1 - In the perfectly aligned case ($\gamma = 0$), output of the weighing cell with tilt stage tilting around x ;

P_2 - In the perfectly aligned case ($\gamma = 0$), output of the weighing cell with tilt stage tilting around y ;

P_1' - In real case when $\gamma \neq 0$, measured output of the weighing cell with tilt stage tilting around x ;

P_2' - In real case when $\gamma \neq 0$, measured output of the weighing cell with tilt stage tilting around y .

As described above, due to its mechanical structure, the weighing cell is insensitive to the tilt around x -axis when $\gamma = 0$, thereby value P_1 is zero and the equation (2.4) and (2.5) can be simplified as equation (2.6). The misalignment angle γ can be calculated with the measured data in the real case, thus γ is calculated as $0.5270 \pm 0.0065^\circ$ (confidence level $k = 2$), by which the measured output P_1' and P_2' are corrected due to equation (2.6) to determine the theoretical output P_1 and P_2 in perfectly aligned case.

$$P_1' = -P_2 \cdot \sin \gamma; P_2' = P_2 \cdot \cos \gamma; \tan \gamma = -\frac{P_1'}{P_2'} \quad (2.6)$$

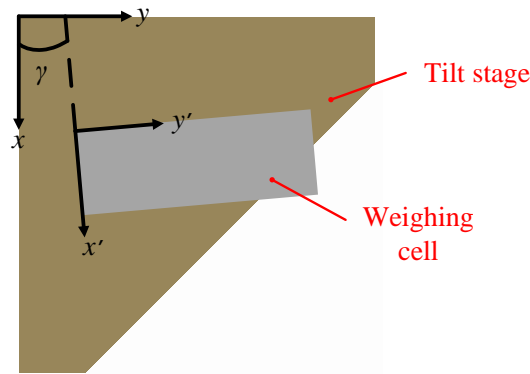


Figure 2.4: Drawing of assembling the weighing cell on the tilt stage with a misalignment angle γ , corresponding to configuration (d) from top view.

In figure 2.3, the slopes of the lines indicate the tilt sensitivity of the weighing cell and change along with the different dead load values. With each dead load, the tilt sensitivity is calculated with linear fitting. Figure 2.5 (d) reveals that the tilt sensitivity is proportional to the value of the weight applied on the weighing cell, which agrees with the equation (2.3). With the help of a linear regression, the relationship between the applied mass piece m_0 (in [g]) and the tilt sensitivity T_{s_y} (in [mN rad⁻¹]) is described in the following form for the weighing cell in configuration (d):

$$T_{s_y} = -10.035 \cdot (m_0 - 31.13)$$

Weight value $m_0 = (31.13 \pm 0.16)$ g can be ascertained by tilt sensitivity T_{s_y} of zero. From the experiments and the calculations above, it can be concluded that the tilt sensitivity of the weighing cell in its suspended configuration can be theoretically minimized to zero by applying the weight of 31.13 g on the weighing pan.

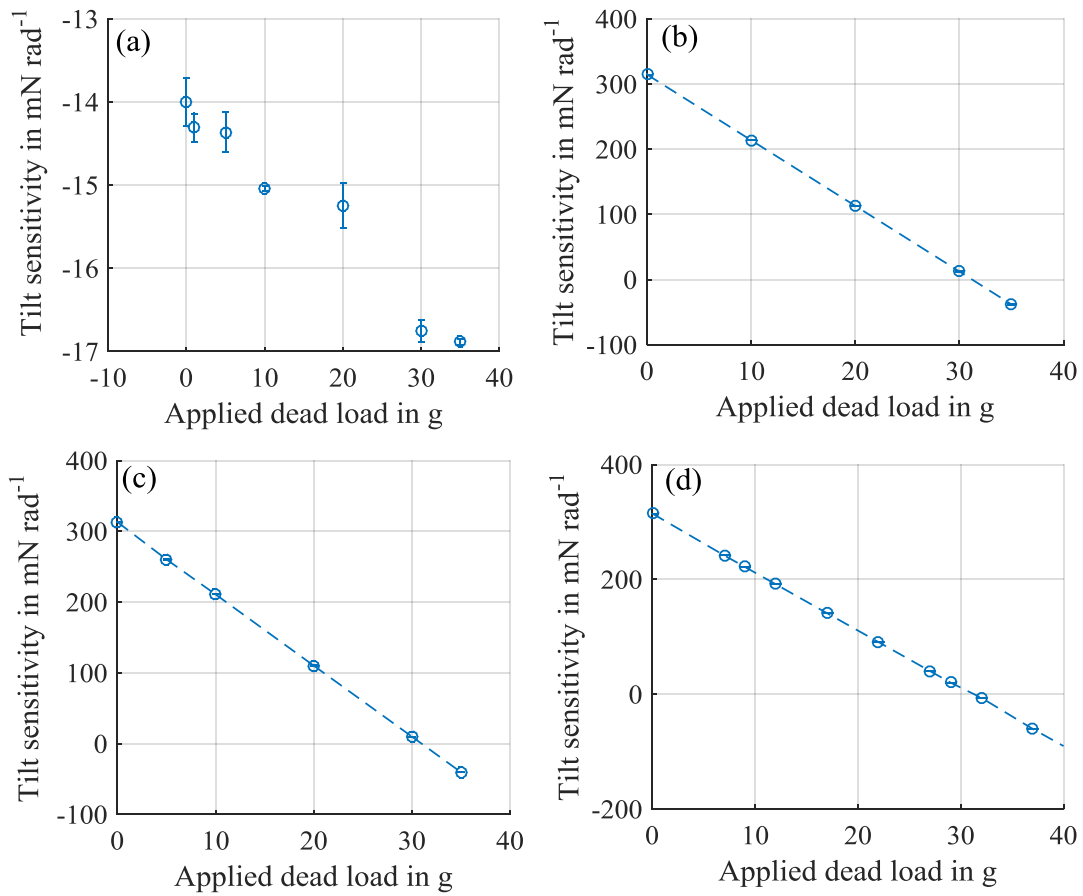


Figure 2.5: The tilt sensitivity of the EMFC weighing cell around the sensitive axis (y -axis) in four configurations (corresponding to figure 2.2) along with the applied dead load values (dead loads are applied on the weighing pan).

The tilt sensitivity of the weighing cell around the sensitive axis (y -axis) of each configuration is calculated and drawn in figure 2.5. The same measurement procedure is repeated during the other three configurations, similar results are achieved in configurations (b) and (c) after the correction with the misalignment angle γ , where the calculated weight m_0 is (31.24 ± 0.15) g and (30.98 ± 0.14) g respectively. A significant deviation appears in the measurements during configuration (a) when the weighing cell performs as a classic balance. In this configuration, the tilt sensitivity of the system with no externally applied dead load is a negative value of -14 mN rad⁻¹ deviated from 312 mN rad⁻¹ in the other three configurations. The required compensating weight m_0 to minimize the tilt sensitivity appears to be a negative value, which means that instead of adding the mass piece on the weighing pan, the weight should be applied on the other side of the lever arm, namely on the counterweight. To clarify this deviation, it is important to have a clear picture of the weighing cell in the four configurations as figure 2.6 shows, in each configuration the weighing cell is presented with a tilt angle α around y -axis.

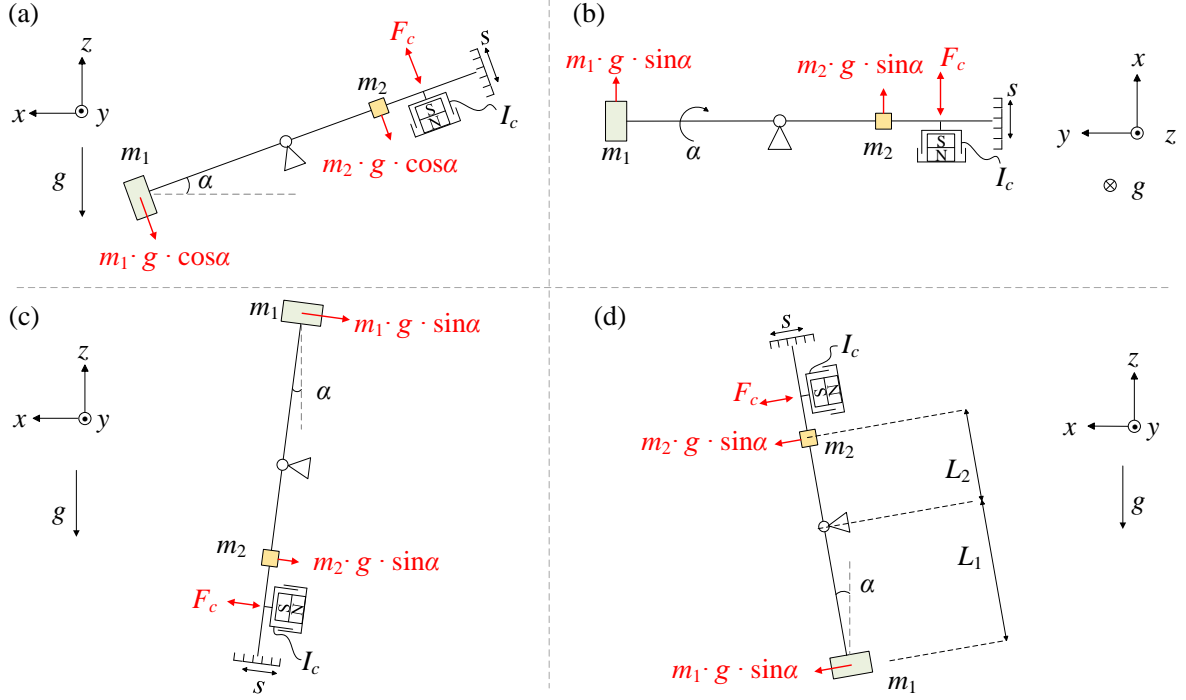


Figure 2.6: Sketched structure of the tilted EMFC weighing cell in four configurations (corresponding to figure 2.2). I_c - compensation current; F_c - compensation force; s - deflection of the lever detected by positioning sensor. (a), (c) and (d) are from side view while (b) is from top view.

As mentioned before, the weighing cell in configurations (b) (c) and (d) can be uniformed as only with different rotation angles in the yz -plane of 90° for configuration (b), 180° for configuration (c) and 0° for configuration (d). In these three configurations, the tilt forces act upon both sides of the lever are proportional to $\sin\alpha$ as indicated in figure 2.6 and equation (2.3). However, in configuration (a) the tilt forces depend on $\cos\alpha$ as equation (2.7) shows.

$$F_t \propto (m_1 \cdot L_1 - m_2 \cdot L_2) \cdot g \cdot \cos \alpha \quad (2.7)$$

In this set of experiments, the tilt angle is produced in a small range of ± 8 mrad, with the small-angle approximation, $\cos\alpha \approx 1 - \alpha^2/2$ while $\sin\alpha \approx \alpha$. Thereby, the tilt sensitivity of the weighing cell in configuration (a) is $T_s = \frac{dF_t}{d\alpha} \propto -(m_1 \cdot L_1 - m_2 \cdot L_2) \cdot g \cdot \sin \alpha$, is much lower than that in the other three

configurations where the tilt sensitivity is $T_s = \frac{dF_t}{d\alpha} \propto (m_1 \cdot L_1 - m_2 \cdot L_2) \cdot g$, and this also explains why the tilt sensitivity in configuration (a) is negative.

Thus, in this subsection of testing tilt sensitivity, the following results can be concluded:

- 1) The tilt force F_t depends linearly on the tilt angle around its sensitive axis (y -axis);

- 2) The tilt sensitivity is linearly dependent on the dead load added on the weighing cell. In configurations (b) (c) and (d) similar results are achieved while the result in configuration (a) differs from the other three. The cause is explained by figure 2.6. By supporting the 1 kg magnet to measure the Lorentz force, the tilt sensitivity can be further amplified and the measurement uncertainty can thereby increase;
- 3) Due to the theoretical calculation and experimental results, the tilt sensitivity can be minimized to zero by adding the appropriate dead load on the weighing cell, namely by fulfilling the requirement of equation (2.2).

2.2 Stiffness of the EMFC weighing cell

Stiffness of a FMS describes the ratio between the force and the resulted displacement. High stiffness indicates robust FMSs, while low stiffness means the higher sensitivity to detect lower forces. The stiffness is also an important index that defines the resolution of the force measurement. With the same technique of positioning detection, a FMS with lower stiffness indicates that it can resolve lower forces. Similar to the investigation on the tilt sensitivity with a set of dead loads, how the dead loads affect the stiffness of the weighing cell is also expected to be studied with the four configurations.

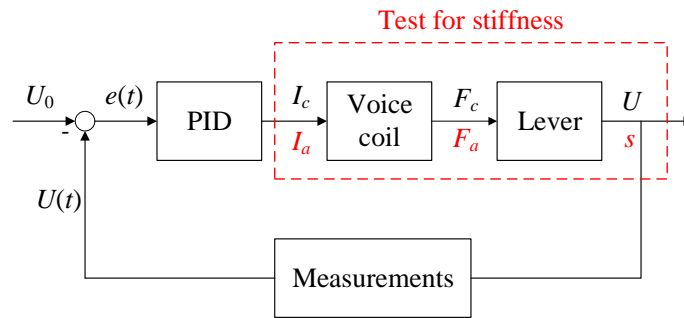


Figure 2.7: Block diagram of compensation procedure of the weighing cell and an option to test the stiffness (in red dash block).

Considering the working principle of the EMFC weighing cell demonstrated in figure 2.7, the position change of the lever caused by forces is continuously recorded and described by the output voltage $U(t)$ of the positioning sensor. The error signal $e(t)$ as the difference between the measured voltage $U(t)$ and the defined voltage value U_0 is transferred to the servo-controller. Compensation current I_c is calculated and applied to the voice coil actuator to generate the compensation force F_c , which brings the lever back to the null position. Alternatively, in the open-loop operation mode where the PID servo-controller is not used, by using the voice coil as a force actuator, controllable stepwise current I_a is applied to the coil to generate controllable stepwise actuation forces F_a . This force leads to the deflections of the lever arm s detected by the positioning sensor and described by the output voltage U . In this way, the stiffness of the weighing cell C_s can be experimentally determined as equation (2.8) shows, where c_1 is a constant depends on the properties of positioning sensor and voice coil.

$$C_s = \frac{F_a}{s} = c_1 \cdot \frac{I_a}{U} \quad (2.8)$$

As shown in figure 2.8, the lever arm is driven by the actuation force F_a and rotates to a new equilibrium as a summation effect of the forces including: ① the electromagnetic actuation force F_a ; ② components of the gravity forces caused by mass m , gravitational acceleration g and angular deflection β ; and ③ the elastic force caused by the spring constant of the mechanical structure C_p and the angular deflection of the lever arm β .

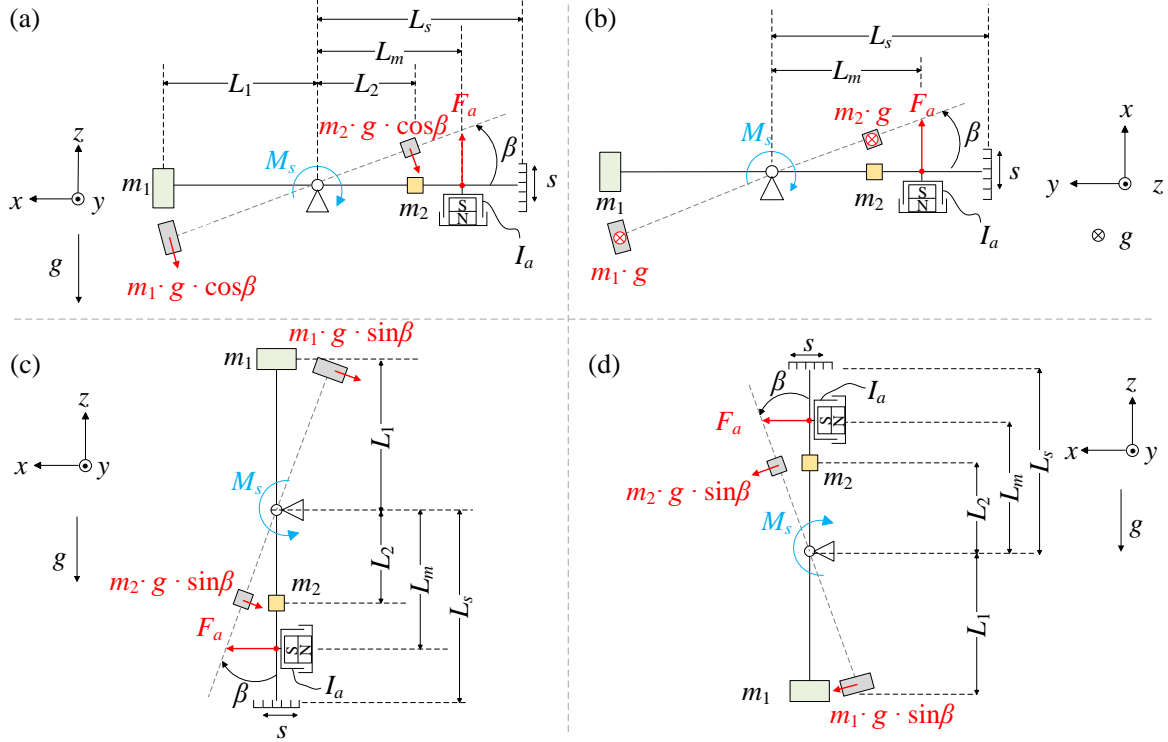


Figure 2.8: Sketched of the main structure of the EMFC weighing cell together with the parameters used to determine the stiffness of the system, in four configurations (corresponding to figure 2.2). (a), (c) and (d) are from side view while (b) is from top view.

Following are the variables presented in figure 2.8 and adopted in later calculations:

F_a	[N]	Electromagnetic actuation force leading to deflection of the lever
L_m	[m]	Arm length of the actuation force F_a , distance from the voice coil actuator to the pivot
m_1	[kg]	Deadweight at the position of the weighing pan on one side of the lever
m_2	[kg]	Deadweight of the counterweight on the other side of the lever
Δm_1	[kg]	Additionally applied mass on the weighing pan
Δm_2	[kg]	Additionally applied mass on the counterweight
L_1	[m]	Arm length of the deadweight m_1

2. Investigation on the EMFC weighing cell

L_2	[m]	Arm length of the dead weight m_2
β	[rad]	Angular deflection of the lever arm, caused by actuation force F_a
M_s	[N m]	Torque caused by the spring constant of the weighing cell and the angular deflection β
s	[m]	Linear displacement at the positioning sensor
L_s	[m]	Distance between the pivot and positioning sensor
C_s	[N m ⁻¹]	Linear stiffness of the weighing cell
C_r	[N rad ⁻¹]	Rotational stiffness of the weighing cell
C_p	[N m rad ⁻¹]	Spring constant of the mechanical structure of the weighing cell

In each configuration, the linear deflection s and linear stiffness C_s can be described by the angular deflection β (β is minor) and rotational stiffness C_r as:

$$C_s = \frac{F_a}{s}; C_r = \frac{F_a}{\beta}; s = L_s \cdot \beta$$

$$\text{Therefore, } C_s = \frac{C_r}{L_s} \quad (2.9)$$

The torque M_s caused by the spring constant of the lever C_p and the angular deflection β can be described as:

$$M_s = C_p \cdot \beta \quad (2.10)$$

Stepwise current I_a is applied to the voice coil while the deflection of the lever is recorded by the positioning sensor. The tests are repeated with a set of different mass pieces Δm_1 applied on the weighing pan changing the value of m_1 ; conditionally restricted dead loads Δm_2 are applied on the other side of the lever arm for changing the value of m_2 only with configuration (a). According to figure 2.8, the analytical calculations for each configuration are as following:

Configuration (a):

When the weighing cell is located in configuration (a) with the common use as a balance, the equation (2.11) can be written to describe its equilibrium indicated in figure 2.8 (a), where the lever arm is differed from its null position by the actuation force F_a :

$$F_a \cdot L_m + (m_1 + \Delta m_1) \cdot g \cdot \cos \beta \cdot L_1 - (m_2 + \Delta m_2) \cdot g \cdot \cos \beta \cdot L_2 - M_s = 0 \quad (2.11)$$

Together with equation (2.9) and (2.10):

$$C_r = \frac{dF_a}{d\beta} = \frac{C_p - [(m_2 + \Delta m_2) \cdot L_2 - (m_1 + \Delta m_1) \cdot L_1] \cdot g \cdot \sin \beta}{L_m}$$

$$C_s = \frac{C_r}{L_s} = \frac{C_p + [(m_1 + \Delta m_1) \cdot L_1 - (m_2 + \Delta m_2) \cdot L_2] \cdot g \cdot \sin \beta}{L_m \cdot L_s} \quad (2.12)$$

In case $\Delta m_1 = \Delta m_2 = 0$:

$$C_{s0} = \frac{C_p + (m_1 \cdot L_1 - m_2 \cdot L_2) \cdot g \cdot \sin \beta}{L_m \cdot L_s} \quad (2.12')$$

Here the m_1 , m_2 , C_p , L_1 , L_2 , L_m and L_s are constants that depend on the mechanical structure of the weighing cell. To investigate the effect of dead load on the stiffness of the system, the added dead loads Δm_1 and Δm_2 are considered as the variable.

The initial stiffness of the system without additionally applied mass pieces is indicated in equation (2.12'). The form of the stiffness is complicated as it depends on the angular deflection β , which is not a constant. However, due to the mechanical structure of the weighing cell, the deflection range of the lever arm is minor in the range of sub-milliradians; thereby the influence on the stiffness caused by the change of the angle β is negligible. Thus, by increasing the value m_1 , the stiffness of the weighing cell increases while by increasing m_2 , the stiffness decreases, which matches with the experimental results demonstrated in figure 2.9 (a). The positive values of Δm in figure 2.9 indicate the mass pieces are applied on the weighing pan, while the negative values indicate the mass pieces are added on the counterweight. In figure 2.9 (a), obvious difference is between the slopes in the two cases where the additional dead load is applied on each side of the lever arm. As equation (2.12) presents, this is caused by the difference between the value of L_1 and L_2 as they are the multiplication factors of the change in dead load value.

Configuration (b):

In figure 2.8 (b), the weighing cell is located in the sidewise position and is demonstrated from the top view. The lever deflects around the pivot in the xy -plane as a result of actuation force F_a and the torque M_s . The gravity forces of m_1 and m_2 are in the yz -plane and makes no influence on the rotation of the lever when no tilt exists. Therefore, the equilibrium of the weighing cell can be described with equation (2.13) and the stiffness of the weighing cell in this configuration can be described as equation (2.14):

$$F_a \cdot L_m - M_s = 0 \quad (2.13)$$

$$C_r = \frac{dF_a}{d\beta} = \frac{C_p}{L_m}$$

$$C_s = \frac{C_r}{L_s} = \frac{C_p}{L_m \cdot L_s} \quad (2.14)$$

Figure 2.9 (b) shows the experimentally obtained stiffness values during the sidewise configuration. In comparison with the other three configurations, the stiffness does not show significant change along with the applied dead load values. This also agrees with the analytical calculated equation (2.14) where deadweight forces make no influences. The deviations in the measured data can be caused by tilt of the system during the measurements, which leads to distorted output as it was discussed in the section 2.1.

Configuration (c):

In the suspended configuration with the weighing pan upwards (similar to inverse pendulum) shown in figure 2.8 (c), the equilibrium of the weighing cell can be described with equation (2.15), by which the stiffness in this configuration is indicated with equation (2.16):

$$-F_a \cdot L_m - (m_1 + \Delta m_1) \cdot g \cdot \sin \beta \cdot L_1 + (m_2 + \Delta m_2) \cdot g \cdot \sin \beta \cdot L_2 + M_s = 0 \quad (2.15)$$

$$C_r = \frac{dF_a}{d\beta} = \frac{-(m_1 + \Delta m_1) \cdot g \cdot L_1 + (m_2 + \Delta m_2) \cdot g \cdot L_2 + C_p}{L_m} \quad \text{with } \sin \beta \approx \beta$$

$$C_s = \frac{C_r}{L_s} = \frac{-(m_1 + \Delta m_1) \cdot g \cdot L_1 + (m_2 + \Delta m_2) \cdot g \cdot L_2 + C_p}{L_m \cdot L_s} \quad (2.16)$$

In case $\Delta m_1 = \Delta m_2 = 0$:

$$C_{s0} = \frac{C_p - (m_1 \cdot L_1 - m_2 \cdot L_2) \cdot g}{L_m \cdot L_s} \quad (2.16')$$

Configuration (d):

Similar to configuration (c), in configuration (d) the weighing cell is suspended, however now with the weighing pan downwards as used previously in [27, 29] to measure the Lorentz force:

$$F_a \cdot L_m - (m_1 + \Delta m_1) \cdot g \cdot \sin \beta \cdot L_1 + (m_2 + \Delta m_2) \cdot g \cdot \sin \beta \cdot L_2 - M_s = 0 \quad (2.17)$$

$$C_r = \frac{dF_a}{d\beta} = \frac{(m_1 + \Delta m_1) \cdot g \cdot L_1 - (m_2 + \Delta m_2) \cdot g \cdot L_2 + C_p}{L_m} \quad \text{with } \sin \beta \approx \beta$$

$$C_s = \frac{C_r}{L_s} = \frac{(m_1 + \Delta m_1) \cdot g \cdot L_1 - (m_2 + \Delta m_2) \cdot g \cdot L_2 + C_p}{L_m \cdot L_s} \quad (2.18)$$

In case $\Delta m_1 = \Delta m_2 = 0$:

$$C_{s0} = \frac{C_p + (m_1 \cdot L_1 - m_2 \cdot L_2) \cdot g}{L_m \cdot L_s} \quad (2.18')$$

From the theoretically calculated equations (2.16) and (2.18), it is revealed that in configuration (c) the stiffness is proportional to the value of $-\Delta m_1$ while in configuration (d) the stiffness is proportional to Δm_1 . Hence, in figure 2.9 (c) the stiffness decreases with the increased dead load on the weighing pan

while in (d) the situation is opposite. Moreover, when Δm_1 and Δm_2 equal to zero which indicates that no additional dead load is applied, the initial stiffness C_{s0} is described by equation (2.16') and (2.18') for the two configurations respectively. As $m_1 \cdot L_1 \neq m_2 \cdot L_2$, the values of initial stiffness differ from each other in the two configurations. This also matches with the experiments when no dead load is applied, the stiffness of the system in configuration (c) is 45.82 N m^{-1} , which is 41.4% higher than 32.4 N m^{-1} determined in the configuration (d). This reveals $m_1 \cdot L_1 < m_2 \cdot L_2$, and considering equation (2.12') and (2.14) this also explains the reason why the initial stiffness C_{s0} determined in configuration (a) is lower than that in configuration (b) with the $m_1 \cdot L_1 - m_2 \cdot L_2 < 0$.

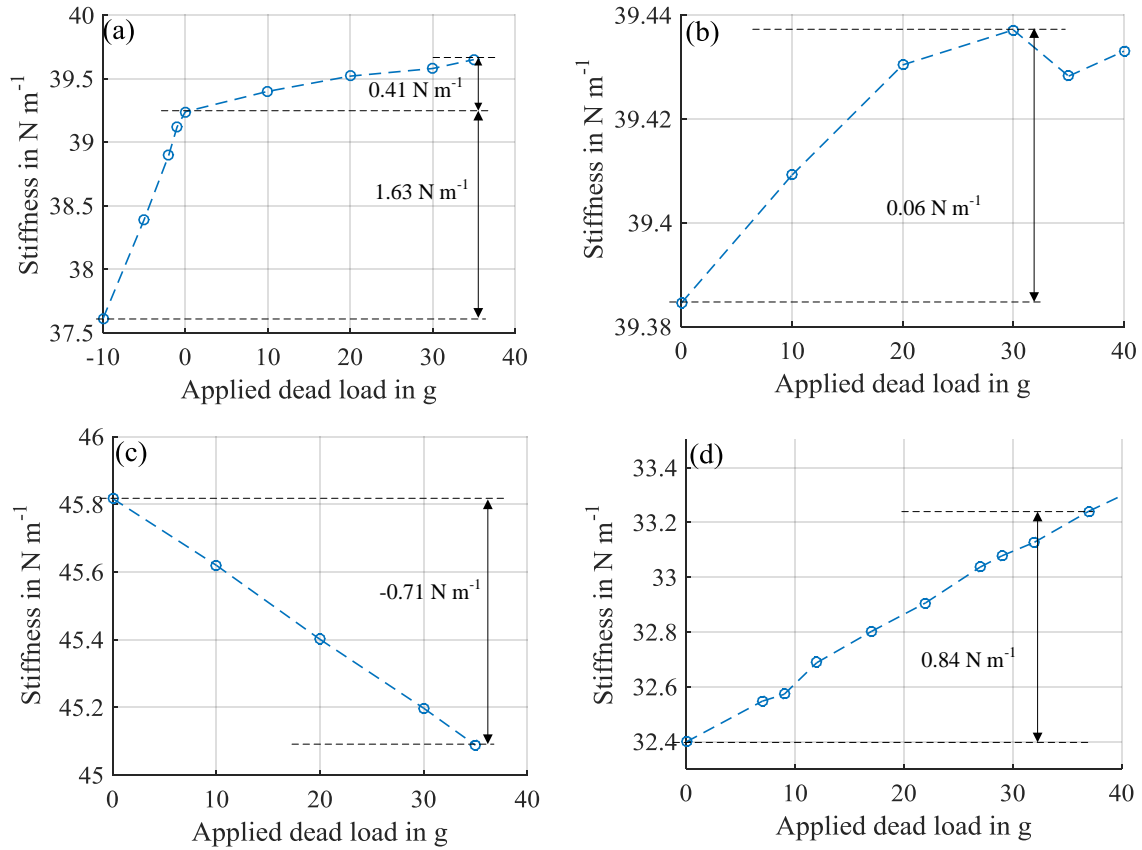


Figure 2.9: The stiffness of the EMFC weighing cell in four configurations (corresponding to figure 2.2) along with applied dead loads (positive dead load values mean mass standards are added on weighing pan changing m_1 , while negative values indicate dead loads are added on the counterweight for changing m_2).

Thus, in this subsection of testing the stiffness the following results can be concluded:

- 1) The stiffness of the system can be changed by locating the EMFC weighing cell in different configurations;
- 2) By adding dead loads on the EMFC weighing cell, different effects can be acted on changing the value of stiffness in different configuration as summarized by table 2.2:
 - a) In configuration (a), adding dead load on m_1 increases the stiffness while adding dead load on m_2 the stiffness is reduced;

- b) In configuration (b), stiffness is constant (not considering the influence caused by tilt);
- c) In configuration (c), adding dead load on m_1 decreases the stiffness while adding dead load on m_2 the stiffness is increased;
- d) In configuration (d), opposite to the case in configuration (c), adding dead load on m_1 increases the stiffness while adding dead load on m_2 the stiffness is decreased.

Table 2.2: Effects on stiffness caused by different dead load values in four configurations.

Configuration		Stiffness of the system
Common usage as a balance	$m_1 \uparrow$	\uparrow
	$m_2 \uparrow$	\downarrow
Sidewise	$m_1 \uparrow$	—
	$m_2 \uparrow$	—
Suspended with weighing pan upwards	$m_1 \uparrow$	\downarrow
	$m_2 \uparrow$	\uparrow
Suspended with weighing pan downwards	$m_1 \uparrow$	\uparrow
	$m_2 \uparrow$	\downarrow

This also indicates that by carrying the 1 kg magnet system in the suspended configuration (d) in previous researches in [27] and [29], the stiffness of the EMFC weighing cell is thereby largely increased to 53.92 N m^{-1} according to the calculation with the linear fitting. This change in stiffness also leads to the undesired negative effect on measuring sensitivity. As the EMFC weighing cell can also measure the horizontally directed forces in configurations (b) and (c), it is preferable to arrange the EMFC in these two configurations carrying the magnet system, because in configuration (b) the stiffness is constant around 39.42 N m^{-1} , while in configuration (c) the lower stiffness of 27.76 N m^{-1} is achieved due to the 1 kg dead load, which makes the system more sensitive.

2.3 Summary

As an essential part in most of the FMSs developed for the LFV, the EMFC weighing cell provides a better robustness than the PFMS and is expected to measure the force down to nanonewton range. Differs from its common usage as a balance, the EMFC weighing cell was adopted within the framework of LFV in its suspended configuration, supporting the magnet system as a dead load over 1 kg. With the aim to study how the configuration and dead load influence the measurement of the EMFC weighing cell, several experiments were carried out in respect to testing the tilt sensitivity and the stiffness with four different configurations and a set of different dead load values.

The results of the experiments were concluded above at the end of each subsection. To emphasize, when using the EMFC weighing cell, it must be noticed that by supporting the magnet system with a

suspended configuration, the tilt sensitivity of the system can be amplified leading to higher measurement uncertainty. Moreover, the stiffness of the EMFC weighing cell is proportional to the dead load in the suspended configuration. The 1 kg magnet system also amplifies the stiffness and makes the system less sensitive.

In the experiments of testing tilt sensitivity, a way was found to eliminate the tilt sensitivity by applying compensation dead load on the EMFC weighing cell, which can be considered as a way to reduce the errors caused by unavoidable tilt. However, concerning that in the LFV application, the EMFC is required to support the 1 kg magnet as the dead load; to compensate this weight on the precise mechanical structure of the weighing cell is not generally desirable. Using two identical EMFC weighing cells in the DFMS is an alternative method to reduce the noises F_{err} from the F_L' (see figure 1.4). In DFMS, it is required to arrange the highly precise geometrical alignment of the two EMFC weighing cells on the frame. Moreover, the cost of using two highly precise EMFC weighing cells should also be considered. Therefore, considering the requirement of a tilt-insensitive system described in equation (2.2), and also with a constant stiffness unchangeable with the supported dead load values, a torsion force measurement system (TFMS) based on the principle of torsion balance is developed and introduced in the following chapters. With the TFMS, the force resolution is expected to be improved by one order of magnitude, namely, from 20 nN (as using the DFMS) to 2 nN.

3. Design concept of torsion force measurement system

The concept of torsion balance is well known as the experiment was carried out by Henry Cavendish in 1798 to measure the gravitational force between two masses [36]. Nowadays, the principle of torsion balance is still widely used for highly resolved force measurements as introduced in section 1.2.1. In this chapter, the force measurement system based on the principle of torsion balance, namely the torsion force measurement system (TFMS), is introduced. In section 3.1, based on the theoretical calculation considering the resolution of the positioning sensor and the expected force resolution, the geometry of the TFMS is set and the type of commercial bearing is chosen to achieve the appropriate stiffness of the system. From section 3.2 to section 3.5, the components of the TFMS are introduced in details.

3.1 Initial idea and theoretical calculation

As indicated in section 1.2.2, the robust EMFC weighing cell is a reasonable replacement of the PFMS to contribute into Lorentz force measurement. By arranging the weighing cell in the suspended downwards position depicted in figure 2.2(d), the weighing cell can measure the small horizontally directed forces with high dead load. In chapter 2, it is revealed that when the mechanical structure of the measurement system does not fulfill the requirement indicated by equation (2.2), errors can occur in the measured signal when the measurement system tilts. The tilt can happen with movement of people, machines or earth crust; as a result, it is unavoidable. Due to the mechanical structure of the EMFC weighing cell, by adding mass pieces on the weighing pan or on the counterweight, namely changing the value of m_1 and m_2 , the equation (2.2) can be theoretically achieved to minimize the influence of the tilt. However, considering the necessity of supporting the 1 kg magnet system while using EMFC to measure the Lorentz force, it is undesirable to compensate this weight by adding additional mass piece in such order of magnitude on the precise monolithic structure. Moreover, the stiffness that defines the measurement sensitivity of the EMFC weighing cell is also further increased by supporting the dead load in its suspended configuration with weighing pan downwards, in which case the force resolution is also thereby impaired.

The initial idea of this work is to overcome the difficulty in achieving equation (2.2) by developing a symmetrical system, where m_1 equals to m_2 while L_1 equals to L_2 , in another word, center of gravity (COG) is identical with pivot point (PP). This kind of system is well known as torsion balance, by which the Cavendish experiment [36] was carried out in 1798 to measure the gravitational force between large and small spheres. Nowadays, the principle of torsion balance is still widely used to determine the Newtonian constant of gravitation [21] and to test small weak equivalence principle [23]. Force measurement setups based on the principle of torsion balance differ in every application. However, the core structure remains the same. Initially in [36], the torsion balance consists of a rod

and a thin fiber suspending the rod in the middle. At each end of the rod is a small sphere, and next to each small sphere located a large sphere on a separated support. Exerting the gravitational force upon the small spheres, the rod starts to rotate while the fiber twists itself until it reaches an angle, where the twisting force of the wire balances the gravitational force. According to Hooke's law, the gravitational force is proportional to the rotational angle and the spring constant of the torsion balance. The spring constant is determined by measuring the resonant vibration period while the rotational angle is detected by microscope, the gravitational force is thereby measured.

The mechanical structure of the torsion balance can also be considered as a transformation from the monolithic mechanical structure of the EMFC weighing cell in its sidewise configuration by modifying the parameters m_1 , m_2 , L_1 and L_2 . Compared with the configuration (c) and (d) in figure 2.2, in the sidewise configuration, the dead load has a minimized influence on the stiffness of the system. Therefore, by using the principle of the torsion balance, influences on the measurement caused by tilt sensitivity as well as change in stiffness can be theoretically overcome.

In order to develop a robust force measurement system which is more appropriate for LFV, the torsion force measurement system (TFMS) illustrated in figure 3.1 as transformation from the initial torsion balance, is introduced. Compared to the master setups such as in work [21], where measurements are carried out with high precision devices under high precision laboratory conditions, the TFMS is designed with more compact dimensions and with normally achievable components. Sufficient resolution is achieved under the normal laboratory conditions.

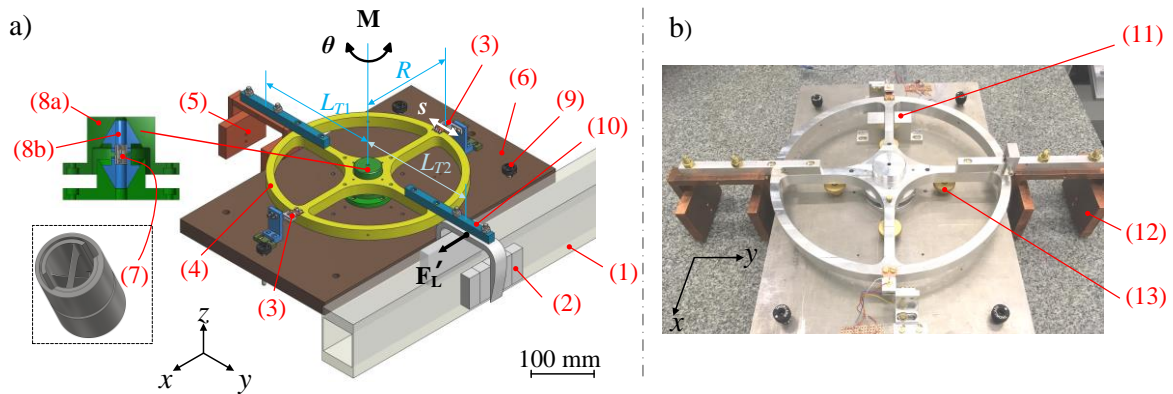


Figure 3.1: Torsion force measurement system: (a) Sketch with flow channel; (b) Snapshot. (1) Flow channel; (2) Integrated magnet system; (3) Positioning sensor; (4) Plane wheel; (5) Non-magnetic copper dummy as counterweight; (6) Baseplate; (7) Commercial flexible bearing hinge; (8a) Outer conical coupling element; (8b) Inner conical coupling element; (9) Adjustable feet; (10) Mechanical connector; (11) Safety fixture; (12) Replacement dummy weight; (13) Knurled screw (4 pieces) to lift the plane wheel.

The plane wheel (4) in figure 3.1 carries the magnet system (2) on one side with the arm length L_{T2} , and on the other side is the non-magnetic dummy weight (5) as the counterweight with the arm length L_{T1} . When the geometry is perfectly symmetrical, namely $L_{T2} = L_{T1}$, and the mass of the dummy is

3. Design concept of torsion force measurement system

identical with the mass of the magnet system, the tilt-insensitive system is thereby achieved by using this design as the requirement of equation (2.2) is fulfilled.

The reaction force \mathbf{F}_L' of the Lorentz force induced by the flowing electrolyte in channel (1) acts upon the magnet system, leads to the torque \mathbf{M} and drives the plane wheel rotate with angle θ , which can be described with equation (3.1).

$$\mathbf{M} = \mathbf{L}_{T2} \times \mathbf{F}_L' \quad (3.1)$$

During rotation of the wheel, the commercial flexible bearing (7) assembled together with the wheel, is deformed and provides the elastic force balancing the external force. The wheel then gets its new equilibrium. The deflection of the wheel θ proportional to the torque \mathbf{M} is detected by the positioning sensor (3).

$$M = C_b \cdot \theta \quad (3.2)$$

C_b [N m rad⁻¹] Spring constant of the commercial bearing

A universal principle of measuring force is measuring the deflection of the mechanism with certain stiffness. As aim of this work is measuring the Lorentz force, the effective stiffness C_t of the TFMS, corresponding to arm length L_{T2} , is desired to be determined. The rotational angle θ can be transferred into displacement s at the positioning sensor with $s = R \cdot \theta$ (see figure 3.1). Therefore, the effective stiffness C_t expressing the sensitivity to measure Lorentz force, can be calculated with the geometrical parameters and the spring constant of the bearing hinge C_b by equation (3.3):

$$C_t = \frac{C_b}{L_{T2} \cdot R} \quad (3.3)$$

L_{T2} [mm] Arm length of the reaction force of Lorentz force

R [mm] Length from the positioning sensor to the center of the TFMS

Considering the expected force resolution of 2 nN and the position resolution provided by the positioning sensor of 1 nm, the stiffness of the TFMS is expected to be lower than 2 N m⁻¹. This can be achieved by modifying the parameters on the right side of equation (3.3). Equation (3.3) indicates that the stiffness of the system can be decreased by using bearing hinges with lower spring constants or by increasing the diameter of the wheel, in which cases the maximum axial load of the bearing and the deformation of the system should also be considered. Thereby, the flexible bearing with the spring constant of 1.17·10⁻² N m rad⁻¹ is chosen with the maximum axial load of 101 N, which is sufficient to carry the dummy weight and the magnet system. The outer diameter of the wheel is designed as 250 mm, leading to the value of R and L_{T2} 135 mm and 180 mm respectively. The stiffness of the TFMS is calculated using the equation (3.3) as 0.48 N m⁻¹ and the theoretical force resolution of

0.48 nN is expected. The undamped natural frequency of the system f_n can be calculated with equation (3.4):

$$f_n = \frac{1}{2\pi} \sqrt{\frac{C_b}{J}} = 0.06 \text{ Hz} \quad (3.4)$$

Here, J is the moment of inertia around the z -axis, and the value of $0.0815 \text{ kg}\cdot\text{m}^2$ is calculated using the numerical simulation results. The low undamped natural frequency is a result of the high dead load as well as the low spring constant of the bearing. Due to the theoretical calculation, the TFMS with an undamped natural frequency of 0.06 Hz is expected to measure forces down to 0.48 nN. The components of the TFMS presented in figure 3.1 are introduced in the following sections in details.

3.2 Plane wheel with dead load

In Cavendish experiment [36], the rod carries two identical small spheres at each end. The mutual attraction force between the small sphere and the leaden large sphere located nearby enables the twisting of the fiber and rotating of the rod. Analogous situation is for the TFMS to measure Lorentz force, where the TFMS has to carry the magnet system of over 1 kg to generate magnetic field, upon which exerted force is to be measured. As a transformation from the rod carrying two spheres in the initial torsion balance, a plane wheel with the outer diameter of 250 mm ((4) in figure 3.1) is chosen to carry the magnet system (2) on one side, and on the other side is a the non-magnetic dummy weight (5) as the counterweight with similar mass and geometrical dimensions. The plane wheel is in symmetrical geometry with the theoretically equal arm lengths L_{T1} and L_{T2} , and provides sufficient place for further assembling. Moreover, the weight is reduced compared to a form of disc with same diameter and material. The two additional connectors (10) provide the convenience to assemble the magnet and dummy weight on the plane wheel, and extends the effective arm length L_{T1} and L_{T2} from 125 mm to 180 (± 2) mm in order to reduce the stiffness and increase the sensitivity of the system. In the initial tests of the capabilities of the TFMS, the magnet system is replaced by a second identical dummy weight (12) to avoid the magnetic interaction caused by the magnet system and other magnetic material/parts in the laboratory. Therefore, the TFMS with the plane wheel carrying dead load theoretically meets the requirement in equation (2.2), which describes an insensitive system to unavoidable tilt.

3.3 Flexible bearing support

3.3.1 Flexible bearing hinge

In [36], the rod and the two small spheres are suspended with a thin fiber, which is connected to the frame and provides twisting force during rotating to balance the gravitational force. Considering the TFMS developed for LFV, using the thin fiber and frame is neither space-saving nor constraints the rotation within the horizontal plane well. A replacement of the thin fiber is desired to build a more robust and compact system. In the mechanical structure of the EMFC weighing cell, the force is transformed into deflection by manufacturing monolithic flexure with elliptical notch flexure pivot.

Similarly, this kind of precise mechanical structure generating elastic force by deformation can be used in the TFMS. A reasonable option is using the flexible bearing hinge depicted in figure 3.2, which is commercially achievable.

The commercial flexible bearing hinge provided by C-Flex Bearing [37] consists of three parts: the core containing the flexure spring, which deforms and provides elastic force with relative movements between the two semi-cylinder segments; and two sleeves assembled solidly on each segment of the core. The sleeves and the core are so assembled coaxially that sleeve 1 is fixed on the core with segment 1, while untouched with segment 2. Analogously, sleeve 2 is fixed on segment 2 but separated from segment 1. The assembled areas are highlighted on the sleeves with pink color. As the side view and top view present, the load acting on sleeve 1 is transferred onto segment 1 assembled to it, while the other segment together with sleeve 2 is fixed. This leads to the deformation of the flexure springs and generates the twist; the elastic force thereby balances the external load. In this way, the commercial flexible bearing enables the rotational motion without friction; similar to the fiber contributes to the torsion balance. An advantage of using the commercial flexible bearing is that the bearings are provided by the manufacturer with different specifications (dimensions and values of spring constant), which makes it convenient to achieve multiple sensitivities in force measurement. In this work, the bearing type D-10 with spring constant $1.17 \cdot 10^{-2} \text{ N m rad}^{-1}$ and diameter of 6.35 mm is chosen based on the theoretical calculation considering the aim resolution of 2 nN. The maximum permissible rotational angle provided by the chosen bearing is $\pm 15^\circ$, which is sufficient for the TFMS to measure force in sub-micronewton range.

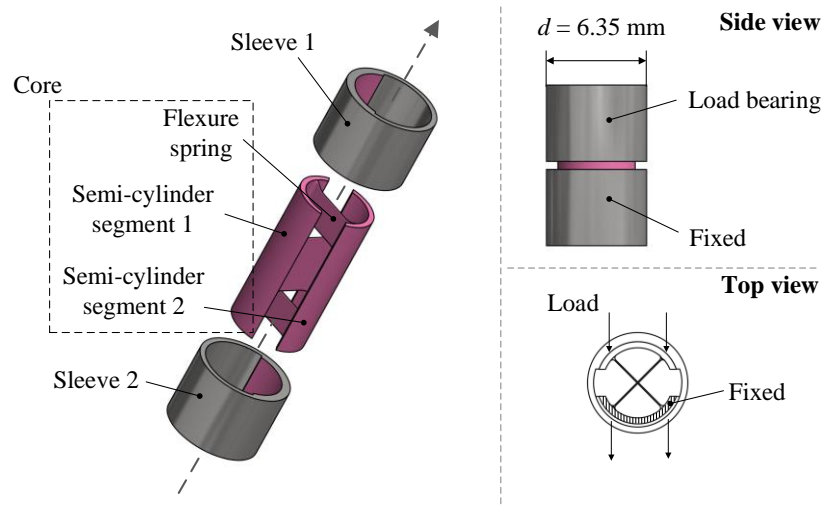


Figure 3.2: Mechanical structure of commercial flexible bearing hinge, drawn according to the data provided by the manufacturer [37].

3.3.2 Conical coupling

The mechanical components shown in figure 3.1 are manufactured from aluminum AW 7075 alloy. The plane wheel and the additional connectors together with the two copper dummy weights are approximately 3 kg, not exceeding the maximum axial load value of the bearing, given by the

manufacturer as 101 N. In reality during assembling, imperfection in alignment can exist. Moreover, during storage or usage, undesired vibrations of ground may occur. In these cases, radial loading in compression and tension can also exist and damage the bearing. To overcome this problem, the additional conical coupling elements (8a) and (8b) in figure 3.1 are designed to avoid the damage.

As illustrated in figure 3.1, the conical coupling elements consist of two inner wedges 8(b) and two outer wedges 8(a). Each inner wedge and outer wedge match with each other by a fine machined 60° angle without fixing element. The two identical inner wedges are glued on each sleeve of the bearing. One of the two outer wedges is screwed on the plane wheel while the other one is screwed on the base plate. Instead of fixing the sleeves of the flexible bearing directly with the plane wheel and the base plate, using this wedge shaped connection with conical coupling elements provides on one hand the stable combination of components during measurements under peaceful situations, and on the other hand enables the relative movement between inner and outer wedges to protect the bearing in aggressive situations where high amplitude vibration occurs.

3.4 Positioning sensor

In the torsion balances developed nowadays, high resolution devices such as autocollimators and laser interferometers are widely used for detection of the position. The kind of optical positioning sensor [38] used in the TFMS ((3) in figure 3.1) is commercial and also used in the EMFC balances to detect the motion of the lever arm. Compared to autocollimator and interferometer, the optical positioning sensor provides enough resolution for the measurements in this work with an extremely reduced compact dimension. The simplified structure of the positioning sensor is illustrated in figure 3.3 (a), where the infrared-LED (1) as the light source illuminates the two-segment differential photodiode (3) via a narrow rectangular aperture (2).

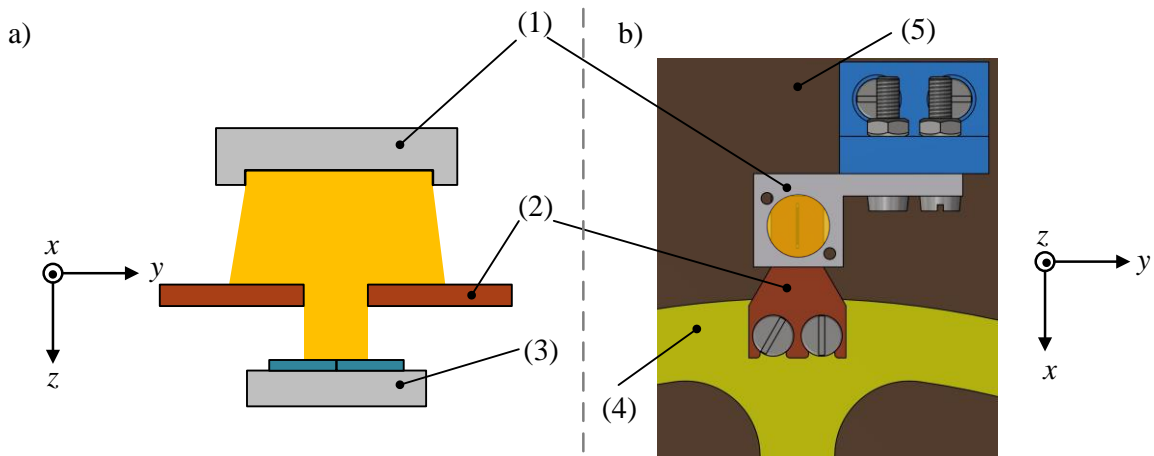


Figure 3.3: Structure of the optical positioning sensor. a) Side view. b) Top view, mounted on the TFMS. (1) LED with metal housing; (2) Aperture; (3) Two-segment differential photodiode with metal housing; (4) Plane wheel; (5) Base plate.

3. Design concept of torsion force measurement system

Figure 3.3 (b) highlights the positioning sensor mounted on the TFMS, where the aperture is fixed on the plane wheel as the rotational component, and the LED and the photodiode are fixed on the base plate as the unmovable components. When the aperture moves together with the plane wheel as a result of external force, the received light on one segment of the photodiode increases while decreases on the other. The difference of the two signals is proportional to the position change of the aperture and results in the voltage change as the output signal. This technique of position measurement enables variable measurement ranges, resolutions and sensitivities by assembling different types of LEDs, photodiodes and the different sizes of aperture. The optical positioning sensor used in this work provides a resolution of 1 nm.

As the first test of the optical positioning sensor, the LED illuminates directly on the photodiode without aperture. Nearby is a thermal resistor, by which the temperature around the positioning sensor can be changed. The positioning sensor together with the thermal resistor is covered with polystyrene box for thermal and light isolation. Without considering the object whose position is to be measured, the LED and photodiode is thermal dependent as indicated in figure 3.4, with the coefficient of approximately 0.27 mV K^{-1} . All the experiments with the TFMS are implemented in the laboratory condition where the temperature is constant within 0.1 K over several days. By this temperature change, the change in measured voltage value from positioning sensor results to $27 \mu\text{V}$, which is taken in to consideration in the later calculation.

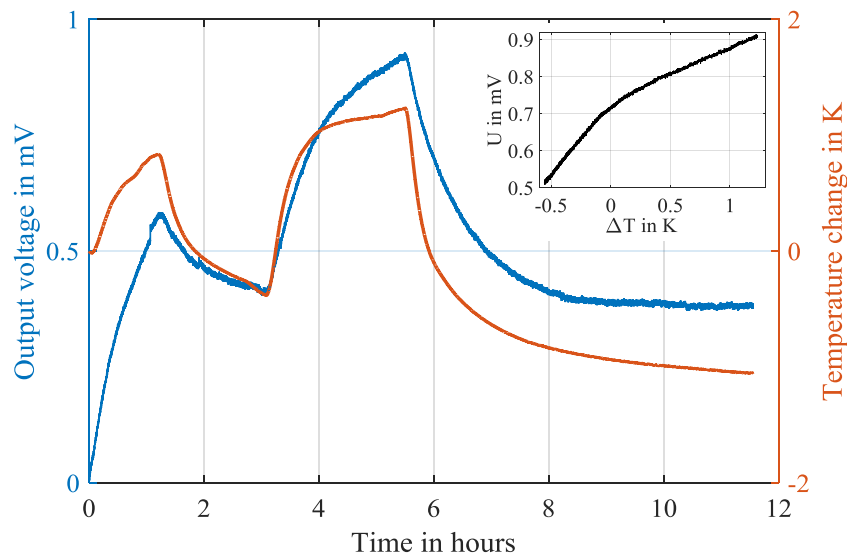


Figure 3.4: Test of the temperature dependency of the positioning sensor (without aperture). Blue: Output of the positioning sensor during 12 hours; red: controlled temperature change with a thermal resistor. Inset: output voltage changes along with the temperature.

The voltage being the initial output of the positioning sensor is recorded by a 4-channel-analog input module NI 9239, providing measurement range of $\pm 10 \text{ V}$ at a 24-bit resolution with the maximum sampling rate of 50 kS s^{-1} [39]. The NI module is first calibrated with the reference values from a multi-function calibrator FLUKE 5720A which was calibrated at PTB. Stepwise values in the range of $\pm 10 \text{ V}$ indicating the full measuring range and $\pm 1 \text{ V}$ as the linear output range of the positioning

sensor are transferred into the NI module. The measurement uncertainty of each step is determined and figure is shown in the appendix A. In both ranges, the mean value of the uncertainties at all steps is $9.24 \mu\text{V}$. This module provides sufficient measurement capabilities for TFMS with a compact dimension.

3.5 Adjustment and safety components

The TFMS is located on a granite workbench. The base plate (6) in figure 3.1 is supported on the workbench by three fine adjustable screws (9) with a pitch of 0.25 mm. With the three-feet-support, the working plane of the TFMS can be adjusted finely around its x - and y -axis. Two additional screw feet are assembled to the TFMS without touching the workbench only for safety. The two connectors (10) are screwed on the plane wheel on one side and support each dummy weight on the other side. By connection, the tolerance of ± 2 mm is available to provide the possibility to adjust the arm length L_{T1} and L_{T2} . The safety fixtures (11) limit the rotation of the wheel within a safe working range, which is enough for measurement in sub-micronewton and not exceeding the rotational angle of $\pm 15^\circ$ given by the manufacturer in case undesired punch or shock occurs. The four knurled screws (13) under the plane wheel are screwed on the base plate, each of which is further processed so that on the upper surface a ball is assembled. During the TFMS operates to measure forces, the knurled screws together with the small balls are separated from the plane wheel. For storage, the knurled screws are firstly screwed carefully upwards until the balls touch the plane wheel, and then screwed further to lift up the plane wheel, so that the flexible bearing is free from load and thereby under protection.

3.6 Summary

As a replacement and improvement of the previously used FMSs to measure Lorentz force, the TFMS based on the principle of torsion balance is introduced in this chapter. A plane wheel together with the dead loads carried by it is in a symmetrical geometry. The commercial flexible bearing is used to enable the non-frictional rotational motion and provide elastic force during deformation to balance the external forces. Various types of bearings with different specifications are commercially achievable according to various requirements in applications. A state-of-the-art optical positioning sensor is used to detect rotational angles, which are transferred into force values with stiffness. Theoretically, the system fulfills the requirement of equation (2.2), which describes an insensitive system to unavoidable tilt angles. Moreover, with a similar structure as the EMFC weighing cell in its sidewise configuration, the stiffness of the TFMS remains constant with different values of dead load. Due to geometrical dimensions and parameters given by the manufacturer, the theoretically calculated force resolution is 0.48 nN with the undamped natural frequency of 0.06 Hz. To achieve a system with force resolution of 2 nN, the calculated theoretical resolution is acceptable. As a summary, the geometrical and functional parameters of the TFMS are presented in the table 3.1.

Based on this design concept, various TFMSs with different dimensions and sensitivities can be manufactured not only for LFV but also for fitting different applications. In addition to the flexibility, the TFMS is more cost effective, yet has the potential to achieve the expected force resolution in the range of nanonewton.

3. Design concept of torsion force measurement system

Table 3.1: Geometrical and functional parameters of the TFMS.

Term	Value	Unit
Diameter of plane wheel	250	mm
Arm length of dead loads L_{T1}, L_{T2} (adjustable within ± 2 mm)	180	mm
Arm length of the positioning sensor (adjustable within ± 1 mm)	135	mm
Mass of magnet system	1.008	kg
Mass of dummy	1.071	kg
Mass of rotational components supported by bearing	≈ 3	kg
Max. load capacity of the bearing	≈ 10	kg
Diameter of bearing	6.35	mm
Max. compression	16.02	N
Max. tension	63.19	N
Spring constant of bearing	$1.17 \cdot 10^{-2}$	N m rad ⁻¹
Resolution of positioning sensor	1	nm
Theoretical effective stiffness	0.48	N m ⁻¹
Theoretical force resolution	0.48	nN
Undamped natural frequency	0.06	Hz

4. TFMS in the open-loop operation mode

Based on the design concept introduced in chapter 3, the components of the TFMS are manufactured and assembled together. In this chapter, adjustments, calibration procedures and experiments are carried out on the TFMS in the open-loop operation mode. Utilizing the behavior of the TFMS during tilting, the deflection method is introduced as a traceable method to perform position calibration (section 4.1) and force calibration (section 4.2). Although the TFMS is introduced as a theoretically insensitive system to the unavoidable tilt, imperfections in geometry of the mechanical components and misalignment during assembling can occur in reality. Consequently, the tilt sensitivity is no longer zero and cannot be ignored. Therefore, similar to that in section 2.1, the test and minimization of the tilt sensitivity of the TFMS is described briefly in section 4.2.1. In section 4.3, the system identification of the TFMS in the open-loop operation mode is presented.

4.1 Position calibration using deflection method

As mentioned in section 3.4, the optical positioning sensor detects the movement of the plane wheel and outputs voltage as the measured signal. In order to detect the position change, the voltage is expected to be calibrated into rotational angle values. The general procedure for position calibration is presented in figure 4.1. An autocollimator *Elcomat 3000* [40] is chosen as a reference system to measure rotational angles θ . When the plane wheel is excited by the actuation force F_a into controllable stepwise rotation motion in the horizontal plane, the motion is detected by the positioning sensor with the output voltage U_p as well as by the autocollimator with the measured rotational angle θ . The calibration factor K_{ps} can be thereby experimentally determined. Moreover, when the actuation force F_a is traceable, the force calibration can be implemented by comparing the voltage U_p with the force value, which will be introduced in section 4.2.

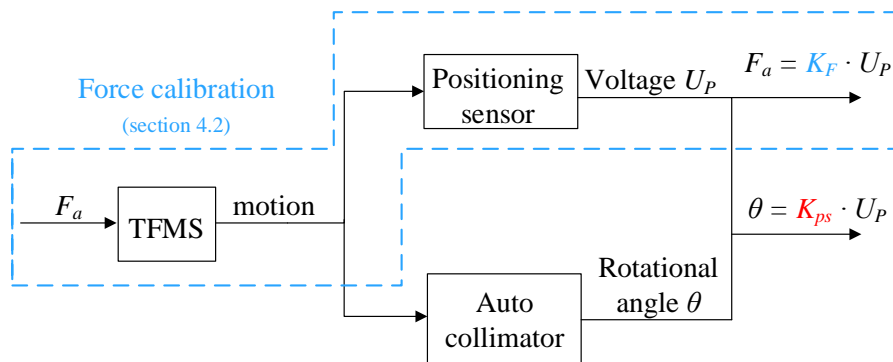


Figure 4.1: Block diagram of the calibration process of the positioning sensor using the autocollimator as the reference system. When the actuation force F_a is traceable, force calibration can be thereby implemented by comparing the force value with the output voltage U_p .

Reproducible actuation forces F_a are usually necessary for executing comparison and calibration procedures in the force measurement technique. In factory inspection of balances or researching in weighing instruments, deadweight forces in vertical direction are usually provided by high class weight-set [12,18]. In applications where horizontally directed actuation forces are desired, for example, to actuate the TFMS into motion, there are several techniques and commercial products can be used in the current state. Voice coil actuator can generate electromagnetic actuation forces; capacitive force actuator can provide electrostatic forces; piezo actuators and micro stages can generate actuation strokes. Avoiding fixing/screwing voice coil or electrode of capacitor as additional components on the TFMS where electric current or voltage is necessary to be supplied, reproducible forces in quasi-horizontal plane can be generated taking convenience of using devices in the laboratory based on the deflection method.

4.1.1 Force/ motion actuation using deflection method

Based on previous research on the EMFC weighing cell introduced in section 2.1, when the suspended weighing cell deflects from the gravitational direction by a tilt angle α , a tilt force F_t presented in equation (2.3) exerts on the system and distorts the measurement result. To reduce the uncertainty of measurement, the tilt sensitivity of the system is expected to be minimized as introduced in chapter 2. The precondition for an insensitive system to tilt angles is described by equation (2.2), where the product of the dead load m_1 on one side multiplied by the lever arm L_1 equals to the dead load m_2 on the other side multiplied by the lever arm L_2 . This can be further explained as the pivot point (PP) being identical to the center of gravity (COG) of a general system.

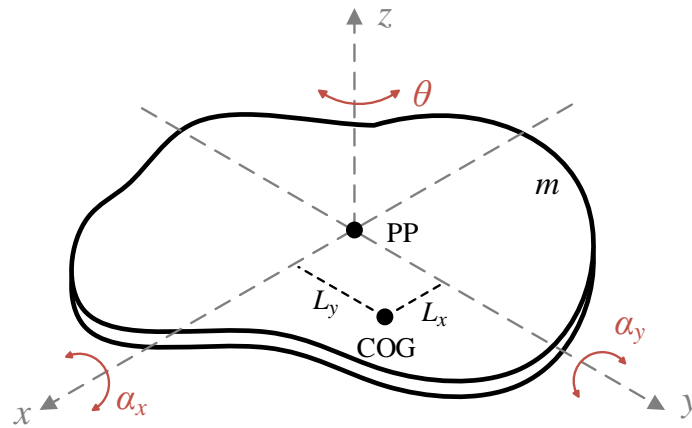


Figure 4.2: General description of a system, by which COG shifts from the PP as the cause of the tilt sensitivity.

In a general system, when COG of the system is not identical to the PP but with the shift L_x and L_y as demonstrated in figure 4.2, the system will leave its equilibrium position driven by the torque \mathbf{M}_t when tilt angles exist, as equation (4.1) denotes:

$$\mathbf{M}_t = \mathbf{L}_x \times (\mathbf{F}_g \cdot \sin \alpha_x) + \mathbf{L}_y \times (\mathbf{F}_g \cdot \sin \alpha_y), \text{ where } F_g = m \cdot g \quad (4.1)$$

When the shift L_x , L_y , the tilt angle α_x , α_y and the mass m are controllable and reproducible, the outcome torque calculated from equation (4.1) is also reproducible. Force values can be derived from the torque with known arm length. Thereby, reproducible motion of the TFMS is enabled by using the deflection caused by tilt angle and shift of COG. Under this condition, the actuation force F_a is achieved using the deflection method. With the achieved actuation force F_a , the position calibration is carried out by comparing the output voltage of the positioning sensor U_P and the measured rotational angle θ by autocollimator as indicated in figure 4.1 [41].

4.1.2 Experimental facility

The deflection method is based on the displacement of COG and the tilt of the system, due to which the tilt force is generated and utilized as the actuation force. The displacement of COG can be performed by adding standard weight on the system, while the reproducible tilt is enabled by the tilt stage. In order to implement the position calibration procedure, reproducible motion of the TFMS is realized using the deflection method by setting up the experimental facility illustrated in figure 4.3.

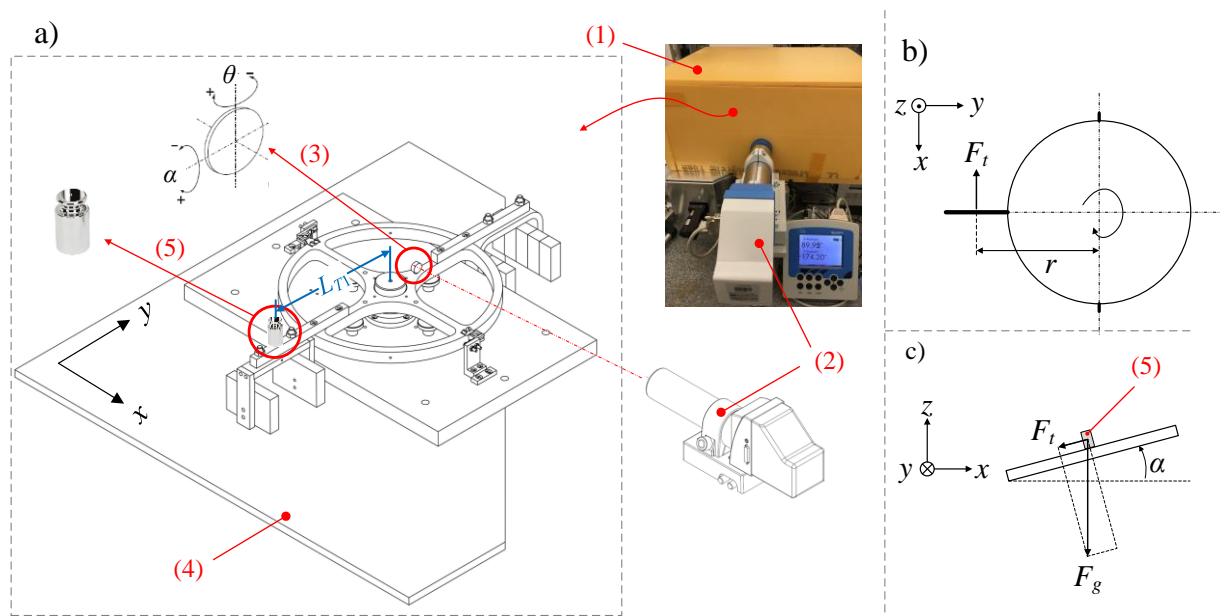


Figure 4.3: a) Calibration setup using deflection method: (1) Polystyrene box as cover of the system, inside of which located the TFMS; (2) Autocollimator as reference system; (3) Mirror for reflecting the beam; (4) Tilt stage to provide tilt angles; (5) Standard weight of class E₂ added on the TFMS to cause the shift of COG; b) Simplified drawing from top view; c) Simplified drawing from side view.

The TFMS is located on the tilt stage (4) and fully covered by a polystyrene box (1) to keep the airflow out, moreover, for thermal and light isolation. The tilt stage provides the possibility to generate controllable tilt angle α_x and α_y around both x - and y -axis. An assumption (a) is made that at the initial state, the COG of all rotational components (plane wheel, adaptors with dummy weights carried by the flexible bearing hinge) lies in the rotational axis of the system, namely, no shift of COG exists. By applying a standard weight (5) on the arm of the TFMS with the arm length $r = L_{T1}$ (see figure 4.3 a

and b), the COG of the system is thereby displaced. Moreover, when the tilt stage generates a tilt angle α around y -axis, the tilt force F_t which is proportional to $\sin\alpha$ and the mass of the standard weight m is generated, acting at the point where the standard weight is applied as equation (4.2) denotes. As illustrated in the simplified drawings (b) and (c) the tilt force F_t operates as the actuation force and drives the plane wheel into motion.

$$F_a = F_t = m \cdot g \cdot \sin \alpha \quad (4.2)$$

A plane mirror (3) mounted on the plane wheel reflects the laser beam back to the autocollimator, enabling the detection of the tilt angle α and rotational angle θ as figure 4.3 (a) presents. The calibration factor K_{ps} is determined by comparing the rotational angle θ and the measured voltage U_p from the optical positioning sensor.

The assumption (a) is valid only under the condition that the mechanical components are in even density, additionally manufactured and assembled ideally symmetrically in geometry. Otherwise, due to the initial displacement of COG, the tilt force F_t' exerting on the system in reality can be deviated from the calculated force F_t using equation (4.2). As the displacement of COG caused by the imperfection during the manufacturing and assembling is an unknown value, the generated tilt force F_t' in reality is reproducible but not a traceable value. However, for the calibration of the positioning sensor aiming to transfer the electric voltage into rotational angle values as the output signal, generating the reproducible actuation force driving the wheel into controllable rotation is the focal point. The exact magnitude of the tilt force is currently not necessary to be under consideration, which means that the assumption (a) is currently acceptable for the position calibration.

4.1.3 Measurements

In the experiments, standard weight of $m = 1$ g from class E₂ is applied on the TFMS, and the tilt stage provides the tilt angle α_y round y -axis with step of 0.1 mrad in the range of ± 3 mrad. This results into the rotation of the plane wheel, which is detected by the optical positioning sensor with the output voltage U_p shown in figure 4.4 (a), and by the autocollimator at the same time with rotational angle θ shown in figure 4.4 (b). As illustrated in figure 4.4 (a), the optical positioning sensor presents linearity only in limited range. The relationship between U_p and the θ is presented in figure 4.4 (c), where the slope of the linear fitting represents the calibration factor K_{ps} . Thus, using this deflection method the calibration factor of the positioning sensor is $K_{ps} = (0.4285 \pm 0.0015)$ mrad V⁻¹ with coverage factor $k = 2$. The uncertainty is described by repeatability calculated by repeated measurements. Due to the linear fitting, the residual difference is within 48.99 μ rad in the linear range of ± 1.1 V illustrated in figure 4.4 (d). For the force measurement in this work, a measuring range of ± 20 μ N is sufficient to measure the Lorentz force induced by weakly conducting electrolyte. Therefore, the linear fitting is implemented within the application range, which is approximately ± 0.6 V shown in figure 4.4 (e). In this range, the residual difference is considerably better as within 4.05 μ rad. The calibration factor is thereby $K_{ps} = (0.4207 \pm 0.0012)$ mrad V⁻¹ and this value is taken in this work according to the local application.

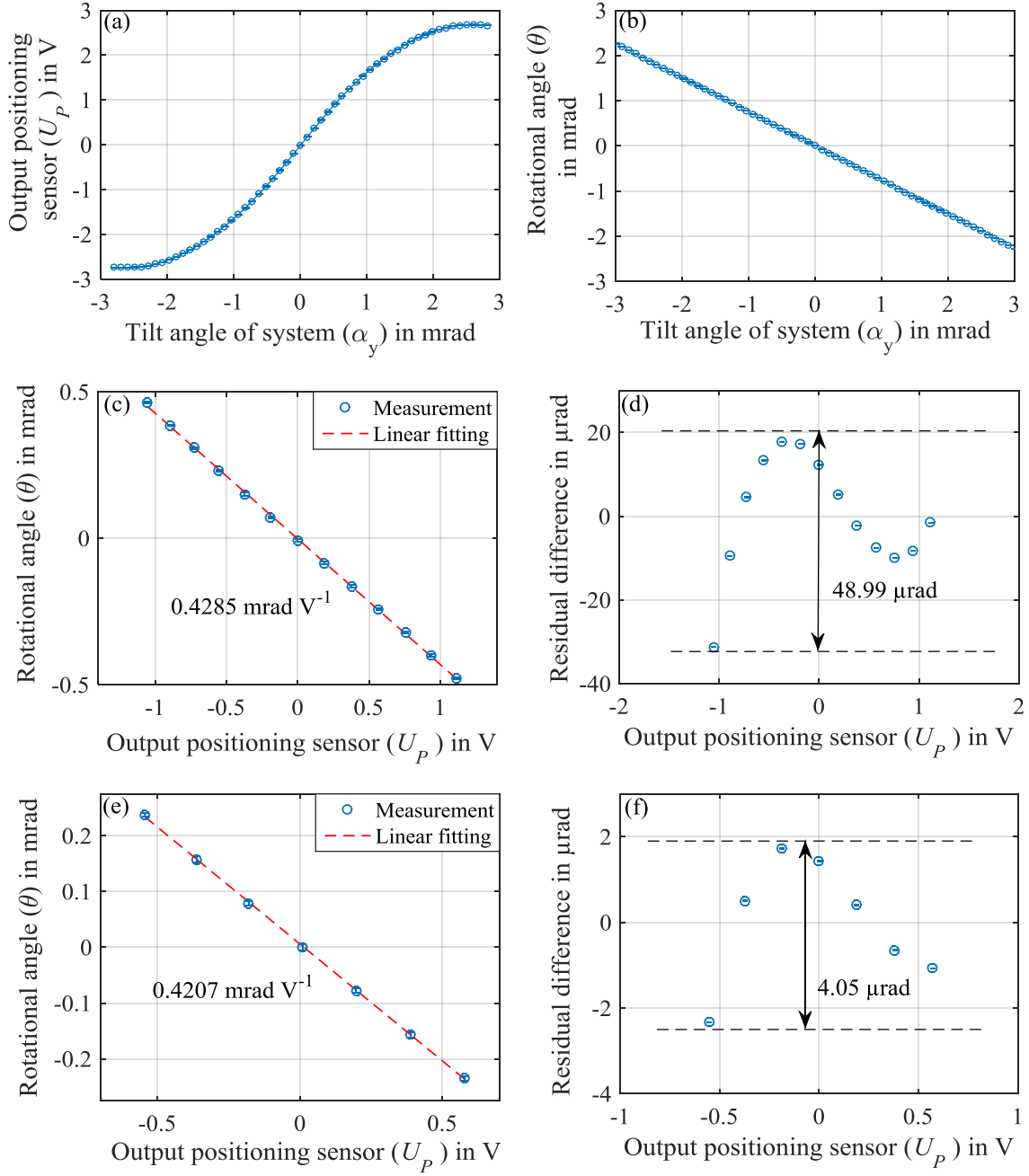


Figure 4.4: Measured data for position calibration using deflection method. (a) Output voltage of the positioning sensor U_P along with tilt angles; (b) Rotational angle θ detected by autocollimator along with tilt angles; (c) Linear fitting (in linear range) for determining the calibration factor; (d) Residual difference due to the linear fitting in (c); (e) Linear fitting (in application range) for determining the calibration factor; (f) Residual difference due to the linear fitting in (e).

Based on the calibration procedure described in block diagram in figure 4.1, the calibration factor K_{ps} is determined by the rotational angle θ and measured voltage U_P . The autocollimator is with a

resolution of 0.005" [40]. The voltage module NI 9239 with 24 bit resolution [39] is used to record voltage value, and the measurement uncertainty of it is 9.24 μV (see Appendix A). The value of the tilt angle α , mass of standard weight m and the arm length L_{T1} indicating where the weight is applied, these values are used to enable the motion of the TFMS, however, have no contribution into the calibration factor K_{ps} . In section 3.4, it was revealed that output of the positioning sensor is temperature depended, the relative uncertainty of 0.28% in the repeated measurements could be a summation effect caused by the temperature dependency of the positioning sensor and the measurement uncertainty of the devices, namely, the NI module and the autocollimator.

4.2 Force calibration using deflection method

In the previous section 4.1, the deflection method is introduced as a reproducible procedure to perform actuation force on the TFMS, which contributes into the position calibration procedure. Assumption (a) is made in section 4.1.2 under the condition that during the calibration of the position values, the reproducible motion of the TFMS is necessary but the exact magnitude of the generated tilt force is not required. However, the initial displacement of COG of the TFMS caused by imperfection in manufacture and alignment should be taken into consideration for further investigations, where the output signal of TFMS is also expected to be calibrated into force values with the aim to measure Lorentz forces. Therefore, the traceable value of the tilt force is required. Moreover, similar as measuring with EMFC weighing cell, the tilt sensitivity of the TFMS is desired to be minimized to reduce the measurement uncertainty. These will be introduced in this section.

4.2.1 Adjustment of the tilt sensitivity

In section 4.1.2, it is assumed that initially, COG of all the rotational components lies in the rotational axis of the system, in another word, $L_x = L_y = 0$. This is acceptable when used to calibrate the positioning sensor from electric voltage into rotational angles. In real cases, the shift of COG does exist and influences the measurement. However, the shift can be compensated by adding compensation mass pieces on the system. Although the shift, namely L_x and L_y , are unknown values, the motion of the TFMS during tilting is the observable outcome of the shift according to equation (4.1). The compensation of shift of COG is thereby enabled by measuring and adjusting the tilt sensitivity.

The tilt sensitivity of the TFMS is investigated and adjusted in this section. Similar approach as described in chapter 2 is carried out with the help of the tilt stage. The TFMS is located on the tilt stage as illustrated in figure 4.3, but initially without applying any additional standard mass pieces. Stepwise tilt angles α_x and α_y within ± 3 mrad are generated respectively, and the rotational angles of the plane wheel θ are recorded. Ideally the rotational angle θ should remain unchanged with different tilt angles α when the COG is identical with the PP. However, in the experiment the rotational angle θ changes linearly with the tilt angle α as figure 4.5 presents. Before any adjustment, the slope of the line, namely the ratio between the rotational angle θ and the tilt angle α_x is $T_{x1} = -5.6 \cdot 10^{-1}$ indicating the tilt sensitivity around x -axis; similarly, the tilt sensitivity around y -axis is $T_{y1} = 2.7 \cdot 10^{-1}$. Both values are not zero which indicates that the shift of COG exists in both x - and y -directions, $L_x \neq 0$ and $L_y \neq 0$.

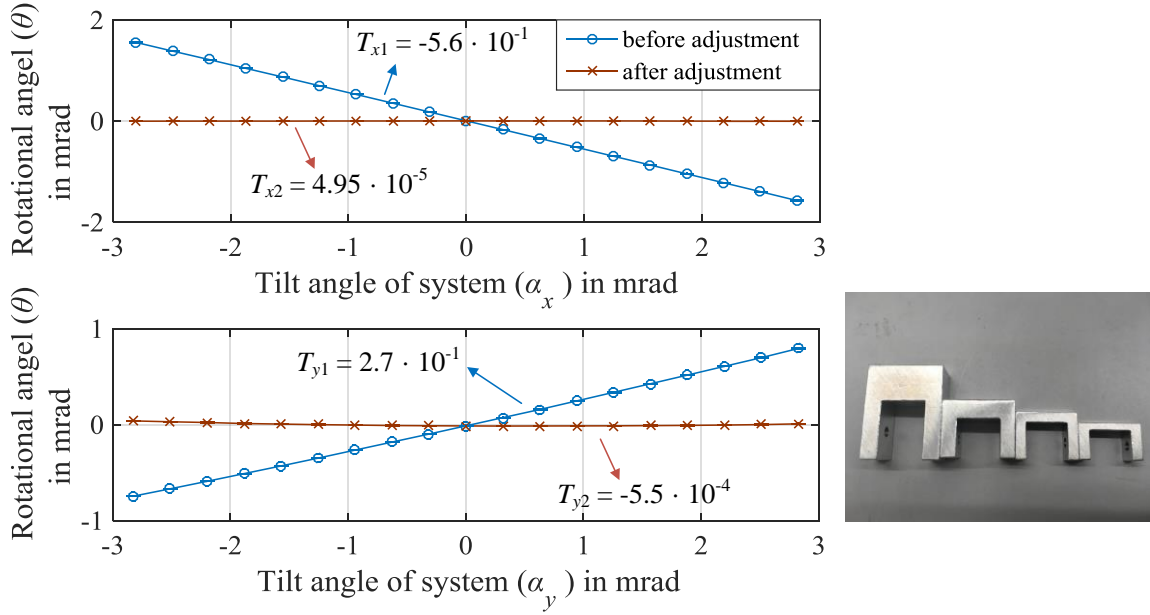


Figure 4.5: Tilt dependency of the TFMS before and after adjustment. (Top: tilt angle generated around the x -axis; bottom: tilt angle generated around the y -axis) and snapshot of the customized aluminum mass pieces for compensation the displacement of the COG.

With the sign and the magnitude of the obtained tilt sensitivity, the direction of the shift can be determined and the distance of COG displaced from the PP can be estimated. A set of customized aluminum components with various dimensions and mass values presented in figure 4.5 are used as compensation weights, which can be applied and fixed on the plane wheel to compensate the displacement of COG. Thus, the tilt sensitivity of the TFMS with compensation weight at different positions is determined until the tilt sensitivity is within the acceptable range. In one work of our institute [20], the inevitable tilt angle generated by people or environmental factors of approximately $\leq 1 \mu\text{rad}$ was revealed. The tilt of $1 \mu\text{rad}$ should not result into a position change of the aperture of more than 1 nm , which indicates the resolution of the positioning sensor. The calculated limit of tilt sensitivity is $1 \text{ nm } \mu\text{rad}^{-1}$, or $7.4 \cdot 10^{-3} \text{ rad rad}^{-1}$ (namely $7.4 \cdot 10^{-3}$) calculated with the distance R of 135 mm (see figure 3.1) from the aperture to the geometrical center of the system. The measurements and adjustment procedures are repeated until the tilt sensitivity is within the required range. As demonstrated in figure 4.5 and table 4.1, after the adjustment procedure with the aluminum compensation weights, the tilt sensitivity is minimized to $T_{x2} = 4.95 \cdot 10^{-5}$ and $T_{y2} = -5.5 \cdot 10^{-4}$, both are within the permitted range of $\leq 7.4 \cdot 10^{-3}$.

Table 4.1: Tilt sensitivity of the TFMS before and after the adjustment procedure.

Tilt sensitivity	around x	around y
Requirement	$< 7.4 \cdot 10^{-3}$	$< 7.4 \cdot 10^{-3}$
Before adjustment	$T_{x1} = -5.6 \cdot 10^{-1}$	$T_{y1} = 2.7 \cdot 10^{-1}$
After adjustment	$T_{x2} = 4.95 \cdot 10^{-5}$	$T_{y2} = -5.5 \cdot 10^{-4}$

4.2.2 Force calibration

Aiming to measure the Lorentz force, the TFMS should give force values as the output signal. Similar to that in the section 4.1, where the position calibration is carried out, the deflection method is also possible to be used for force calibration as indicated in figure 4.1. In the force calibration procedure, the tilt force F_t generated by deflection method should be not only reproducible, but the traceable value is also required. In order to generate controllable tilt force F_t , a set of defined tilt angles within specified limits are produced by the tilt stage in the range of several milliradians. Although the tilt sensitivity was minimized within the permitted range to enable an insensitive system to the unavoidable tilt angle caused by person or surroundings ($\leq 1 \mu\text{rad}$), the influences caused by the remaining tilt sensitivity around both x - and y -axis after the adjustment could not be entirely ignored at the range of milliradians in the calibration procedure. In this set of measurements, due to the direction of the Lorentz force in the LFV application, the tilt angles are only necessary to be created around y -axis. Furthermore, the TFMS is carefully aligned to the axes of the tilt stage to avoid the cross-sensitivity. Thus, the term $\sin\alpha_x$ in equation (4.1) could be considered zero. Only the shift of COG along y -axis (L_y) needs to be considered.

After the adjustment procedure presented in the section 4.2.1, taking in consideration the remaining tilt sensitivity (also refers remaining displacement of COG), force calibration using the deflection method is implemented in the following three steps:

i) Without adding known weights

The experimental facility of force calibration is the same as that of position calibration presented in figure 4.3. Initially, no additional standard weight (component (5) in figure 4.3) is placed on the TFMS. The tilt stage provides the stepwise tilt angle α_y in the range of $\pm 3 \text{ mrad}$, the motion of the TFMS is recorded. This motion is a result of the remaining tilt sensitivity T_{y2} caused by the remaining displacement of COG L_{y2} , which was minimized in the permitted range but still a non-zero value. As introduced in section 4.1.1, the remaining displacement L_{y2} and the tilt angle α_y lead to the torque M_z^* presented in equation (4.3):

$$M_z^* = m^* \cdot g \cdot \sin \alpha_y \cdot L_{y2} \quad (4.3)$$

m^* indicates the total mass of the rotational components of TFMS, together with the customized aluminum compensation weights on the wheel used to adjust the tilt sensitivity. After the adjustment in section 4.2.1, the value L_{y2} is a relatively small but unknown value. However it can be described by the measured signal. The torque M acting on the system is proportional to the output voltage U_p of the positioning sensor, which can be directly measured by the NI device. The factor K_m is introduced as:

$$M = K_m \cdot U_p \quad (4.4)$$

Therefore, the equation (4.3) can be transferred into equation (4.5).

$$M_z^* = m^* \cdot g \cdot \sin \alpha_y \cdot L_{y2} = K_m \cdot U_{p1} \quad (4.5)$$

U_{p1} is the voltage change during motion of the TFMS caused by remaining tilt sensitivity, and is recorded by the NI voltage module.

ii) With additional known weights

In the second step, traceable external force is applied on the TFMS by adding known mass standard m at a certain position on the wheel with the arm length L_{T2}' along y -axis, this arm length indicates the position where the force will act in the LFV application. Theoretically, L_{T2}' is equal to L_{T2} in figure 3.1, both of which are 180 mm. However, deviation can exist because of the uncertainty of manual operation. In this work, the maximum permissible error of the position where the known weight applied is assumed as 0.5 mm. With the applied known mass standard on the TFMS, the torque M_z caused by the tilt sensitivity is a summation of two effects: one generated by the remaining shift of COG after the adjustment procedure; and another by the applied known standard mass piece m . Similarly, the torque can be described with equation (4.6):

$$M_z = g \cdot \sin \alpha_y \cdot (m^* \cdot L_{y2} + m \cdot L_{T2}') = K_m \cdot U_{p2} \quad (4.6)$$

U_{p2} is the voltage value from the positioning sensor during the motion caused by tilt.

iii) Difference between step i) and ii)

Subtracting equation (4.5) from equation (4.6), the difference is:

$$M_{diff} = M_z - M_z^* = g \cdot \sin \alpha_y \cdot m \cdot L_{T2}' = K_m \cdot U_{p2} - K_m \cdot U_{p1} \quad (4.7)$$

And the introduced factor K_m can be calculated as:

$$K_m = \frac{m \cdot g \cdot \sin \alpha_y \cdot L_{T2}'}{U_{p2} - U_{p1}} \quad (4.8)$$

Since the TFMS is developed to measure force values, the calibration procedure primarily aim to determine the necessary force calibration factor K_F , by which the output voltage of the position sensor can be converted into forces that act on the magnet system at the effective arm length L_{T2} , equations (4.9) and (4.10) are shown.

$$\mathbf{M} = \mathbf{L}_{T2} \times \mathbf{F}; \quad F = K_F \cdot U_P; \quad M = K_m \cdot U_P$$

$$\text{and} \quad K_F = \frac{K_m}{L_{T2}} \quad (4.9)$$

4. TFMS in the open-loop operation mode

Therefore,

$$K_F = \frac{m \cdot g \cdot \sin \alpha_y \cdot L_{T2}'}{(U_{P2} - U_{P1}) \cdot L_{T2}} \quad (4.10)$$

Each parameter at the right hand side of the equation (4.10) is either known value or measurable. The force calibration factor K_F can be thereby experimentally determined.

The experimental facility used for force calibration remains the same as figure 4.3 presents and the standard weight of $m = 1 \text{ g}$, 2 g and 4 g (as combination of two pieces of 2 g) are added on the TFMS with the arm length L_{T2}' respectively. With different tilt angle α_y , and the mass of the standard weight m , the tilt force F_t is calculated and the corresponding output voltage from the positioning sensor is recorded and presented in figure 4.6. Linear fitting is applied to the measured data and the slope of the fitting indicates the factor K_F , with which the output of the TFMS can be calibrated into force values. In figure 4.6, the measured data with different applied standard weights match each other well. The force calibration factor determined as the mean value of the set of experiments is following with the uncertainty determined as the repeatability by repeated measurements.

$$K_F = 30.07 \pm 0.2 \mu\text{N V}^{-1} (k = 2)$$

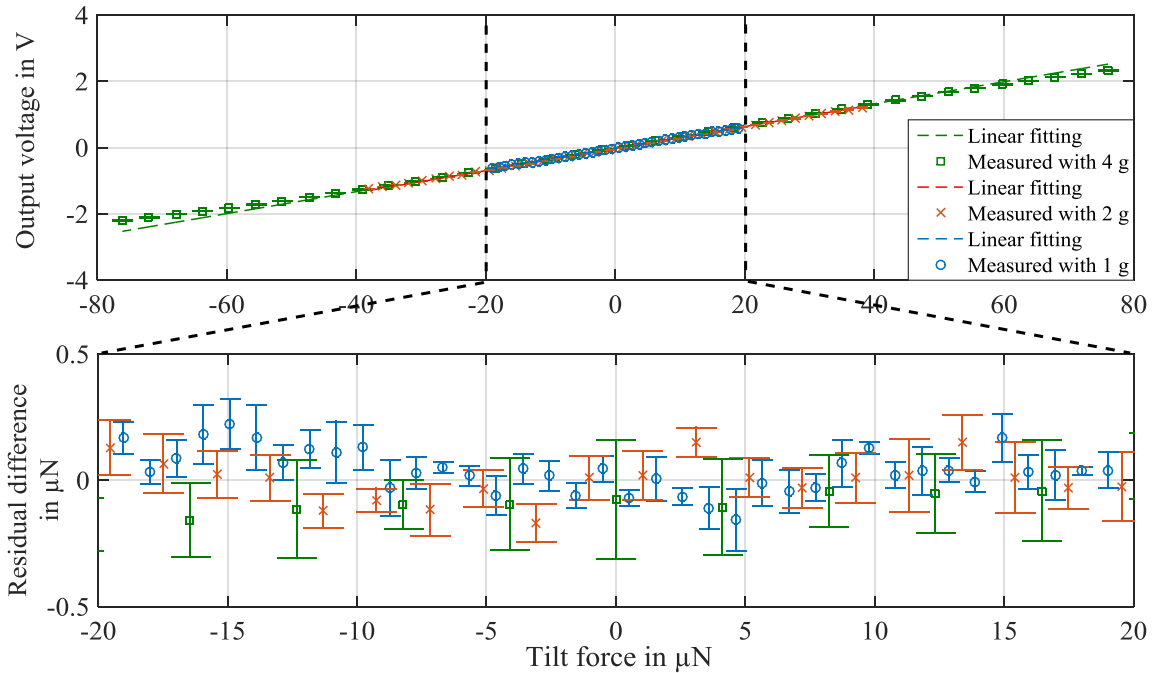


Figure 4.6: Experimentally measured data to determine force calibration factor K_F . (Top: output voltage along with calculated tilt force in full range of $\pm 80 \mu\text{N}$; Bottom: residual difference in the application range of $\pm 20 \mu\text{N}$; blue with circle marker: tilt force generated by mass 1 g ; red with cross marker: tilt force generated by mass 2 g ; green with square marker: tilt force generated by 4 g mass piece).

During the rotational motion of the TFMS driven by the tilt force, the rotational angles θ_1 in step i) and θ_2 in step ii) are also recorded by the autocollimator. The spring constant of the flexible bearing C_b can be thereby experimentally determined by equation (4.11):

$$C_b = \frac{M_z - M_z^*}{\theta_2 - \theta_1} = (1.34 \pm 0.01) \cdot 10^{-2} \text{ N m rad}^{-1} \quad (4.11)$$

The spring constant given by the manufacturer is $1.17 \cdot 10^{-2} \text{ N m rad}^{-1}$ without information about calibration and uncertainties. The experimentally determined spring constant during the force calibration using the deflection method is $(1.34 \pm 0.01) \cdot 10^{-2} \text{ N m rad}^{-1}$ with 14.5% deviation from the given value of the manufacturer. Additionally, the experimentally determined stiffness of the system is thereby 0.55 N m^{-1} also deviated from the theoretical calculation of 0.48 N m^{-1} using equation (3.3).

4.2.3 Uncertainty discussion

The uncertainty of the determined force calibration factor K_F using the deflection method is obtained by the parameters on the right side of the equation (4.10). The applied known mass piece is from the weight-set class E₂. The maximum permissible error of the mass m of 1 g is 0.03 mg according to the international recommendation OIML R111-1 [42]. The value of g is taken from the certificate, as once the local gravitational acceleration was measured in the laboratory [43]. The tilt angle α_y is generated by the tilt stage and recorded by the autocollimator and the uncertainty is determined from the repeatability with the normal distribution. The L_{T2}' describing the position of the added mass standard, is theoretically equal to L_{T2} , but could be deviated within $\pm 0.5 \text{ mm}$ due to the manual operation. Similar to the tilt angle, the voltage U_P is also measurable and its uncertainty is described by the repeatability. Table 4.2 shows the uncertainty budget of the obtained calibration factor considering the contribution of all the parameters in equation (4.10). The relative uncertainty in the determined force calibration factor K_F is 0.76 % with the coverage factor $k = 2$.

Table 4.2: Uncertainty budget of the obtained force calibration factor.

Quantity	Value	Standard Uncertainty	Distribution	Sensitivity coefficient	Index
m [kg]	$1 \cdot 10^{-3}$	$1.73 \cdot 10^{-8}$	Rectangular	30000	0 %
g [m s^{-2}]	9.81015772	$0.11 \cdot 10^{-6}$	Normal	3.1	0 %
α_y [rad]	$2.04 \cdot 10^{-3}$	$0.20 \cdot 10^{-6}$	Normal	15000	0 %
L_{T2}' [m]	0.18	$2.89 \cdot 10^{-4}$	Rectangular	0.17	17.6 %
U_{P2} [V]	0.67	$2.3 \cdot 10^{-3}$	Normal	-45	81.7 %
U_{P1} [V]	$4.96 \cdot 10^{-3}$	$2 \cdot 10^{-4}$	Normal	45	0.6 %
Result:		$K_F = 30.07 \pm 0.23 \text{ } \mu\text{N V}^{-1} \quad (k = 2)$			

The result according to the uncertainty budget shows that the measured voltage U_p has the most contribution to the calibration factor. The position parameter L_{T2}' contributes with 17.6 %. Because the uncertainty of U_p is in the normal distribution, a possible way to reduce the uncertainty is to arrange more repeated measurements to reduce the repeatability. Reducing the uncertainty in L_{T2}' may be achieved in further work where automatic mechanism for loading and unloading may be introduced.

4.3 System identification

In section 4.2, the force calibration factor is determined with the deflection method. The TFMS is thereby able to output force values. Based on the theoretical calculation in section 3.1, the undamped resonance frequency of the TFMS is low as 0.06 Hz, which is caused by the high dead load and the low stiffness of the system. In the open-loop operation mode, the TFMS could be considered as a mass-spring-damper system whose damping ratio ζ is smaller than 1; in other words, the system is underdamped and the transfer function can be written as:

$$G(s) = \frac{\omega_n^2}{s^2 + 2\zeta\omega_n s + \omega_d^2} \quad (4.12)$$

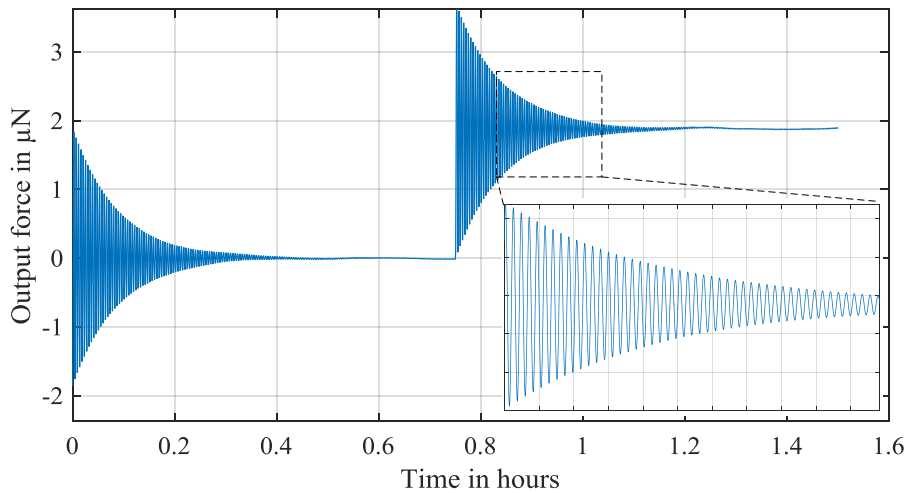


Figure 4.7: Step response of the TFMS in open-loop operation mode. Insert figure: zoom of the oscillation procedure.

The dynamic behavior and the parameters in the transfer function can be obtained from the step response. In the experiment, the TFMS is excited by the external force into the durable oscillation and reaches a stable state after about 20 minutes as presented in figure 4.7. The overshoot in the step response is 95%, by which the damping ratio of the system is determined as 0.0163. The peak time is 9.36 s and thereby the undamped natural frequency of the system ω_n is $0.3357 \text{ rad s}^{-1}$ (0.053 Hz), which matches the theoretically calculated 0.06 Hz in equation (3.4). The parameters to determine the transfer function are shown in table 4.3. The transfer function of the TFMS in the open-loop operation mode can be written as:

$$G(s) = \frac{\omega_n^2}{s^2 + 2\zeta\omega_n s + \omega_d^2} = \frac{0.1127}{s^2 + 0.011s + 0.1126}$$

Table 4.3: Parameters determined by step response for obtaining the transfer function.

Term			Value
Percent overshoot	PO	$= \frac{y_{\max} - y_{ss}}{y_{ss}} \cdot 100\%$	95%
Peak time	T_p	---	9.36 s
Damping ration	ζ	$PO = \exp\left[\frac{-\zeta\pi}{\sqrt{1-\zeta^2}}\right]$	0.0163
Natural frequency	ω_n	$= \frac{\pi}{T_p \sqrt{1-\zeta^2}}$	0.3357 rad s ⁻¹
Damped natural frequency	ω_d	$= \omega_n \sqrt{1-\zeta^2}$	0.3356 rad s ⁻¹
Settling time (with 5% error tolerance)	τ	$= \frac{\ln(0.05\sqrt{1-\zeta^2})}{\zeta \cdot \omega_d}$	547 s

In figure 4.8, the Bode diagram obtained using the transfer function is presented to describe the dynamic behavior of the TFMS in its open-loop operation mode. In the upper figure, near the natural frequency the magnitude of the signal is distorted; in a frequency range higher than the natural frequency, the magnitude is attenuated strongly. The cutoff frequency, which describes that the response of the external load remains in the permissible error band of the final normalized value, is necessary to be defined. Corresponding to the settling time, the cutoff frequency within the 5% error tolerance is 0.002 Hz. Based on this value, a PID-controller is expected to be built with which the TFMS can operate in the closed-loop operation mode where the dynamic behavior of the TFMS is improved.

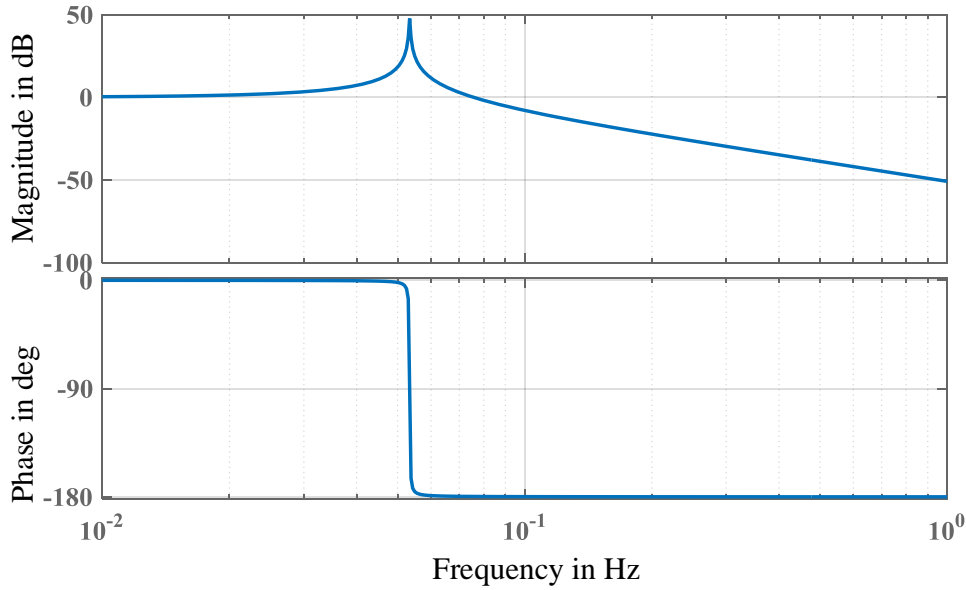


Figure 4.8: Bode diagram of the TFMS in the open-loop operation mode.

4.4 Summary

In this chapter, the position calibration and force calibration using the deflection method were carried out. The deflection method, based on the behavior of the system during tilt, is introduced to generate tilt force operating as the actuation force. By applying known mass piece on the TFMS, the displacement of COG can be controlled. Moreover, the tilt angle provided by the tilt stage is detected by the autocollimator, which leads to the tilt force as a reproducible and also traceable value.

The initial output voltage of the positioning sensor is compared with the rotational angle from autocollimator during the reproducible motion of the wheel. The position calibration factor is thereby determined as $K_{ps} = 0.4207 \pm 0.0012 \text{ mrad V}^{-1}$ ¹. Considering the imperfection could exist during the manufacturing and assembling of the mechanical components, the tilt sensitivity of the TFMS was tested and minimized into a permitted range for precise force measurement. Afterwards, the output of the TFMS was calibrated into force values and the force calibration factor was determined as $K_F = 30.07 \pm 0.23 \text{ } \mu\text{N V}^{-1} (k = 2)$ ². In this procedure, it should be noticed that after the adjustment, the remaining tilt sensitivity is minimized but still a non-zero value. The influence of the remaining tilt sensitivity during the calibration procedure is eliminated by running the same procedure with and without known mass piece; and then taking the data evaluation. Additionally, the spring constant of the commercial flexible bearing as well as the stiffness of the TFMS was determined experimentally in the force calibration procedure. Both values are with deviation from the theoretical calculation. The reason is that in the previous calculation, the value of the spring constant is chosen as it is given by the manufacturer, which is a value without information about calibration and uncertainty; therefore the value could be with large deviation.

In the open-loop operation mode, the external force acting on the TFMS is determined by converting the electric voltage values into force values based on the calibration factor K_F . The transfer function of the TFMS in the open-loop operation mode was determined with the step response. The high dead

load and low stiffness of the system lead to a low natural frequency; additionally, the damping ratio of the TFMS is also low as 0.0163. Both effects result into the long response time of over 500 s. With the aim to improve the dynamic behavior, the closed-loop operation mode based on the PID-controller is set up, which will be introduced in the chapter 5.

^{1,2} *The value differs from that determined in the previous work [44], because the TFMS was once disassembled for another low temperature test. The geometry could change after reassembling.*

5. TFMS in the closed-loop operation mode

In chapter 4, experiments and calculations were carried out on the TFMS to determine the transfer function in its open-loop operation mode. Aiming to improve the dynamic properties of the TFMS, the closed-loop operation mode is set up. Figure 5.1 presents an overview of the work in this chapter.

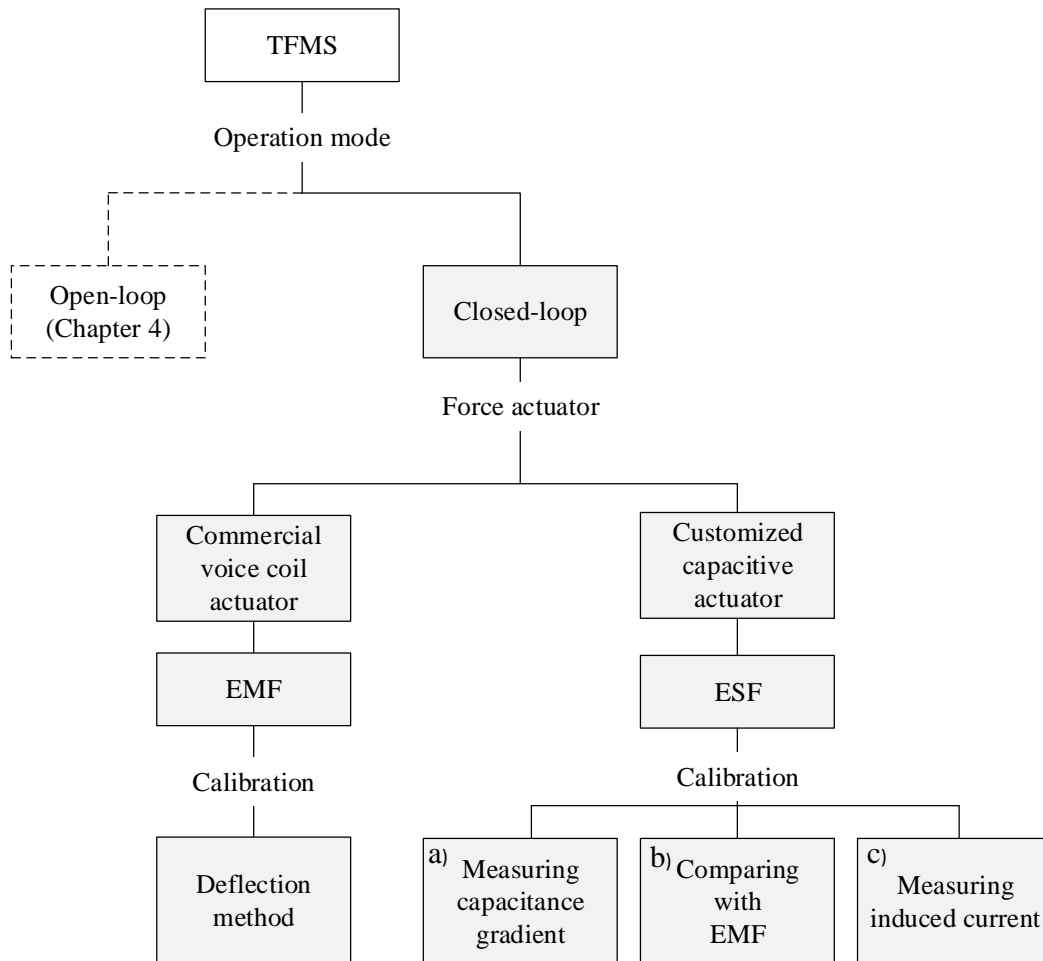


Figure 5.1: Block diagram giving an overview of work in chapter 5. The closed-loop operation mode is set up based on PID-controller. Commercial voice coil actuator generates electromagnetic force (EMF) as the compensation force. The EMF is calibrated using deflection method. The customized capacitive actuator is built to provide electrostatic force (ESF) as an alternative way to perform compensation force. The ESF is calibrated with three methods which will be introduced in section 5.3.

The closed-loop operation mode is set up in section 5.1, with electromagnetic force (EMF) as the compensation force by using a commercial voice coil actuator. The force constant of the voice coil actuator is determined using the deflection method. In section 5.2, a customized plate-shaped capacitor

is introduced to generate the electrostatic force (ESF), which is considered as a reasonable replacement of the EMF. Afterwards, three methods for the calibration of the ESF are introduced in the section 5.3, they are:

- a) Calibration by measuring capacitance gradient;
- b) Calibration by comparing with the EMF as the reference force;
- c) Calibration by measuring induced current when the TFMS operates in a velocity mode.

At the end of this chapter, the dynamic and static properties of the TFMS are tested respectively in section 5.4 and 5.5.

5.1 Setting up PID-controller using electromagnetic force

In the open-loop operation mode presented in figure 5.2, the motion of the TFMS caused by external force is detected by the positioning sensor. The force value is calculated from the initial output voltage U_P and the calibration factor K_F determined in section 4.2.

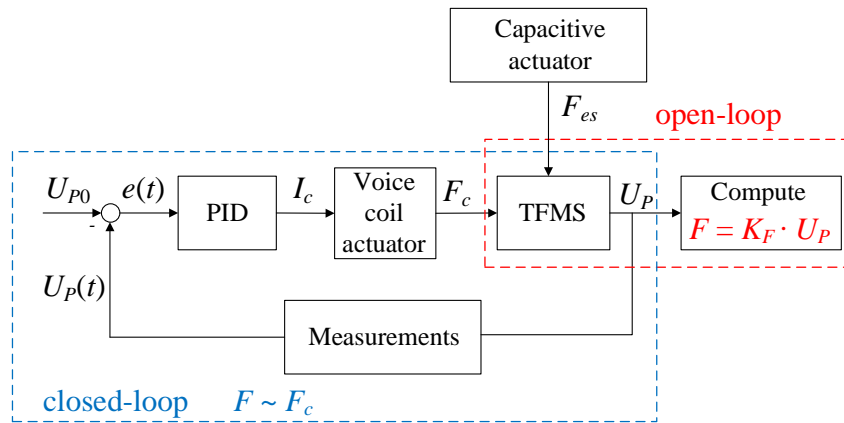


Figure 5.2: Block diagram of the TFMS in the open-loop operation mode and closed-loop operation mode using PID-controller.

As a result of the dead load caused by the dummy weights and the low stiffness enabled by the sensitive flexible bearing, the undamped natural frequency of the system is as low as approximately 0.06 Hz. Moreover, the damping ratio of the TFMS is also minimal at 0.0163, which leads to the durable oscillation when the TFMS is excited by external signal as figure 4.7 presents. In the measurement of static force with the load frequency ≤ 0.002 Hz, the open-loop operation mode is acceptable. However, when the load frequency is higher than 0.002 Hz, the magnitude of the output starts to be distorted, and damped strongly when the load frequency is higher than 0.06 Hz. In the LFV application to monitor the production process, the mean velocity of the conducting flows is quasi constant leading to the static Lorentz force. Therefore, the dynamic property of the force measurement system is not a crucial point. However, the dynamic behavior is still expected to be improved under the premise that force resolution is maintained. The closed-loop operation mode is set up based on the PID-controller.

As demonstrated in figure 5.2, similar to the working principle of the EMFC weighing cell, in the closed-loop operation mode the deflection of the TFMS caused by external force is continuously compensated by force F_c . A commercial voice coil actuator similar to the one integrated inside the EMFC weighing cell, is utilized to generate the electromagnetic compensation force. The voice coil actuator consists of a magnet and coil wire immersed in the magnetic field. The voice coil actuator is assembled to the TFMS as presented in figure 5.3: the coil wire is screwed on the arm of the plane wheel while the magnet is carefully aligned to the coil and fixed on the base plate. By supplying electric current I_c to the coil, the electromagnetic force based on equation (1.4) is generated between the coil and magnet, namely, the electromagnetic force acts on the TFMS. The original power cables of the coil provided by the manufacturer are replaced by the very thin copper wires with the diameter of 50 μm , carrying the electric current I_c in the range of microampere supplied by the universal source HP 3245A [46]. As the coil is assembled to the rotational component of the TFMS, reducing the diameter of the cables by using the thin wires can minimize the undesired forces caused by the stiffness of the cables. Exchanging the position of the magnet and the coil is not desired as the magnetic interaction could influence the motion of the TFMS when the magnet is assembled on the plane wheel.

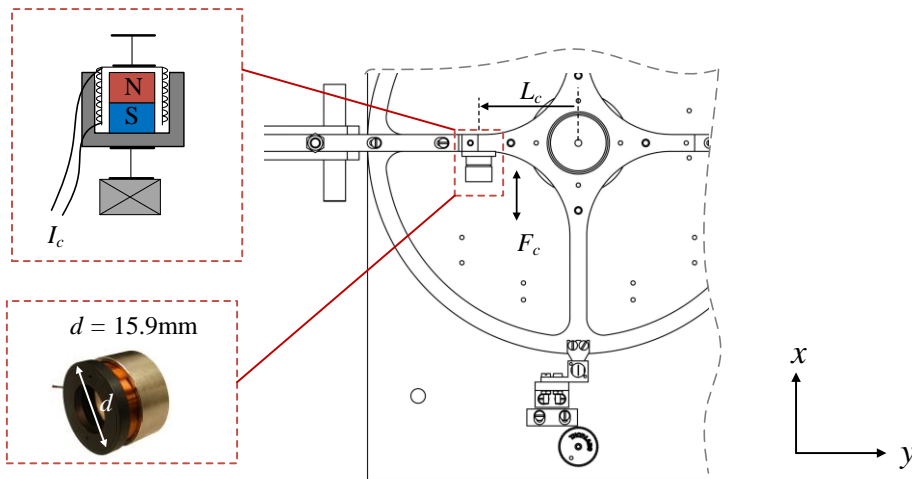


Figure 5.3: Commercial voice coil actuator assembled on the TFMS, providing electromagnetic compensation force for the closed-loop operation mode.

The PID-controller is used to calculate the required compensation current I_c in order to perform the compensation procedure. As demonstrated in figure 5.2, initially a voltage value U_{P0} is defined for the null position of the plane wheel. The value U_{P0} can be manually given as zero indicating the geometrical center position or any other non-zero values indicating offset from the geometrical center. The value of U_{P0} can also be taken as the mean value of a period of pre-measurement in the open-loop operation mode, which describes the natural static position of the TFMS. When the wheel deflects from the defined null position due to external forces, the value $e(t)$ as the difference between the real time measured voltage $U_p(t)$ and the defined value U_{P0} is calculated and transferred to the PID-controller to determine the compensation current I_c . The parameters of the PID-controller is firstly determined with MatLab application *system identification* based on the step response of the TFMS in

its open-loop, and adjusted then experimentally to obtain faster response and also stability. The electric current I_c is applied to the commercial voice coil actuator to generate the electromagnetic force as the compensation force F_c bringing the TFMS from deflection back to its null position.

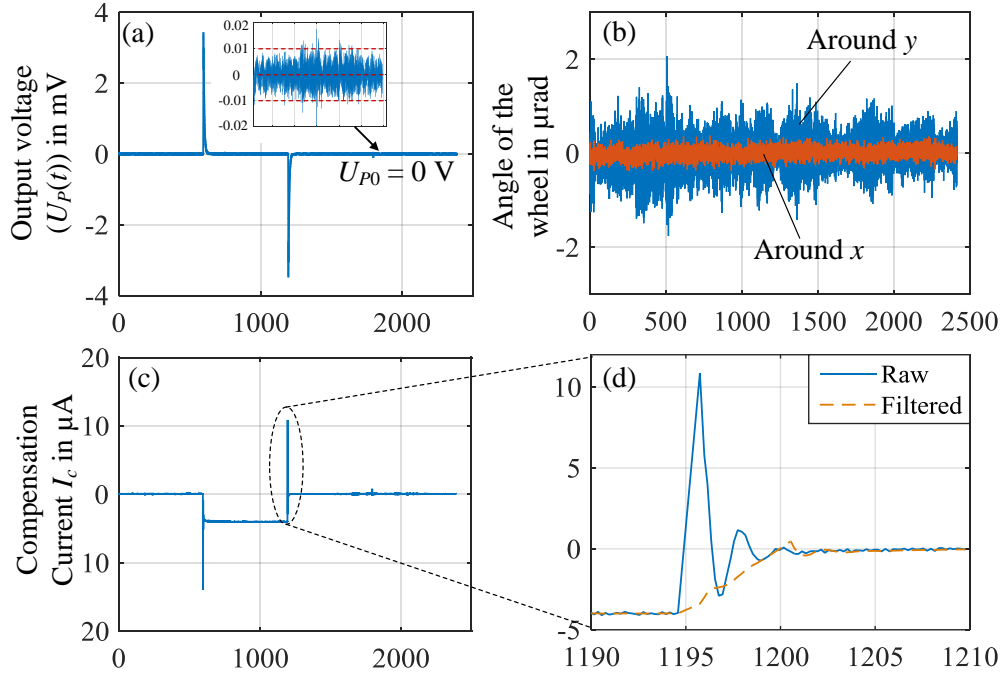


Figure 5.4: Step response of the TFMS in the closed-loop operation mode based on PID-controller and electromagnetic compensation force. (a) Output voltage of the positioning sensor $U_P(t)$ indicating that the wheel is continuously compensated back to the null position; (b) Motion of the plane wheel around x - and y -axis detected by the autocollimator which indicates that the plane wheel remaining stable in the xy -plane; (c) Compensation current I_c for generating compensation force; (d) Highlighted control procedure. The horizontal scale of all four figures is given as: Time in seconds.

Figure 5.4 presents the experimental data describing the control procedure. The TFMS in the closed-loop operation mode is excited by external force. Figure 5.4 (a) presents the output voltage $U_P(t)$ indicating the position of the plane wheel. Due to the PID-controller, the plane wheel is continuously compensated back to the null position which is defined by the voltage U_{P0} . In this test, the U_{P0} is given as 0 V as demonstrated in the insert figure. The measured $U_P(t)$ oscillates around the value U_{P0} in the range of $\pm 10 \mu\text{V}$, which can be considered as stable due to that the voltage value of $10 \mu\text{V}$ corresponds to the position change of < 1 nm. The figure 5.4 (c) presents the required compensation current I_c to compensate the deflection caused by external forces, and the highlighted control procedure is presented in figure 5.4 (d). In this experiment, the settling time of the TFMS in closed-loop operation is about 9.2 s with 5% error tolerance. Additionally, in the test of the closed-loop operation mode, the autocollimator is assembled to the system in a suspended configuration, aiming to record the undesired motion of the plane wheel around x - and y -axis. The measured data shown in figure 5.4 (b) presents a stable signal with a standard deviation of 0.06 arcsec and 0.1 arcsec of the

rotational angle around x - and y -axis, which proves that during operation the wheel remains considerably stable in the xy -plane.

After setting up the closed-loop operation mode, the measured force values are no longer calculated with the output voltage U_P and the calibration factor K_F , but described by the compensation force F_c , which is obtained by the compensation current I_c and the force constant of the voice coil actuator K_{vc} . The force constant of the actuator given by the manufacturer is $K_{vc} = 1.1 \text{ N A}^{-1}$ [45]. However, in real cases the force constant could deviate from the given value because of alignment errors and different immersion depths of the coil into the magnetic field. For example, in work [29], the force constant of the same voice coil actuator was determined as 0.93 N A^{-1} . In [47] the force constant with different immersion depths of a similar kind of actuator is tested with a micro stage and the EMFC weighing cell. In that test, the measured data reveals that a change of 1 mm in the immersion depth leads to the relative change in force constant of more than 2.5%. Therefore, after local alignment and assembling, the force constant of the voice coil actuator used in this work is expected to be determined. This procedure can also be achieved by using the deflection method introduced in chapter 4. The traceable tilt force is generated on the TFMS by using tilt stage and the standard weight. In this experiment, the PID-controller is switched on. The required compensation current I_c is continuously recorded during the compensation of the tilt force. The force constant of the voice coil actuator K_{vc} in the work is determined experimentally as:

$$K_{vc} = \frac{m \cdot g \cdot \sin \alpha \cdot L_{T1}}{I_c \cdot L_c} \quad (5.1)$$

The result presented in table 5.1 is obtained concerning the uncertainty contribution of the following parameters:

- The mass m is 1 g standard weight piece from class E₂, the maximum permissible error is 0.03 mg;
- The gravitational acceleration g was once measured in the laboratory locally, the value and its uncertainty are taken from the certificate;
- The tilt angle α is measured by the autocollimator, the mean value and uncertainty are determined by repeated measurements.

The three parameters mentioned above determine the quality of the generated tilt force.

And additionally:

- The compensation current I_c is also determined as the mean value of repeated measurements;
- The arm length of the voice coil actuator L_c , and L_{T1} indicating the position where tilt force is applied, the permissible error of both is 0.5 mm.

The uncertainty budget presents that the uncertainty in the obtained force constant comes mostly from the repeatability of the compensation current. The force constant of the voice coil actuator with the local alignment is experimentally determined as $K_{vc} = 0.869 \pm 0.038 \text{ N A}^{-1}$. Thus, the compensation

current I_c presented in figure 5.4 (c) can be transferred to force values and TFMS can output forces in the closed-loop operation mode.

Table 5.1: Uncertainty budget of the force constant K_{vc} of the voice coil actuator.

Quantity [unit]		Value	Standard Uncertainty	Distribution	Sensitivity coefficient	Index
m	[kg]	$1 \cdot 10^{-3}$	$1.73 \cdot 10^{-8}$	rectangular	870	0 %
g	[m s ⁻²]	9.81015772	$0.11 \cdot 10^{-6}$	normal	0.089	0 %
α	[rad]	$6 \cdot 10^{-3}$	$0.351 \cdot 10^{-6}$	normal	150	0 %
L_{T1}	[mm]	180	0.289	rectangular	0.0048	0.6 %
L_c	[mm]	59.5	0.289	rectangular	-0.015	5.2 %
I_c	[A]	$2.05 \cdot 10^{-4}$	$4.22 \cdot 10^{-6}$	normal	-4200	94.2 %
Result		$K_{vc} = 0.869 \pm 0.038 \text{ N A}^{-1}$ ($k = 2$) (relative uncertainty: 4.4 %)				

5.2 Setting up electrostatic force generator

By setting up the closed-loop operation mode based on PID-controller, the dynamic property of the TFMS is improved. However, there are still some imperfections by using the electromagnetic force as the compensation force because: (1) the stiffness of the thin copper wires as the power cables of the voice coil actuator is small but not zero. Motion of the wires can influence the measurement of the TFMS; (2) in the later application as part of the LFV, a magnet system is involved which is supported by the TFMS, providing the magnetic field and carrying the force to be measured. Under this condition, by using the voice coil actuator, electromagnetic interaction can influence the measurement; (3) the TFMS developed in this work is expected to be reduced in dimensions to build a second generation system. In the future, the second generation system will cooperate with high-temperature superconducting (HTS) bulks as quasi-permanent magnets [48], replacing the current used magnet system. In the design concept, the second generation TFMS together with the HTS bulks will be assembled inside a cryostat and brought to magnetization in the strong magnetic field, in which case the voice coil actuator as part of the TFMS will be also magnetized and not in the condition to provide traceable compensation forces. Due to the three reasons mentioned above, the voice coil actuator is thereby urged to be replaced. The development introduced in this section intends to find a reasonable replacement of the voice coil actuator, namely, to find other kinds of force which could operate as the compensation force for the TFMS and replace the electromagnetic force.

In several researches on small force metrology [12-18], the electrostatic force has been introduced. A brief introduction is presented earlier in section 1.2.1. By applying actuation voltage U_a across the two electrodes of the capacitor, electrostatic force F_{es} is induced between the two electrodes as equation

(5.2) presents. Based on the mechanical construction of the TFMS, a customized capacitive force actuator is set up and is introduced in this section.

$$F_{es} = \frac{1}{2} \cdot \frac{dC}{dx} \cdot U_a^2 \quad (5.2)$$

All the mechanical components of the TFMS are made of metal: dummy weights made of copper, the commercial flexible bearing from stainless steel, the material of all the other mechanical components manufactured in the workshop from aluminum AW 7075 alloy. Moreover, all screws for fixing are from brass. This makes the TFMS as one conductor, which can be further considered as one electrode of a capacitor. A rectangular printed circuit board (PCB) presented in figure 5.5(b) is fixed near and facing the dummy weight and connected to the anode of the signal generator as demonstrated in figure 5.5. The base plate of the TFMS is grounded and connected to the cathode of the signal generator. Since the TFMS is one conductor, the electric potential at each part of the TFMS is same and equals to the cathode. The PCB as one electrode, the section of the dummy weight facing against the PCB as the second electrode and together with the air in between is in the structure of a plate-shaped capacitor. Electrostatic force F_{es} is induced by applying the actuation voltage U_a across the two electrodes. Thus, the customized capacitive force actuator is built without assembling additional components on the rotational part of the TFMS. Electrostatic force is controllable by adjusting the actuation voltage U_a .

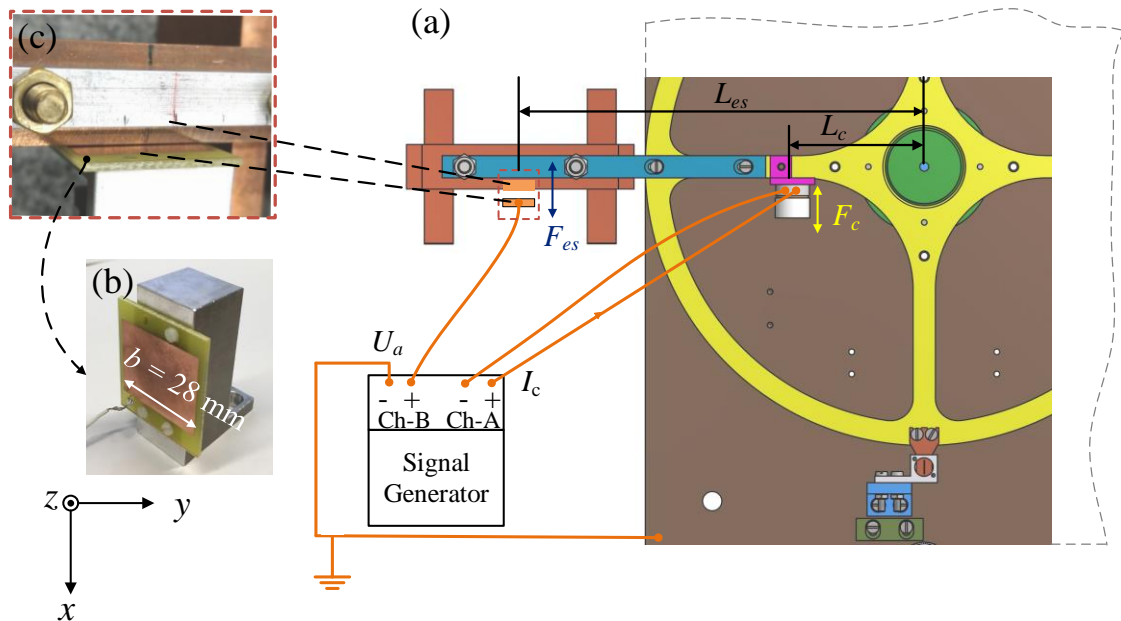


Figure 5.5: Setting up a capacitive actuator to generate electrostatic force on the TFMS. (a) Overview. (b) The customized rectangular PCB plate. (c) The PCB is located facing the dummy weight with a small distance, in between is air. By supplying actuation voltage across the PCB and TFMS, the electrostatic force is thereby generated.

5.3 Calibration of electrostatic force

Equation (5.2) indicates that the induced electrostatic force F_{es} is proportional to the second power of the applied actuation voltage U_a across the two electrodes, and the calibration factor K_{es} depends on the capacitance gradient described by equation (5.3):

$$F_{es} = K_{es} \cdot U_a^2 \quad \text{with} \quad K_{es} = \frac{1}{2} \cdot \frac{dC}{dx} \quad (5.3)$$

To actuate traceable electrostatic force, the calibration factor K_{es} is necessary to be determined. In this section, three methods are introduced to implement the calibration of the electrostatic force. The block scheme describing the following three methods is shown in figure 5.6, they are:

- Determining the force calibration factor K_{es} by measuring capacitance values with different distances between the two electrodes (determining capacitance gradient);
- Determining the force calibration factor K_{es} by comparing the electrostatic force with the reference force -- electromagnetic force;
- Determining the force calibration factor K_{es} by measuring induced current during the TFMS operating in a velocity mode.

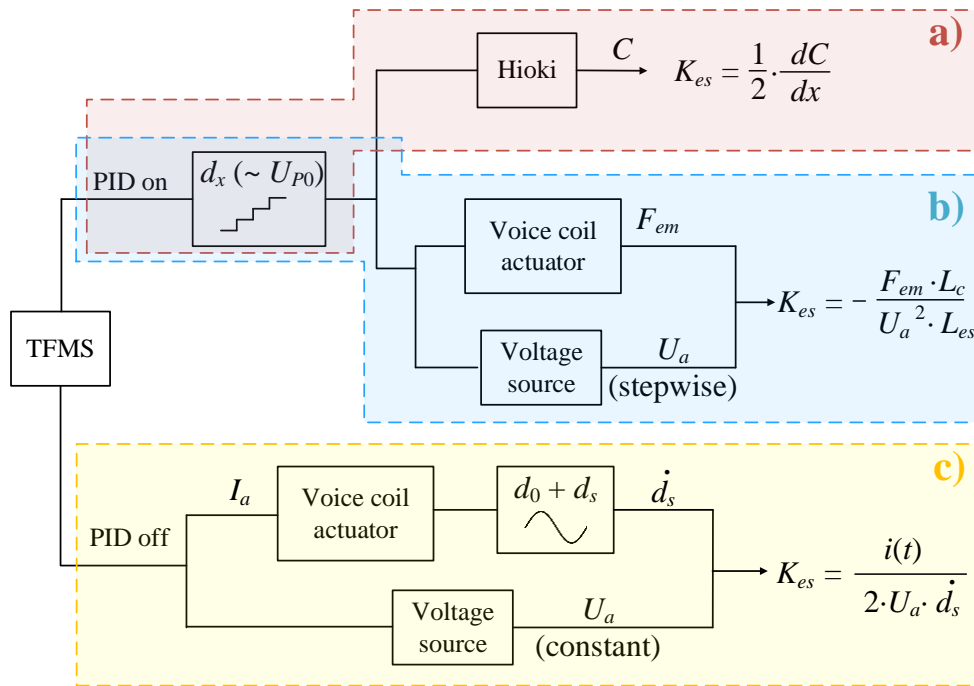


Figure 5.6: Determining the calibration factor with three methods: (a) Measuring capacitance values C with different distances d_x for obtaining capacitance gradient; (b) Recording the compensation force with different actuation voltage U_a across the two electrodes, in order to compare the electrostatic forces F_{es} with electromagnetic forces F_{em} ; (c) The PID-controller is shut down and the TFMS is set into a velocity mode, the calibration factor is determined by measuring the induced current $i(t)$.

5.3.1 Three methods to calibrate the electrostatic force

Method (a): By measuring the capacitance values with different distance values:

This method is based on the equation (5.2) and (5.3) as general equations to generate the electrostatic force, where the force calibration factor K_{es} is described by the capacitance gradient dC/dx as presented in equation (5.4). The capacitance of the capacitor is dependent on the distance between the two electrodes, namely the distance between the PCB and the dummy weight in x -direction. A is the effective cross section of the customized capacitor. Between the two electrodes is air under the room temperature, relative permittivity ε_r is 1.00053. d_0 is the initial distance between the two electrodes and d_s indicates the change of the distance in the x -direction.

$$K_{es} = \frac{1}{2} \cdot \frac{dC}{dx} = -\frac{1}{2} \cdot \frac{\varepsilon_0 \varepsilon_r A}{(d_0 + d_s)^2} \quad (5.4)$$

In several work [16,18], for calibration of the electrostatic force, the distance between the two electrodes is adjusted by driving one of the electrodes to different positions using a piezo stage or an auxiliary capacitor. In comparison, as the motion of the TFMS can be controlled in its closed-loop operation mode, the dummy weight as one electrode can be set to different positions by giving different defined values U_{p0} in the PID-controller. Thereby, the distance d_x between the dummy weight and the PCB as the summation of d_0 and d_s can be adjusted and controlled. The value of the distance can be calculated with equation (5.5).

$$\begin{aligned} d_x &= d_0 + d_s = (U_{p0} - U_P') \cdot K_{ps} \cdot L_{es} \\ d_0 &= (0 - U_P') \cdot K_{ps} \cdot L_{es} = -U_P' \cdot K_{ps} \cdot L_{es} \end{aligned} \quad (5.5)$$

U_{p0} is the value given to the PID-controller and defines the position to be maintained in the compensation procedure. By setting different values of U_{p0} , the value d_x as the distance between the two electrodes of the capacitor changes along with it. d_0 indicates the distance between the two electrodes when the value U_{p0} of zero is given. U_P' is the output voltage of the positioning sensor when the wheel is at the position where the dummy weight touches the PCB (namely, $d_x = 0$). The factor K_{ps} obtained in section 4.1 is the calibration factor to convert the voltage values into rotational angles and L_{es} illustrated in figure 5.5 is the distance of the customized capacitor away from the rotational axis of the TFMS. With the known values of U_P' , K_{ps} and L_{es} , the initial distance d_0 is determined as approximately 124 μm .

According to the rough calculation with the parameters of the customized capacitor, the capacitance value is in the range of dozens picofarad and can be measured by the device Hioki impedance analyzer IM-3570 [49]. In the experiment, stepwise voltage U_{p0} is given in the PID-controller in order to lead to different distance values d_x . The capacitance value C of the customized capacitor is measured by the impedance analyzer with each distance value as the block diagram (a) in figure 5.6 presents. In this

way the capacitance gradient is determined, which can be used to describe the calibration factor of the electrostatic force.

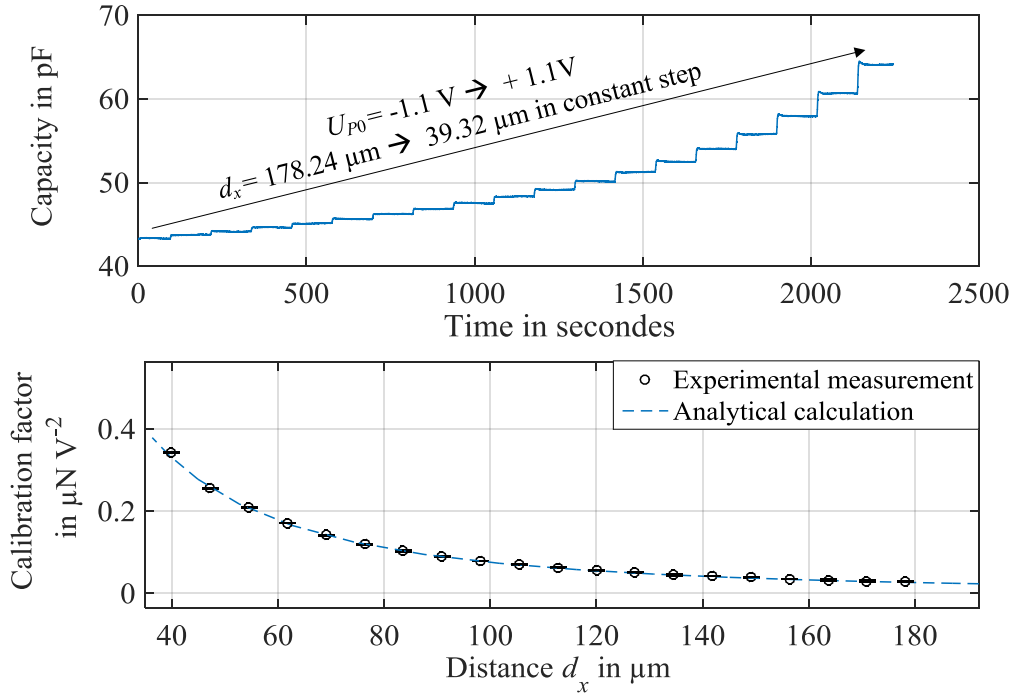


Figure 5.7: Top: Measured capacitance values of the customized capacitor by setting different distances between the two electrodes. Bottom: Determined calibration factor along with different distance values.

Top of figure 5.7 presents the measured capacitance values by setting different distances between the two electrodes. The capacitance value is inversely proportional to the distance d_x . Due to a same change in the separation, the closer the two electrodes are, the more rapidly the capacitance increases. The calibration factor K_{es} is demonstrated in the bottom figure, the values calculated theoretically with the parameters according to equation (5.4) as well as the experimental data are presented and show an agreement with each other. The calibration factor depends on the distance between the two electrodes, when $U_{p0} = 0 \text{ V}$, in other words, with the separation d_0 , the calibration factor is:

$$K_{es} = 0.0561 \pm 0.0006 \text{ } \mu\text{N V}^{-2} (k = 2)$$

Figure 5.7 reveals that the calibration factor can be further increased by reducing the distance between the PCB and the dummy weight. From 120 μm to 40 μm , the calibration factor is increased by 6 times. Moreover, indicated by equation (5.4), increasing the effective section area A of the capacitor or the relative permittivity is also a way to increase the calibration factor.

Method (b): By comparing with the electromagnetic force:

As a widely used calibration procedure in force metrology, the unknown forces are able to be compared with known force values given by normal and standards. The force constant of the voice coil actuator is calibrated with the standard mass piece of class E₂ using the deflection method. The electromagnetic force provided by it is traceable and can be thereby considered as the reference force. By applying the stepwise actuation voltage U_a across the two electrodes and simultaneously recording the required electromagnetic compensation forces F_{em} from the voice coil actuator, the calibration factor is determined experimentally using equation (5.6).

$$F_{es} = K_{es} \cdot U_a^2 = -F_{em} \cdot \frac{L_c}{L_{es}} \quad \text{therefore,} \quad K_{es} = -\frac{F_{em} \cdot L_c}{U_a^2 \cdot L_{es}} \quad (5.6)$$

L_c and L_{es} indicate the arm length of the electromagnetic force F_{em} and the electrostatic force F_{es} respectively. In this way, the electrostatic force can be calibrated with the help of electromagnetic force in the force mode as presented with the block diagram (b) in figure 5.6.

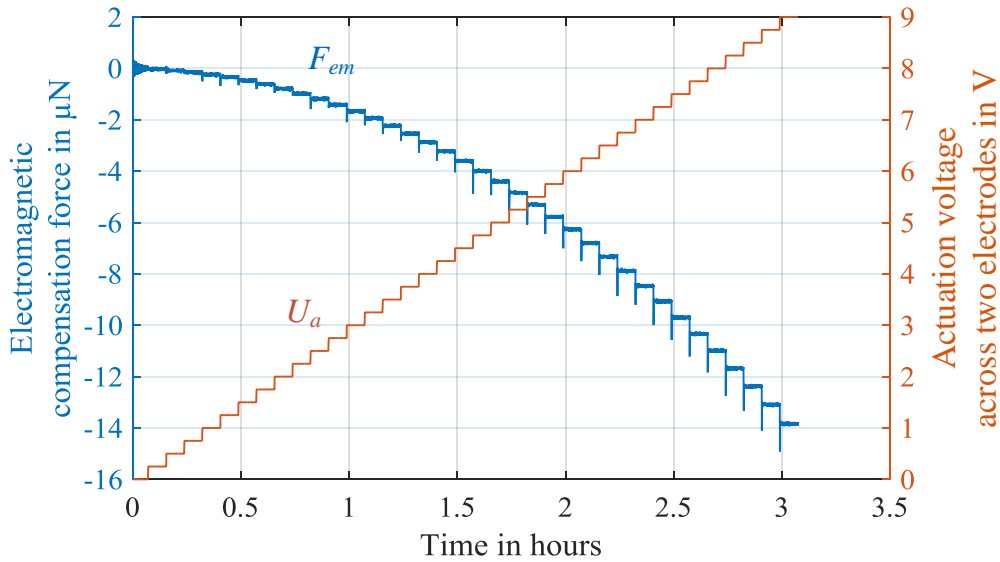


Figure 5.8: Stepwise actuation voltage across the capacitor to generate electrostatic force (right axis) and the required electromagnetic force to compensate it (left axis).

In figure 5.8, the measured data of one experiment with the distance d_0 ($U_{P0} = 0$) is demonstrated. The stepwise applied actuation voltage U_a leads to stepwise electrostatic forces F_{es} which are compensated by the electromagnetic force F_{em} . The quadratic relationship is between the actuation voltage and the force which agrees with equation (5.6). Second order polynomial fitting is applied on the measured data and with the consideration of the arm length L_{es} and L_c the calibration factor determined by method (b) is:

$$K_{es} = 0.0534 \pm 0.0022 \mu\text{N V}^{-2} \quad (k = 2)$$

The obtained calibration factor matches the one determined by method (a) well. Moreover, similar to that in method (a), the calibration procedure is implemented with different distances between the two electrodes by setting the different value of U_{P0} , which is presented later at the end of the section.

Method (c): By measuring induced current in a velocity mode:

In the watt balance experiment the force factor ($B \cdot L$) can be dynamically determined by operating the balance in a velocity mode and recording the induced voltage on the coil [50]. Similarly, the customized capacitor can be arranged in the velocity mode when the wheel is driven by the voice coil actuator moving relatively to the PCB plate (PID-controller is shut down). Due to the relative motion, the current $i(t)$ is induced and can be measured through a resistor. Constant actuation voltage U_a is applied across both electrodes of the capacitor, the induced current as the time-derivative of the charge Q is described as equation (5.7):

$$i(t) = \frac{dQ}{dt} = \frac{d(C \cdot U_a)}{dt} = C \cdot \frac{dU_a}{dt} + U_a \cdot \frac{dC}{dt} = U_a \cdot \frac{dC}{dt} = -\frac{U_a A \epsilon_0 \epsilon_r \dot{d}_s}{(d_0 + d_s)^2} \quad (5.7)$$

Where A indicates the section area of the capacitor, d_0 is the initial distance of the two plates in static status and d_s describes the motion of the wheel in dynamic case; \dot{d}_s presents the velocity of the motion. Based on equation (5.4) and (5.7) the force calibration factor K_{es} can be described as equation (5.8):

$$K_{es} = -\frac{1}{2} \frac{\epsilon_0 \epsilon_r A}{(d_0 + d_s)^2} = \frac{i(t)}{2 \cdot U_a \dot{d}_s} \quad (5.8)$$

The experimental procedure is demonstrated in figure 5.6 block diagram (c). Current source supplies sinusoidal actuation current I_a to the voice coil, leading the plane wheel of the TFMS into the sinusoidal motion. This motion is detected by the positioning sensor, by which the velocity of the dummy weight as one electrode of the capacitor is determined as the time-derivative of the position. Across the capacitor the constant voltage U_a of 5 V is supplied. Due to the slow response of the TFMS in its open-loop mode, high velocity motion is not achievable because the amplitude of the motion is strongly damped when the frequency is higher than the resonance frequency. The actuation current is set with the amplitude of 50 μ A and frequency of 0.06 Hz. The induced current is in the range of pico-ampere due to the low velocity and measured by measuring the voltage drop U_m upon a resistor R_r . In order to amplify the voltage, a resistor of 4 M Ω is connected to the capacitor. The multimeter with an inner resistor of 1 M Ω is connected to the resistor R_r in a parallel circuit to measure the voltage drop U_m . The effective resistor R_r' is thereby reduced from 4 M Ω to 0.8 M Ω .

Figure 5.9 demonstrates the measured and analytical results. Due to the sinusoidal actuation current, the TFMS is driven into the sinusoidal motion with the displacement and the velocity shown in the upper figure. With equation (5.7), the induced current $i(t)$ is determined theoretically with the value of

the parameters on the right side of the equation. The measured current matches the analytical result as presented in the bottom figure. The procedure is dynamic as one electrode of the capacitor moves continuously, leading to different K values of the calibration factor at different positions. Based on equation (5.8), the determined K_{es} calculated with the induced current, velocity and the constant voltage is presented in figure 5.10 corresponding to different position values, and at the position d_0 , the calibration factor is:

$$K_{es} = 0.0583 \pm 0.010 \mu\text{N V}^{-2} \quad (k = 2)$$

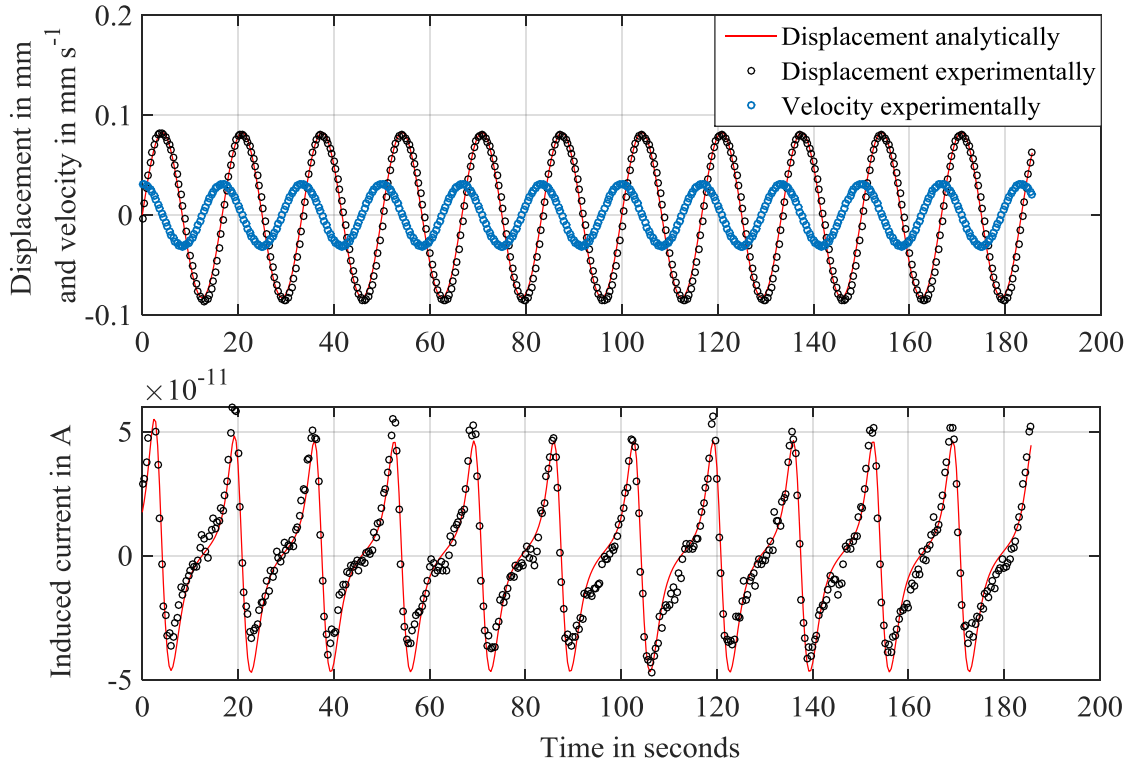


Figure 5.9: Top: Analytically calculated displacement of the dummy as one electrode according to the stiffness of the TFMS; experimentally measured displacement, and the velocity as the time-derivative of the displacement; Bottom: induced current: analytical calculation with equation (5.7) and values determined experimentally by measuring the voltage drop through a resistor.

5.3.2 Discussion and uncertainty budget

In the previous subsection, three methods are introduced to calibrate the electrostatic force. The agreement is presented in figure 5.10, the quality of each method differs from each other.

In the method (a), where the calibration is implemented by determining the capacitance gradient, the uncertainty of the calibration factor is determined by the measurement of the capacitance and the uncertainty of the distance. The capacitance value is taken as the mean value from repeated experiment while the distance is described by the voltage values of the positioning sensor, which is constant at a certain value in the range of $\pm 10 \mu\text{V}$, corresponding to the change in d_x of $< \pm 1 \text{ nm}$. The

uncertainty is presented in table 5.2. In this method, the result is determined dominantly by the repeatability in the measurement of the capacitance value.

Table 5.2: Uncertainty discussion of the calibration factor determined by three methods.

	Quantity	Value	Standard uncertainty	Distribution	Index
(a)	dC [pF]	1.64	0.009	Normal	100%
	dx [μm]	14.6	$0.577 \cdot 10^{-3}$	Rectangular	0%
Result: $K_{es} = 0.0561 \pm 0.0006 \mu\text{N V}^{-2}$ ($k = 2$)					
(b)	K_{vc} [N A^{-1}]	0.869	0.019	Normal	86.3%
	I_c [A]	$1.5 \cdot 10^{-5}$	$0.107 \cdot 10^{-6}$	Normal	9.0%
	L_c [mm]	59.5	0.289	Rectangular	4.2%
	U_a [V]	9	$4.08 \cdot 10^{-6}$	Triangular	0%
	L_{es} [mm]	180	0.289	Rectangular	0.5%
Result: $K_{es} = 0.0534 \pm 0.0025 \mu\text{N V}^{-2}$ ($k = 2$)					
(c)	U_m [μV]	14.4	1.3	Normal	100%
	R_r [$\text{M}\Omega$]	0.8	0.008	Rectangular	0%
	U_a [V]	5	$4.08 \cdot 10^{-6}$	Triangular	0%
	\dot{d}_s [mm s^{-1}]	0.0312	$0.61 \cdot 10^{-5}$	Normal	0%
Result: $K_{es} = 0.0583 \pm 0.0100 \mu\text{N V}^{-2}$ ($k = 2$)					

In the second method, where the electrostatic force is compared with the electromagnetic force, the uncertainty budget is presented in table 5.2 in the bases of the equation (5.6). The uncertainty in the force constant of the voice coil actuator contributes most to the measurement with the index of 86.3%. Using this method, there is a deviation from the analytical result, this could be resulted by the different values of the force constant K_{vc} as the immerse depth changes along with different separations.

When the TFMS operates in the velocity mode, the measurement is obtained by the measured voltage drop upon the resistor, namely, by the measured induced current. In comparison with the method (a) and (b), the calibration factor determined in the velocity mode shows a larger uncertainty and also larger deviation from the analytical calculation. The reason is that the velocity as well as the amplitude of the motion is limited by the dynamic behavior of the TFMS in its open-loop operation mode, therefore the low induced current in the range of pico ampere can be covered by noise as it is presented in figure 5.9. However, the agreement with the results achieved in method (a) and (b) shows the feasibility to calibrate the electrostatic force in such velocity mode. To overcome the problem caused by the slow response in the open-loop, instead of using the contactless electromagnetic force to actuate the TFMS into motion, in the calibration procedure the TFMS could be fixed with the

actuation device (for example, piezo stage), the motion with high frequency is thereby enabled and the induced current can be amplified.

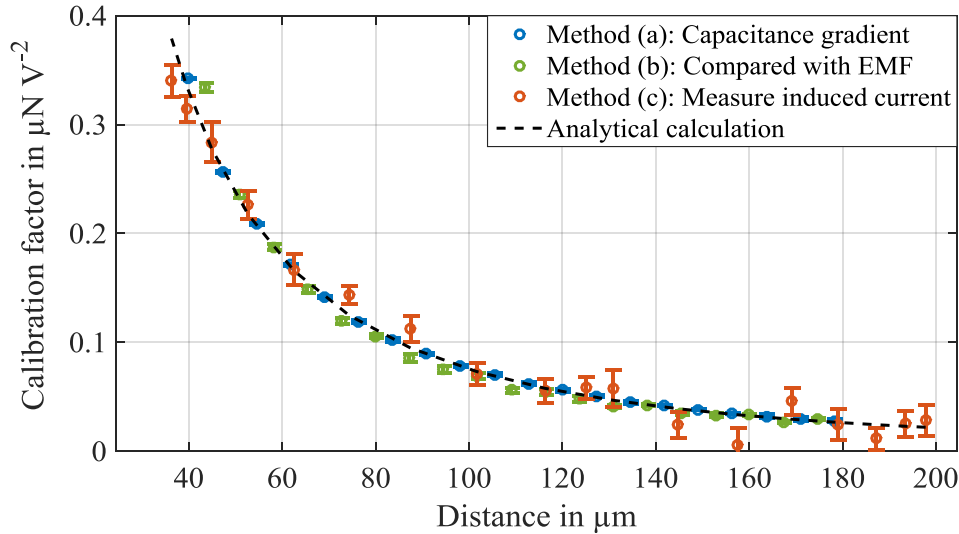


Figure 5.10: Calibration factor as the function of the distance between two electrodes of the capacitor, determined with three methods.

In comparison with the other two methods, the calibration factor determined by measuring the capacitance gradient is with the minimal deviation from the analytical calculation and also with a considerably lower relative uncertainty of 1 % ($k = 2$). The calibration factor K_{es} determined by the method (a) will be taken and used in the later measurement. Compared to the force constant K_{vc} of the commercial voice coil actuator with relative uncertainty of 4.4 % ($k = 2$), the electrostatic force provided by the customized capacitive actuator is a reasonable replacement of the electromagnetic force to perform actuation forces.

5.4 Test of the dynamic behavior

Using the simple configuration presented in figure 5.5, the electrostatic force between the two electrodes of the customized capacitor can be generated in the attractive direction. With the aim to set up the closed-loop operation mode using electrostatic force as the compensation force, a pre-voltage $U_{a0} = 5$ V is applied between the PCB and the TFMS to generate the electrostatic pre-force and drive the wheel to a pre-position which is treated as the null position. In this way, by increasing and decreasing the actuation voltage U_a , the wheel can be controlled by the electrostatic force around the null position. The calibration factor K_{es} is determined according to the figure 5.10 with the distance d_x when $U_a = 5$ V is applied.

The dynamic behavior of the TFMS is tested in this section in respect to its operation in open-loop, in closed-loop using the electromagnetic force and electrostatic force respectively. In section 4.3, the dynamic behavior is presented by the bode diagram plotted due to the transfer function, which is determined by step response. In this section, the dynamic behavior is tested with dynamic forces. Until now, both electromagnetic force and electrostatic force can function as actuation force as well as

compensation force. To test the dynamic behavior of the TFMS with electromagnetic force as the compensation force, the electrostatic forces with different loading frequencies generated by the customized capacitive actuator act as external actuation forces. In contrast, the electromagnetic forces are applied with different loading frequencies to the TFMS while being compensated by the electrostatic forces. In the test of operation in the open-loop, both forces can be used as external applied force, whereas the electromagnetic force is chosen. Based on the different dynamic behavior of the TFMS in open-loop and closed-loop, the range of the load frequency is set differently in each case. In the open-loop, the loading frequency from 0.001 Hz to 5 Hz are tested while in the closed-loop loading frequency up to 10 Hz is tested.

The solid lines in figure 5.11 indicate the analytically determined frequency response in each case. For open-loop, it is plotted by the transfer function $G(s)$ described in equation (4.12). In both cases of closed-loop, the transfer function $\Phi(s)$ is calculated from $G(s)$ in open-loop and the $H(s)$ of the PID-controller, revealed by equation (5.9) and (5.10) [51]. K_p , K_d and K_i are the parameters of the PID-controller which were experimentally determined for both cases.

$$H(s) = K_p + \frac{K_i}{s} + K_d \cdot s \quad (5.9)$$

$$\Phi(s) = \frac{G(s) \cdot H(s)}{1 + G(s) \cdot H(s)} \quad (5.10)$$

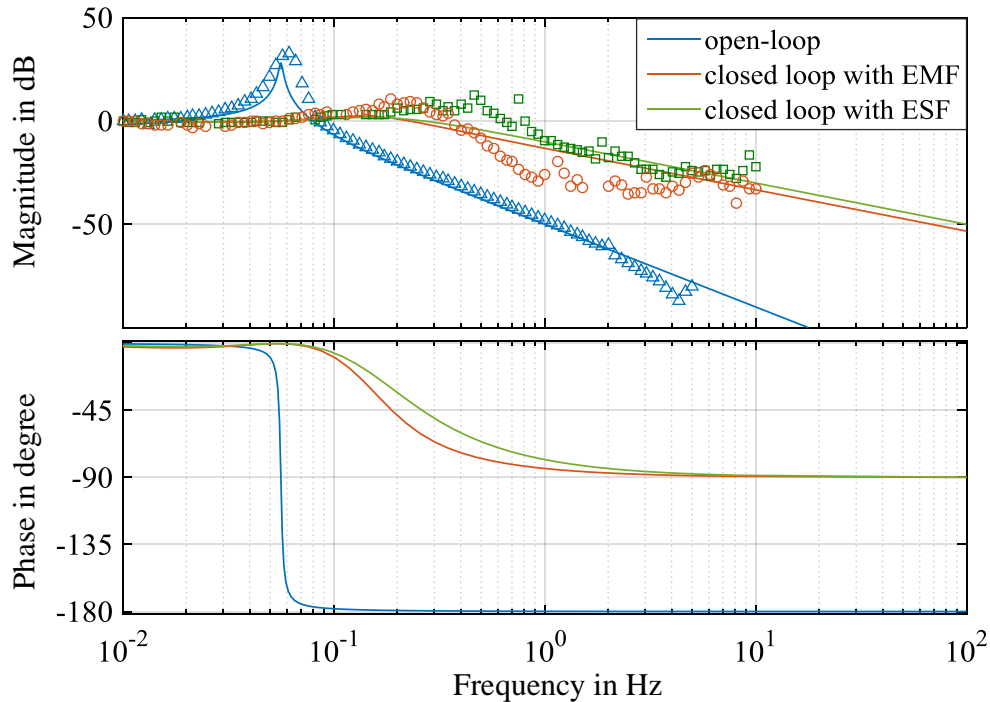


Figure 5.11: Frequency response of the TFMS in open-loop and closed-loop. Solid line: analytical calculation with transfer function; markers: experimentally determined by forces with different load frequencies.

The measured data presented in figure 5.11 shows agreement with the analytical calculation. After setting up the closed-loop operation mode, the cutoff frequency is improved to approximately 0.1 Hz, which is sufficient for the measurement in LFV application. Moreover, by using the customized capacitive actuator to generate electrostatic compensation force, the dynamic behavior of the system is similar to that using the commercial voice coil actuator to generate electromagnetic force.

5.5 Test of force resolution

In the current stage, the closed-loop operation mode is built and the dynamic behavior of the TFMS is thereby improved. Additionally, the commercial voice coil actuator and customized capacitive actuator are assembled to the TFMS, providing both possibilities to generate electromagnetic force and electrostatic force. With such an option, smaller magnitude forces are applied and measured by the TFMS to test the force resolution in the closed-loop operation mode. The general measurement schematic is illustrated in figure 5.2. In this set of measurements, different values of actuation voltage U_a are supplied to the customized capacitor. The electrostatic forces as external actuation forces are applied on the TFMS; and the electromagnetic force is involved as the compensation force which compensates the external electrostatic force to maintain the plane wheel at its defined null position.

For the measurement of weak forces in micro and nanonewton range, the consideration of the influences such as the thermal and seismic drift and noises from the environment should be assumed carefully. In several researches, differential force measurement setups were developed, with one system measuring target signal which is distorted by noises, and an additional identical reference system measuring such noises [26, 30]. However, without considering changes in mechanical structure or other additions in our work, an alternative approach can be applied in the data evaluation.

The ABA (or ABBA) measurement sequence is a commonly known method used in the mass and force metrology. The measurement is carried out in the process of measuring weight A, then weight B, then again weight A (or unloaded (A) - loaded (B) - unloaded (A)). Each measurement of weight A or B lasts an equal time period. The linear drift can be then eliminated by fitting with the measured values in the ABA procedure (details in [52]). In this case, the related data evaluation has a positive effect to cancel out the linear drift. However, in many situations, the drift is non-linear and by running the ABA (or ABBA) sequence measurements, the errors can still remain in the measured signal. In case of the apparatus presented in our work, another alternative known as the newton's polynomial interpolation (NPI) is used for estimation of the non-linear drift [53, 54].

Equation (5.11) describes the calculation method of the NPI: with a set of given data points $(x_0, y_0), (x_1, y_1), \dots, (x_j, y_j), \dots, (x_k, y_k)$, the non-linear polynomial fitting can be estimated in order to determine the ungiven values $N(x)$ on the fitting. In the force measurement, the x_j indicate the time points during the measurement procedure, while y_j are the drift values. By using equation (5.11), each ungiven points on the non-linear drift $y = N(x)$ can be estimated.

$$N(x) = y_0 + f(y_0, y_1)(x - x_0) + f(y_0, \dots, y_k)(x - x_0) \dots (x - x_{k-1}) \quad (5.11)$$

- During the measurement period without external load/forces, the output signal of the TFMS F_{out1} indicates the drift/noise F_{D1} , which can be considered as the given values on the non-linear polynomial fitting, as equation (5.12) shows:

$$F_{out1} = F_{D1} \quad (5.12)$$

- During the loading period with external force F_{es} acting on the TFMS, the output signal of the TFMS F_{out2} is a summation of the drift signal F_{D2} and the target force signal F_{es} as equation (5.13) describes:

$$F_{out2} = F_{D2} + F_{es} \quad (5.13)$$

At these time points, the drift values F_{D2} can be considered as ungiven values on the polynomial fitting curve, but are possible to be determined by NPI with the measured data F_{D1} in step 1 as known data.

- Thus, the subtraction between the measured signal F_{out2} and the determined drift signal F_{D2} is the target force value. In this way, without using the differential force measurement system, the non-linear drift can also be estimated and corrected by using such data evaluation.

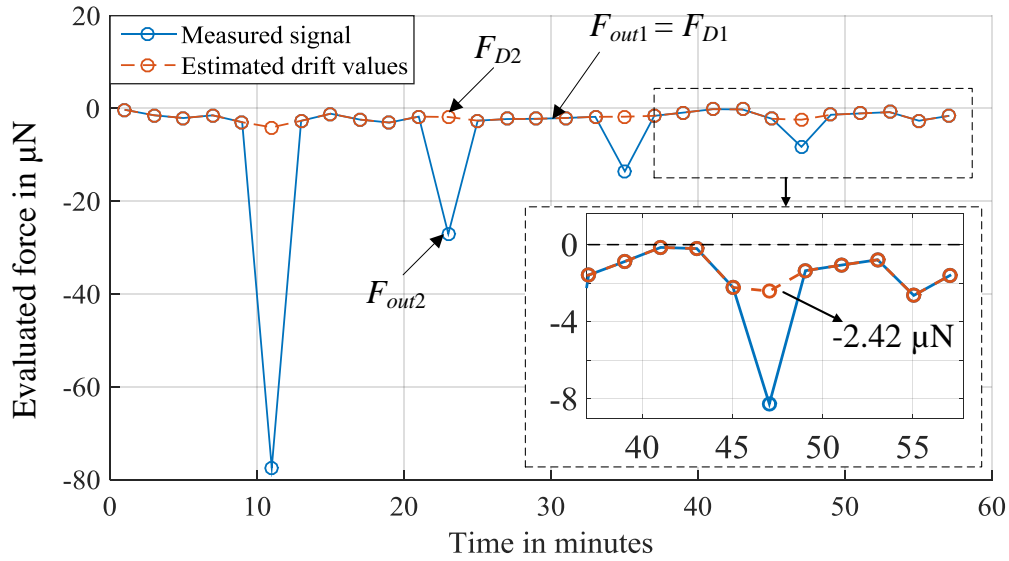


Figure 5.12: Estimation of the drift using the NPI. Blue solid: measured signal from TFMS (summation of external force and drift); red dashed: estimated drift using the NPI.

The more given data points used in the NPI, the more accurate unknown drift values can be estimated. As it is presented in figure 5.12, in approximately 1 hour time period, electrostatic force is applied on the TFMS four times with different magnitudes. Each loading period lasts for 2 minutes. Before and after each loading, there is a period of 10 minutes with no external force, in other words, during the time period before and after loading, the drift values are continuously recorded. The mean value of the output signal in each time interval of 2 minutes is calculated. Using the NPI described in equation (5.11), the drift values when forces are applied can be estimated as figure 5.12 shows. As mentioned

above, the subtraction of the measured output signal F_{out2} and the estimated drift values F_{D2} indicate the external electrostatic force. As the insert figure shows, without such data evaluation, the force is distorted by the drift value of $2.42 \mu\text{N}$, approximately 30% of the measured signal, which proves that the necessity of using NPI.

By applying the NPI in the data evaluation, the minimally resolved force is tested on the TFMS. A set of actuation voltage values $U_a = [0.5 \ 0.2 \ 0.1 \ 0.05 \ 0.04 \ 0.03 \ 0.02 \ 0.01] \text{ V}$ are applied across the two electrodes of the capacitor. The electrostatic forces with the related magnitudes can be generated on the TFMS and measured by electromagnetic compensation force. The magnitude of the electrostatic forces can be calculated with the calibration factor K_{es} determined with the corresponded distance. The applied forces and the measured force values are compared with each other, measurement results are presented in figure 5.13 and table 5.3.

Table 5.3: Comparison of the applied force values and measured force values.

U_a [V]	Applied force [nN]	Measured force [nN]		Difference [nN]
		Value	Uncertainty ($k = 2$)	
0.5	77.1	77.5	0.6	0.4
0.2	26.3	26.2	0.9	-0.1
0.1	12.2	12.0	0.4	-0.2
0.05	5.9	6.0	0.5	0.1
0.04	4.7	4.7	0.5	0
0.03	3.5	3.7	0.5	0.2
0.02	2.3	2.5	0.6	0.2
0.01	1.2	1.6	0.6	0.4

The differences between the applied force values and the experimentally measured force values are within the range of $\pm 1 \text{ nN}$, which presents agreement with each other. The uncertainties of the experimentally measured forces are determined by measured data from repeated measurements ($k = 2$). Further tests with even lower applied electrostatic forces are carried out. However, the forces weaker than 1.6 nN are difficult to be distinguished. In comparison with the theoretically calculated force resolution of 0.55 nN (obtained with experimentally determined spring constant in section 4.2.2 instead of the value given by the manufacturer), the forces obtained experimentally are limited by the influences originating from the surroundings that are typical in real laboratory conditions. After setting up the closed-loop operation mode, the resolution of the TFMS is 2 nN by using the NPI in data evaluation. The expanded uncertainties ($k = 2$) of the tested forces are also within $\pm 1 \text{ nN}$, which is acceptable since it does not exceed the force resolution. With a maximum applied voltage $U_a = 8 \text{ V}$ in this work, an electrostatic force of approximately of $6 \mu\text{N}$ is applied to the TFMS; this means the

measurement range of the system can be described as $\pm 3 \mu\text{N}$. As introduced in section 5.3, the measuring range can be further extended by increasing calibration factor K_{es} , which can be achieved by reducing the distance between the two electrodes, increasing the permittivity, or changing other geometrical parameters of the customized capacitor.

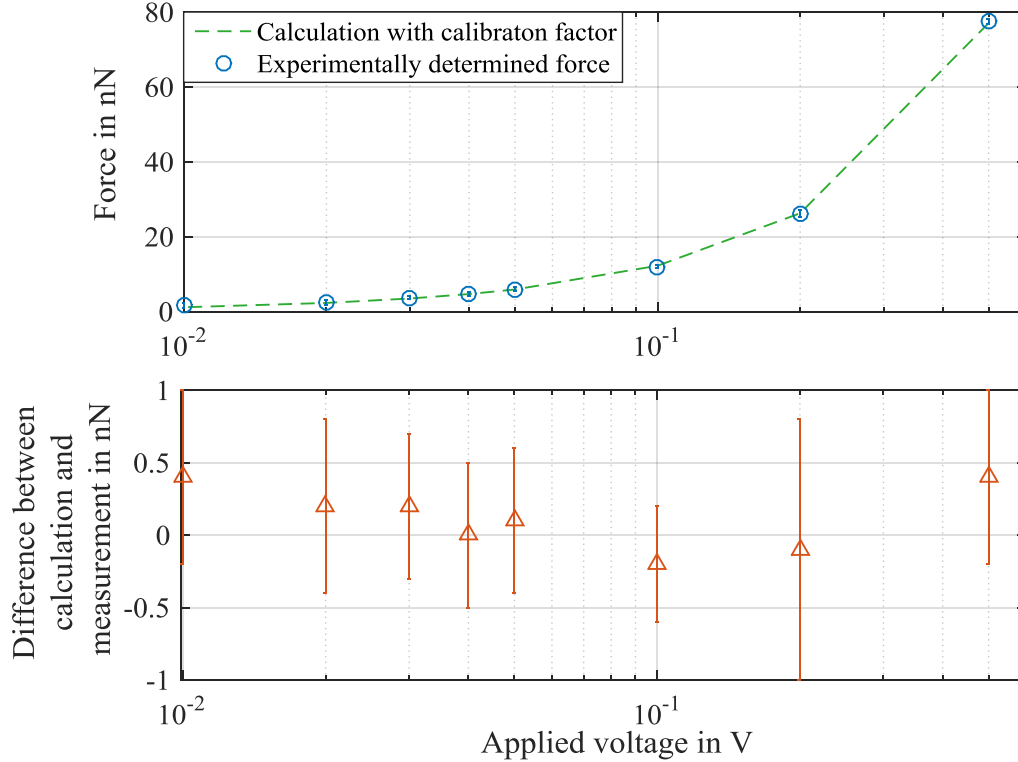


Figure 5.13: Comparison of the applied electrostatic forces and the measured force. Green dash line: Applied electrostatic force (values are calculated using the calibration factor K_{es}); blue circle markers: measured electrostatic force using the TFMS and the newton's polynomial interpolation in the data evaluation; red triangular markers: difference between the applied forces and the measured forces.

5.6 Summary

In this chapter, the closed-loop operation mode was set up based on the PID-controller. In the closed-loop operation mode, the plane wheel of the TFMS is continuously maintained at the custom-defined null position by the compensation force. Initially, the compensation force was the electromagnetic force provided by a commercial voice coil actuator. For the local alignment, the force constant of the voice coil actuator is determined using the deflection method as $K_{vc} = 0.869 \text{ N A}^{-1}$ with the relative uncertainty of 4.4 % ($k = 2$), which differs from the value given by the manufacturer because of the immersion depth and errors in alignment. Then, a customized capacitive actuator was introduced to generate electrostatic force as an alternative to provide compensation/actuation force to the TFMS. By assembling a PCB plate connected to the anode of the voltage source, and taking the whole TFMS as one conductor connected to the cathode of the voltage source, a customized capacitive force actuator

was built as described in section 5.2. The value of the generated electrostatic force is obtained by the actuation voltage applied across the two electrodes and the electrostatic force calibration factor K_{es} . In section 5.3, three methods were presented to determine the calibration factor, they are: (a) by measuring capacitance with different distances to obtain capacitance gradient; (b) by comparing the electrostatic force with the electromagnetic force as the reference force; (c) by measuring the induced current when the capacitor is set into a velocity mode. The calibration factors determined using the three methods show agreement with each other. In comparison with method (b) and (c), by measuring the capacitance gradient, the determined calibration factor matches the analytical result with the minimal deviation and a considerably low uncertainty of 1 % ($k = 2$). Moreover, the relationship between the calibration factor and the distance between the two electrodes of the capacitor was also presented. The calibration factor can be further increased by modifying the geometrical parameters. In section 5.4 the dynamic behavior of the TFMS in its open-loop operation mode, closed-loop operation mode with electromagnetic force as well as electrostatic force as the compensation force were tested respectively. Sinusoidal actuation signals with different load frequencies as the input were applied to the TFMS. The response in each case was recorded and the bode diagram presented that by setting up the closed-loop operation mode, the cutoff frequency of the system has been improved to 0.1 Hz with the settling time of approximately 9.2 s. Additionally, the customized capacitive actuator functions as well as the commercial voice coil actuator in the compensating procedure. It is revealed that the electrostatic force is a reasonable replacement of the electromagnetic force with the following improvements:

- (1) More suitable for the LFV application where magnet system is involved;
- (2) No power wires connected to the rotational part of the TFMS;
- (3) Force constant K_{es} with lower relative uncertainty.
- (4) Force constant K_{es} can be adjusted by changing the geometry of the capacitor.

Finally in this chapter, the minimally resolved force with TFMS was tested. The newton's polynomial interpolation was used in the data evaluation to estimate the undesired drifts and noises. In this way, the influence caused by surroundings can be compensated without assembling second additional reference system. Considering theoretically calculated force resolution of 0.55 nN is limited by the influences from the surroundings that are typical in real laboratory conditions, the achieved force resolution of 2 nN is acceptable and the aim to improve the force resolution by one order of magnitude as introduced in the chapter 1 is reached.

Another improvement considered to be made in the future is setting up the differential electrostatic force actuator with two identical PCB plates presented in figure 5.14. With such configuration, two capacitors C_1 and C_2 enable the electrostatic force perform in both directions. The pre-voltage is thereby no more necessary and the measurement range can be extended.

The two PCBs are with identical geometry and assembled symmetrically at both sides of the copper dummy, which indicates that the capacitance gradient of the both capacitors are equal in magnitude and opposite in direction at the equilibrium position ($d_s = 0$).

$$\frac{dC_1}{dx} = -\frac{dC_2}{dx} \quad (5.14)$$

When the copper dummy as the middle electrode is biased at the voltage U_b , and the actuation voltage U_a and $-U_a$ is applied to PCB 1 and PCB 2 respectively, the electrostatic force is then determined based on equation (5.15) [55].

$$F_{es} = \frac{1}{2} \cdot \frac{dC_1}{dx} \cdot [(U_a - U_b)^2 - (-U_a - U_b)^2] = 2 \cdot \frac{dC_1}{dx} \cdot U_a \cdot U_b \quad (5.15)$$

In this way, the characteristic curve between the electrostatic force F_{es} and the actuation voltage U_a is thereby further improved as linear.

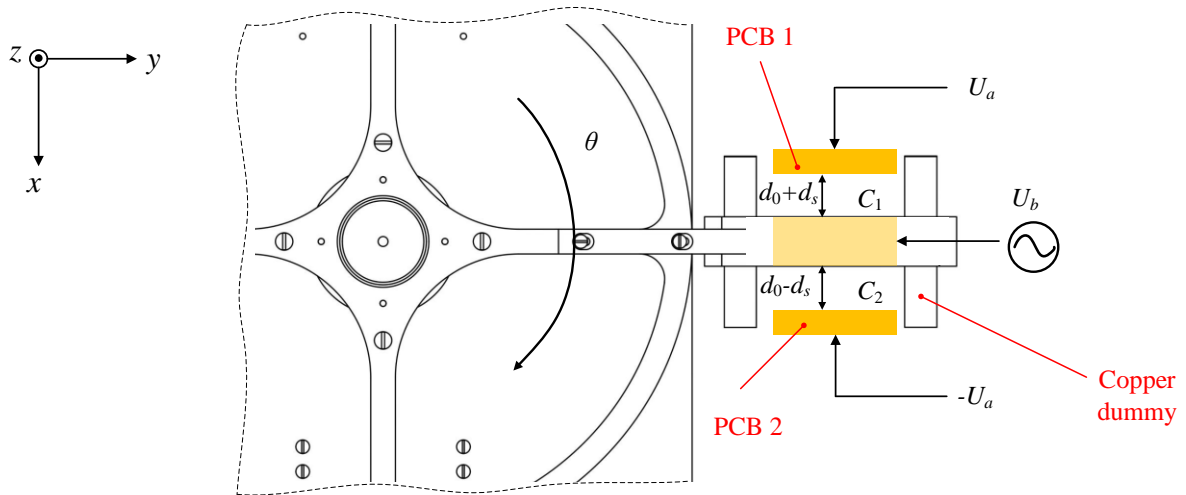


Figure 5.14: Schematic of electrostatic force actuator in differential configuration (top view), which is introduced as an improvement in the future.

6. Lorentz force measurement

In this Chapter, the measurements are implemented using the TFMS to measure Lorentz forces. The TFMS operates in the closed-loop operation mode with the electrostatic force compensating external forces. One of the two non-magnetic dummies is replaced by the magnet system providing the magnetic field. The experimental facility is built for implementing semi-dry calibration in section 6.1. In section 6.2, the experiments are presented, salt water as a mixture of tap water and salt (sodium chloride) is chosen as the electrolyte. Using the semi-dry calibration, the measuring sensitivity of the flowmeter based on the TFMS is obtained for different conductivity values.

6.1 Experimental facility

As introduced in section 1.1, the reaction force of the Lorentz force F_L' acting upon the magnet system is proportional to the flow velocity v and the electrical conductivity σ . By measuring the horizontally directed force F_L' , the TFMS carrying the magnet system can measure the velocity as a flowmeter or measure the conductivity as a conductivity meter after it is calibrated with known values. Intending to test the performance of the TFMS for measuring F_L' , practical measurements with magnet system together with electrolytes are implemented.

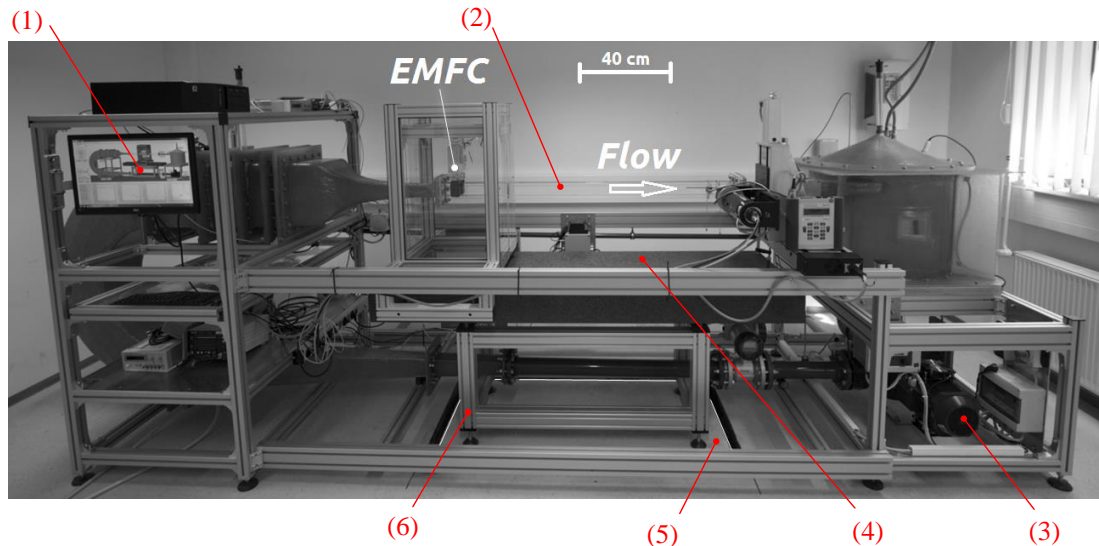


Figure 6.1: Photograph showing the LFV experimental facility in previous researches: EMFC as force measurement system and the channel-loop. (1) Control PC; (2) Channel; (3) Pump; (4) Granit-stone; (5) Decouple block of basement; (6) Main support frame of LFV [56].

Figure 6.1 presents the experimental facility used in previous researches in the framework of LFV. The flow channel was developed during the dissertation of André Wegfraß [56]. The fluid is pumped to flow in the channel by a pump (3), the flow velocity is dependent on the rotational speed of the pump and the maximally achieved flow velocity with it is approximately 3 m s^{-1} . Although the EMFC as the FMS is supported by the frame (6) located on the decouple block of basement (5), it was revealed in [27] that during the Lorentz force measurement on this channel-loop, vibration generated by the pump influenced the measurement result negatively. Without using the pump, the flow is generated utilizing the hydrostatic pressure in [27] to reduce the vibration. The uncertainty of the measured force is thereby reduced.

In this work, also without using the pump, an experimental facility with a tube is set up to simulate the flow channel. With the experimental facility presented in figure 6.2, the TFMS is calibrated for velocity measurement using the so-called semi-dry calibration.

To implement practical measurement, one of the two dummies in figure 3.1(b) is replaced by the magnet system, which was earlier designed in [10]. The magnet system is made of several permanent magnets arranged in a so-called Halbach-array structure shown in the snap shot in figure 6.2. On each side are five single permanent magnets arranged in the Halbach-array and both sides are combined with a bracket as mechanical connection, with which the magnet system is able to be assembled to the TFMS. The mass of the magnet system is 1.008 kg with the dimensions $a = 56 \text{ mm}$, $b = 46 \text{ mm}$ and $l = 90 \text{ mm}$ [10]. Compared to the conventional magnet system with similar dimension and mass, the magnet system arranged in Halbach-array can lead to approximately three times larger Lorentz force [27].

After replacing one dummy by the magnet system, the COG of the rotational part of the TFMS is displaced due to the change in geometry during reassembling, namely L_{T2} in figure 3.1 is extended or shortened. Moreover, the mass of the magnet system is not perfectly equal to the replaced dummy, which also leads to the necessity to adjust COG of the TFMS. Without moving and lifting the whole system on the tilt stage again, the tilt sensitivity as a concrete outcome of the displacement of COG is tested by tilting the work plane of the TFMS using the three adjustable feet ((9) in figure 3.1). Each of the three feet is a fine screw with length of 50.8 mm and pitch of 0.25 mm [57]. According to the geometrical parameters shown in appendix B, using the fine adjustable feet is able to generate the tilt angles around x with the resolution of 1.32 mrad (corresponding to a full turn of the fine screw) in the range of $\pm 267 \text{ mrad}$ and around y the tilt angles in the range of $\pm 154 \text{ mrad}$ can be realized with the resolution of 0.76 mrad. Similar as the adjustment procedure for minimizing the tilt sensitivity introduced in section 4.2.1, the tilt angle of the TFMS is manually adjusted using the adjustable feet while the output of the TFMS is recorded. Aluminum compensation weights are applied on the plane wheel to compensate the shift of COG until the monitored tilt sensitivity is within the required range.

Since the application conditions of the Lorentz force flow meter for high-temperature liquid metal alloys are difficult to be reproduced in the laboratory environment, the method of dry calibration was introduced in [56] and [58], where metal bars move through the magnet system with an adjustable speed as a simulation of the liquid metal flows. An advantage of the dry calibration is that the velocity can be accurately controlled without the effects of the velocity fluctuations. Differs from the cases in [56] and [58] where the liquid metal with high conductivity in the range of 10^4 to 10^6 S m^{-1} is mainly

6. Lorentz force measurement

investigated, in our work the weakly conducting electrolytes are expected to be studied. This is realizable by replacing the metal bars by a tube filled with electrolytes with different conductivities and implementing the semi-dry calibration. In comparison with the channel presented in figure 6.1, the experimental facility demonstrated in figure 6.2 enables the measurements with lower vibrations as well as lower thermal and magnetic influences.

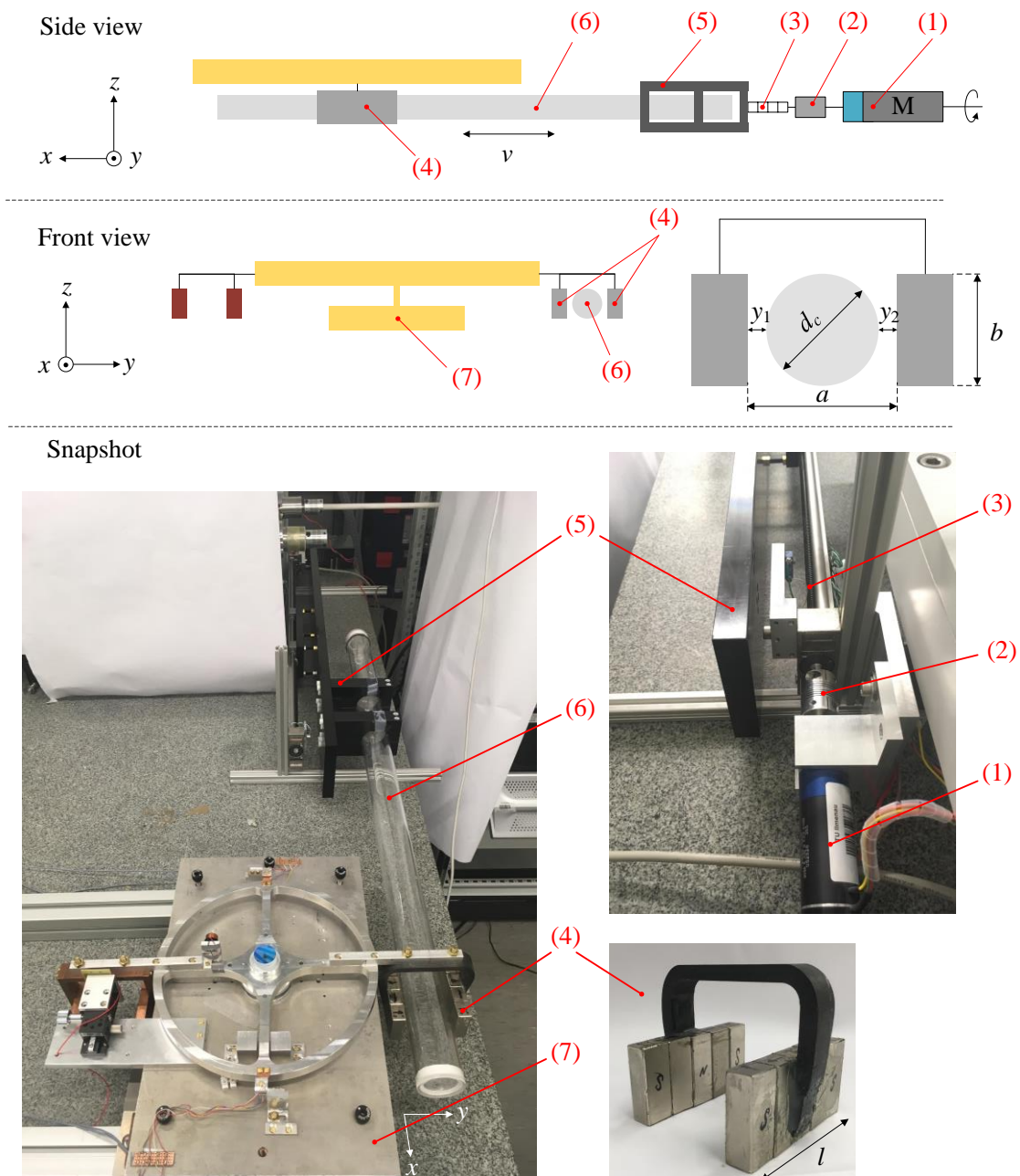


Figure 6.2: Experimental facility built up in this work to simulate LFV application and to implement semi-dry calibration: TFMS assembled with magnet system located on the tube, side view, front view and snap shot. (1) DC-servomotor; (2) Axis coupling; (3) Threaded shaft; (4) Magnet system arranged in Halbach-array; (5) Support of the tube; (6) Plexiglass tube for filling electrolytes; (7) TFMS.

A commercial plexiglass tube (6) with 1000 mm length, inner diameter of 46 mm and outer diameter $d = 50$ mm, is situated symmetrically within the magnet system with $y_1 = y_2 = 3$ mm. The tube is connected by the support (5) to a threaded shaft (3) which is driven by the DC-motor (1) [59]. As the DC-motor operates, the rotation motion is transferred into the linear motion by the threaded shaft. The tube, together with liquid inside, moves through the magnetic field simulating the flow in the channel. The support is manufactured from polyamide and screws and nuts used for connections are made of brass and aluminum as non-magnetic materials for minimizing the influences caused by magnetic interaction. Because the metal shaft and screws are also electrically conductive, which could lead to Lorentz force during the movement, the test channel is so assembled and located, that the screws, threaded shaft and DC-motor are far from the TFMS.

The speed of the tube is controllable by giving parameters to the DC-motor. The salt water as a mixture of tap water and sodium chloride is chosen as the electrolyte in the channel for experimental convenience. The conductivity is also adjustable by adjusting the concentration of the salt water. This experimental facility is flexible to provide the various values of conductivity and velocity, and is able to contribute into the so-called semi-dry calibration to determine the measuring sensitivity of the TFMS as a Lorentz force flowmeter.

6.2 Semi-dry calibration of the TFMS

Practical measurements with electrolytes are implemented using the experimental facility presented in figure 6.2. Limited by the specification of the DC-motor and the pitch of the threaded shaft, the speed of the tube is up to 3.3 mm s^{-1} available. The TFMS operates in the closed-loop operation mode with electrostatic force as the compensation force. Reference measurements are initially implemented without liquid inside the tube, signal from the TFMS is recorded with moveable empty tube as the 'dry part' of the semi-dry calibration to determine the noises caused by the experimental facility. Then, the same experimental procedures are carried out with the same tube filled with electrolytes. The semi-dry calibration indicates that instead of pumping the liquid running in the channel-loop, the calibration procedure is performed with the tube and the liquid inside moving together using the moving mechanism.

Different electrolytes are made with salt dissolved into the tap water to achieve different concentration presented in table 6.1. The conductivity of the empty tube is described by the conductivity of air, while the conductivity of the tap water is measured by the conductivity meter. According to the conductivity ordering guide [60], the conductivity of the salt water can be calculated from its concentration. The uncertainties given in the value of conductivity are due to a maximum permissible deviation of ± 100 mg in the weight of the dissolved salt, which could be caused during weighing process and dissolving process. Velocity values are adjusted as $v = 1.2, 2.6$ and 3.3 mm s^{-1} by sending different values to the controller of the motor. As introduced in the section 5.5, the NPI is applied during the data evaluation. Therefore, in order to estimate the drift signals, before and after each velocity level is the period of standstill, namely $v = 0$. Considering the settling time of the TFMS in its closed-loop operation mode and the settling time of the DC-motor, each step with the non-zero velocity lasts 30 seconds. As presented in the figure 6.3(a), before and after the motion is 300 seconds motionless period. The movement of the tube processes forth and back alternatively with positive and negative

velocity values, the maximum distance of the movement is thereby 99 mm (30 seconds with velocity of 3.3 mm s^{-1}), which is within the stroke of the shaft, and the required space of the experimental facility is thereby reduced.

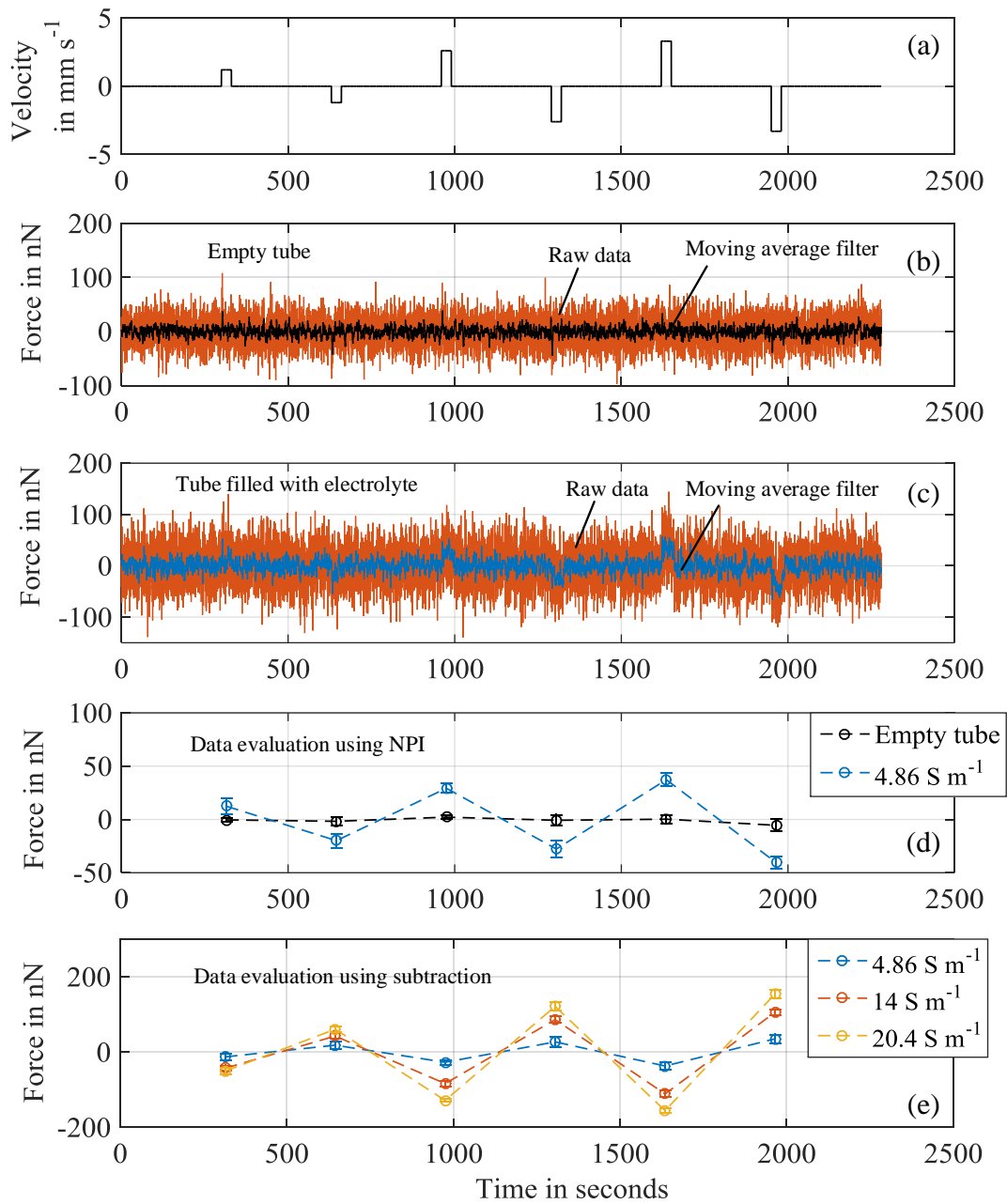


Figure 6.3: Overview of the measured force using the semi-dry calibration. (a) Moving velocity of the tube; (b) Recorded force values during measurement with the empty tube; (c) Recorded force values during measurement with tube filled with electrolyte (conductivity is 4.86 S m^{-1}); (d) Determined force values using the newton's polynomial interpolation; (e) Difference between the force signal with and without electrolyte.

When no electrolyte is inside, during the motion of the empty tube, recorded force signal is presented in figure 6.3 (b). In the raw data, noise is in the range of ± 100 nN which could be caused by the mechanical noises such as vibration of the tube. To enable the movement of the tube, the TFMS is no more located in the closed cover but exposed partially to the surroundings where airflow could also influence the measurements and increase the noise. However, in the real practical conditions where the TFMS is enclosed on the flow channel, this problem could be overcome. With the same procedure, the force values determined with the electrolyte with conductivity of 4.86 S m^{-1} in the tube are illustrated in the figure 6.3(c). After the data evaluation with the NPI, the force values determined during motion of the empty tube as well as the tube with the electrolyte inside are presented in the figure 6.3(d). In the further data evaluation, the Lorentz force generated by the moving electrolytes is determined by subtracting the force signal captured during measurements with empty tube, the results are illustrated in the figure 6.3(e).

Table 6.1: Conductivity values of the electrolytes used in the practical measurements; and the experimentally obtained measuring sensitivity.

Electrolyte	Conductivity [S m^{-1}]	Obtained sensitivity [nN s mm^{-1}]
Empty tube	$3 \cdot 10^{-15} \sim 8 \cdot 10^{-15}$	-
Tap water	0.026	0.0611
sodium chloride 30 g/L	4.86 ± 0.015	$11.63 \pm 2.88 (k = 2)$
sodium chloride 100 g/L	14 ± 0.012	$33.77 \pm 2.4 (k = 2)$
sodium chloride 167 g/L	20.4 ± 0.007	$48.06 \pm 3.1 (k = 2)$

The same data evaluation is implemented with all the measured data in respect to the electrolytes with different conductivities. In figure 6.4, the measured force values are presented in accordance with the velocity values for different electrolytes. As motioned above, with the channel presented in figure 6.1, the flow velocity of approximately of 3 m s^{-1} is achievable by using the pump. The available motion speed of the tube in our work is limited by 3.3 mm s^{-1} , which is approximately three orders of magnitude lower. Based on the equation (1.1), the induced Lorentz force is thereby also three orders of magnitude lower when the electrical conductivity remains as the same. Therefore, the relationship between the velocity and the induced force by the tap water with electrical conductivity of 0.026 S m^{-1} is difficult to identify. However, in the measurements on electrolytes with conductivity of 4.86 S m^{-1} , 14 S m^{-1} and 20.4 S m^{-1} , a good linearity can be observed. The linear fitting describing the sensitivity S_T of the TFMS as a flowmeter is applied on the measured data. The slopes of the linear fitting are presented in the figure 6.5 and table 6.1, giving the sensitivity of the velocity measurement for different conducting electrolytes. The sensitivity of the tap water is obtained on the linear fitting as $S_T|_{\text{Tap water}} = 0.0611 \text{ nN s mm}^{-1}$; with the velocity increased to 1 m s^{-1} , the corresponded force of

61.1 nN is expected to be measured. The uncertainties in the obtained sensitivities shown in figure 6.5 are from the repeatability of the force measurements. In the datasheet of the DC motor no uncertainty is given for its rotational speed, moreover, the uncertainty of the pitch of the shaft is also unknown. Therefore, the uncertainty of the velocity is assumed here with a relative uncertainty of 5 %. The uncertainty in the obtained sensitivity of the TFMS for measuring velocity is determined with the equation (6.1) and (6.2).

$$S_T = \frac{dF_L}{dv} \quad (6.1)$$

$$u_{S_T} = \sqrt{\left(\frac{\partial S_T}{\partial F_L} \cdot u_{F_L}\right)^2 + \left(\frac{\partial S_T}{\partial v} \cdot u_v\right)^2} \quad (6.2)$$

In this measurement, the uncertainty in the obtained sensitivity S_T is up to 24%, which is mainly contributed by the measured force values. As mentioned before, in order to enable the movement of the tube, the TFMS is difficult to be isolated from the surroundings, where influence of the airflow as well as the vibration of mechanical structure is unavoidable, and the measurement uncertainty is thereby increased. Another cause could be in the data evaluation using the NPI, where the estimated drift value could be deviated from the real value. To reduce this deviation, more given data should be used to calculate the polynomial fitting.

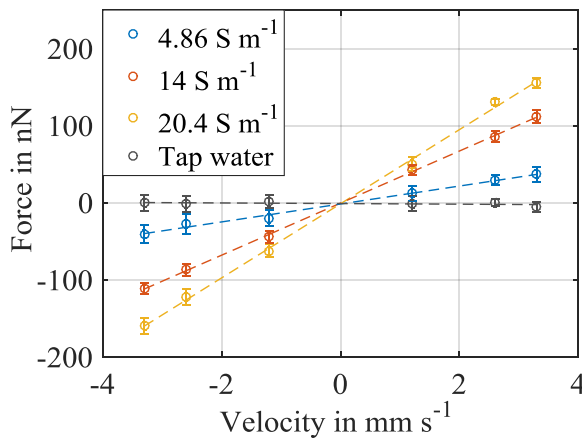


Figure 6.4: Determined force values in accordance with the velocity values for different conductivities.

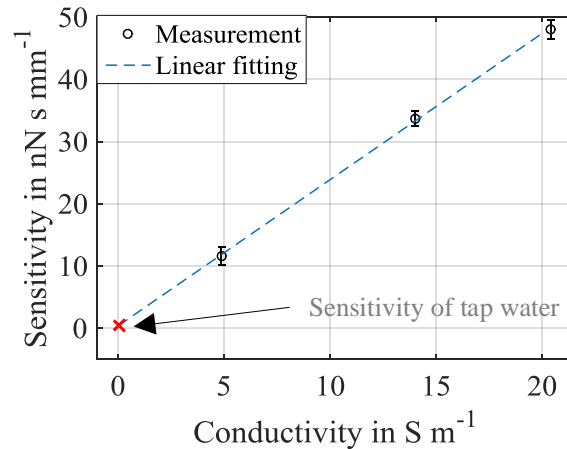


Figure 6.5: Sensitivity of the TFMS working as flowmeter in accordance with different conductivity values.

In comparison with the results achieved in work [29], with the same velocity and conductivity, the induced Lorentz force in our work is approximately 40% lower. The reason is that in this work a cylindrical tube with inner diameter of 46 mm is used, while in [29] the channel presented in figure 6.1 is rectangular with the inner section of 50 mm x 50 mm. The larger cross section leads to the larger volumetric flow rate and Lorentz force is thereby with higher magnitude. Moreover, the magnetic flux

density of the magnet system is inhomogeneous in the y -direction, which also leads to the difference in the induced Lorentz force when the shape of the channel is different. From both figure 6.4 and 6.5, it is indicated that the induced Lorentz force depends linearly on the velocity and the conductivity of the electrolyte as introduced in the section 1.1. The TFMS shows a good capability to measure the Lorentz force. Moreover, with the limited moving velocity up to 3.3 mm s^{-1} , the TFMS enables the force measurement on electrolyte with conductivity of 4.86 S m^{-1} . The experimental data presents the potential of the TFMS to measure with further extended range of conductivity down to 0.0064 S m^{-1} when the velocity is increased to 2.5 m s^{-1} , which is as an improvement from 0.059 S m^{-1} achieved in [29] with the similar velocity value. In comparison with the DFMS, the characteristics of the TFMS achieved in our work are presented in table 6.2.

Table 6.2: The TFMS as the newly developed force measurement system for LFV, in comparison with the previously developed differential force measurement system (DFMS).

	DFMS	TFMS
Force resolution	20 nN	2 nN
Settling time	1.4 s	9.2 s (in closed-loop)
Compensation force	EMF	EMF / ESF
Dead load capacity	Approximately 1 kg; theoretically up to 3 kg [27]	Over 3 kg; theoretically up to 10 kg [37]
Lorentz force measurement for electrolyte with conductivity down to:	0.059 S m^{-1} with velocity up to 2.5 m s^{-1}	0.0064 S m^{-1} with velocity 2.5 m s^{-1} (estimated from experimental data)

6.3 Summary

In this chapter, the practical measurements were implemented. Without pumping the liquid inside the channel, the semi-dry calibration is carried out with the experimental facility consisting of a plexiglass tube and a moving mechanism driven by a DC-motor. Different values of moving velocity as well as electrical conductivity were set in the measurement procedure. Because the velocity is limited up to 3.3 mm s^{-1} due to the moving mechanism, the conductivity is chosen as $\sigma = [4.86, 14, 20.4] \text{ S m}^{-1}$ in

our work, higher than that used in previous research [29], in order to achieve the Lorentz force in the range of nanonewton. During the measurement, procedures with and without motion were processed alternately with different duration to estimate and compensate the drift using the NPI in the data evaluation. In the measurement results, a good linear relationship between the induced force and the velocity as well as conductivity was indicated. The sensitivity of the TFMS to measure the velocity was obtained using the semi-dry calibration in respect to different conductivity values.

To summarize with table 6.2, for horizontal force measurement, the TFMS achieved a resolution of 2 nN by using NPI in the data evaluation. Moreover, the dead load capacity is improved to 3 kg (theoretically up to 10 kg due to the maximum load capacity of the flexible bearing). The dynamic behavior with the settling time of 9.2 s is also acceptable for the LFV application. According to the practical measurements on electrolytes, the TFMS enables force measurement for electrical conductivity of 4.86 S m^{-1} . When the velocity is increased from 3.3 mm s^{-1} to 2.5 m s^{-1} as the velocity that was arranged for measurements with DFMS, the TFMS shows the potential to implement measurements with even lower conductivity down to 0.0064 S m^{-1} , which is a great improvement compared to 0.059 S m^{-1} achieved in [29].

7. Conclusions and Outlook

The presented work aims to develop a high resolution force measurement system to contribute to the Lorentz force velocimetry application for velocity measurement of weakly conducting electrolytes.

Initially, the EMFC weighing cell as the core component of the previously developed FMSs is investigated. In previous work, the EMFC weighing cell was located in the suspended configuration carrying the 1 kg magnet system as the dead load, differing from its common usage as the balance. To study how the configurations and dead load values influence the measurement of the EMFC, the tilt sensitivity contributing to the measurement uncertainty and the stiffness determining the measuring sensitivity were tested in chapter 2. Experiments were carried out with the EMFC located on a tilt stage in four different configurations, and with different dead load values. The following points are concluded from chapter 2:

- To measure horizontally directed forces, the weighing cell in its sidewise configuration, suspended configuration with weighing pan upwards and with weighing pan downwards (figure 2.2) can be arranged. In each of the three configurations, linear relationship between the tilt sensitivity and the applied dead load was revealed;
- With the obtained linear relationship, the dead load value is determined, by which the tilt sensitivity was found to be zero. Therefore, a tilt-insensitive system can be theoretically achieved. In this way, the measurement uncertainty can be reduced (figure 2.5);
- In different configurations of the EMFC weighing cell, the stiffness of the system is different. Moreover, during the sidewise configuration, the stiffness is constant to the applied dead load values, while in the other three configurations the stiffness is further changed by changing dead loads (figure 2.9), which leads to the change in the measuring sensitivity of the system.

Although compensation weight can be manually applied to the EMFC weighing cell to achieve an insensitive system to the unavoidable tilt angles, with the necessity to carry the 1 kg magnet system, it is not generally desirable to apply the counterweight at such an order of magnitude on the precise mechanical structure of the weighing cell. Additionally, the stiffness of the EMFC is further increased by supporting the 1 kg magnet in the suspended configuration in work [27, 29], which makes the FMS less sensitive.

Considering the stiffness of the system is insensitive to the dead load in its sidewise configuration, as a transformation from the EMFC weighing cell in its sidewise configuration, the torsion force measurement system based on the principle of torsion balance was introduced in chapter 3. In the theoretical design concept, the symmetrical plane wheel carries the magnet system on one side and a non-magnetic dummy with a similar weight and geometrical parameters on the other side. A commercial flexible bearing hinge supports the plane wheel, enabling the rotation motion without friction and providing the elastic force balancing the external force. Rotation motion is detected by the optical positioning sensor with a compact size and providing sufficient resolution of 1 nm. Initial idea

of developing the torsion force measurement system is that the symmetrical geometry provides the equal arm lengths L_{T1} and L_{T2} , and with the similar weight of the dead load (magnet system and dummy) on each side, the precondition of a tilt-insensitive system is reached without applying additional compensation dead load in high magnitude. Theoretical calculations were made to design the system considering the following points:

- The geometrical parameters;
- The spring constant and maximum axial load of the flexible bearing given by the manufacturer;
- The resolution of the positioning sensor;
- The target force resolution of 2 nN.

By using a flexible bearing with the spring constant of $1.17 \cdot 10^{-2} \text{ N m rad}^{-1}$ (value given by manufacturer) and $L_{T1} = L_{T2} = 180 \text{ mm}$, R as the distance from the positioning sensor to the rotational axis is 135 mm, the stiffness of the system is 0.48 N m^{-1} and thereby the force resolution of 0.48 nN is calculated based on the theoretical calculations.

In chapter 4, the deflection method as a traceable method to perform the position calibration as well as force calibration was introduced by utilizing the tilt dependency of the system. Traceable tilt force caused by the tilt angle and standard mass piece was considered as the reference actuation force on the TFMS, by which the electrical voltage as the initial output of the positioning sensor was calibrated into rotational angles with the calibration factor $K_{ps} = 0.4207 \pm 0.0012 \text{ mrad V}^{-1}$ ($k = 2$), as well as into force values with $K_F = 30.07 \pm 0.23 \text{ } \mu\text{N V}^{-1}$ ($k = 2$). Because of the low stiffness and the high dead load, the natural frequency of the TFMS is low (0.06 Hz); and as an underdamped system with the damping ration of 0.0163, the cutoff frequency is as low as 0.002 Hz. The dynamic behavior is expected to be improved by setting up the closed-loop operation mode.

In chapter 5, the closed-loop operation mode was build up based on the PID-controller, where the force signal is no longer calculated from the voltage value using the force calibration factor K_F , but described by the compensation force which brings the deflection of the TFMS continuously back to the null position. The TFMS in its closed-loop operation mode was tested with the electromagnetic force as the compensation force provided by a commercial voice coil actuator. Then, a customized electrostatic force generator based on the structure of plate-shaped capacitor was introduced. Taking the whole TFMS as one conductor, a customized capacitor is built by assembling a PCB plate near the TFMS as the second electrode. Electrostatic force was generated between the two electrodes while actuation voltage is applied across them. Additionally, the calibration of the electrostatic force was implemented by using the following three methods (figure 5.6), they are:

- (a) By measuring the capacitance values with different distances between the two electrodes as a way to determine the capacitance gradient;
- (b) By comparing the electrostatic force with the electromagnetic force, which is calibrated using the deflection method and works as the reference force;
- (c) By setting the TFMS in a velocity mode, the calibration factor can be determined by measuring the induced current in the capacitor.

An agreement was presented by using the three calibration methods. With the lower uncertainty as well as minimal deviation from the theoretical calculation, the calibration factor determined by method

(a) is taken for further measurements. The customized capacitive actuator presented the ability to be used as a force generator. In the test of the dynamic behavior, the TFMS was tested in the open-loop and closed-loop with electromagnetic force as well as electrostatic force as the compensation force respectively. The dynamic behavior was improved as the cutoff frequency is increased to 0.1 Hz. Additionally, the electrostatic force operated at the same level as the electromagnetic force in the compensation procedure. As summarized in section 5.6, the customized capacitive actuator is a reasonable replacement of the commercial voice coil actuator with the following improvements:

- (1) More suitable for the LFV application where magnet system is involved;
- (2) No power wires connected to the rotational part of the TFMS;
- (3) Force constant K_{es} with lower relative uncertainty;
- (4) Force constant K_{es} can be adjusted by changing the geometry of the capacitor.

In the test of the force resolution, the newton's polynomial interpolation is introduced in the data evaluation to estimate and compensate the thermal and seismic drift and noises; the force down to 2 nN is resolved.

Lastly, the TFMS was involved in the Lorentz force measurement. The semi-dry calibration was introduced by using a tube to simulate the channel. With the liquid inside moving together with the tube driven by the moving mechanism, the flow channel is simulated with lower vibrations. In this experiment, the TFMS shows the good feasibility to measure the Lorentz force, which is linearly proportional to the velocity and conductivity. With a limited velocity up to 3.3 mm s^{-1} , the Lorentz force is measurable on electrolyte with conductivity down to 4.86 S m^{-1} . This shows the potential to extend the measurement range further down to 0.0064 S m^{-1} when the velocity is increased to 2.5 m s^{-1} , indicating the velocity arranged in work [29], where measurements on electrolytes with conductivity down to 0.059 S m^{-1} were achieved by the DFMS.

To conclude, as a newly developed FMS to measure the induced Lorentz force by weakly conducting electrolytes, the TFMS shows good capabilities with improved resolution, increased load capacity and multiple possibilities to perform actuation and compensation forces (table 6.2). Moreover, with easily commercially achieved components (flexible bearing, voice coil actuator, positioning sensor) and several customized components (PCB and capacitive actuator), the cost of the TFMS is also a great advantage compared to the EMFC weighing cell.

As mentioned in section 5.6, one of the future tasks is setting up the differential capacitive force actuator, with which the measuring range of the TFMS can be increased and the pre-voltage in the PID-controller is no more necessary.

Concerning that the semi-dry calibration was performed with limited velocity up to 3.3 mm s^{-1} in our work, the moving mechanism will be improved with the aim to increase the achievable moving velocity. This improvement can be based on changing the DC-motor and using a threaded shaft with larger pitch. However, because the motion period lasts 30 seconds during the measurement (figure 6.3), the velocity up to approximately 33 mm s^{-1} is thereby limited while implementing the semi-dry calibration on the tube with the limited length of 1000 mm. To overcome this limitation, the linear moving mechanism will be replaced by the rotating mechanism presented in figure 7.1, where the 1000 mm-long tube is replaced by an annular pipe. Similar to the tube presented in figure 6.2, the

annular pipe is filled with electrolytes and moves through the magnetic field. Moreover, the annular pipe is able to rotate continuously without considering the limitation of the stroke. Higher velocity values in the range of several meters per second can be thereby achieved, the velocity is dependent on the specifications of the motor, the dead load supported by the motor and also the diameter of the annular pipe (D_a in figure 7.1). With the new experimental facility, the semi-dry calibration can be implemented on electrolytes with further lower conductivity. Additionally, in order to reduce the environmental noise, a shell will be manufactured for the TFMS to improve the isolation from surroundings.

The second generation of the TFMS has already been developed and manufactured with a reduced geometry (270 mm x 45 mm x 60 mm). As another task in the further, the new TFMS will work together with the bulk superconductor as magnet system under cryogenic isothermal condition in a cryostat, with which high magnetic flux density is expected to be achieved. The feasibility to measure the Lorentz force using the second generation of the TFMS will also be tested on the experimental facility presented in figures 6.2 and 7.1.

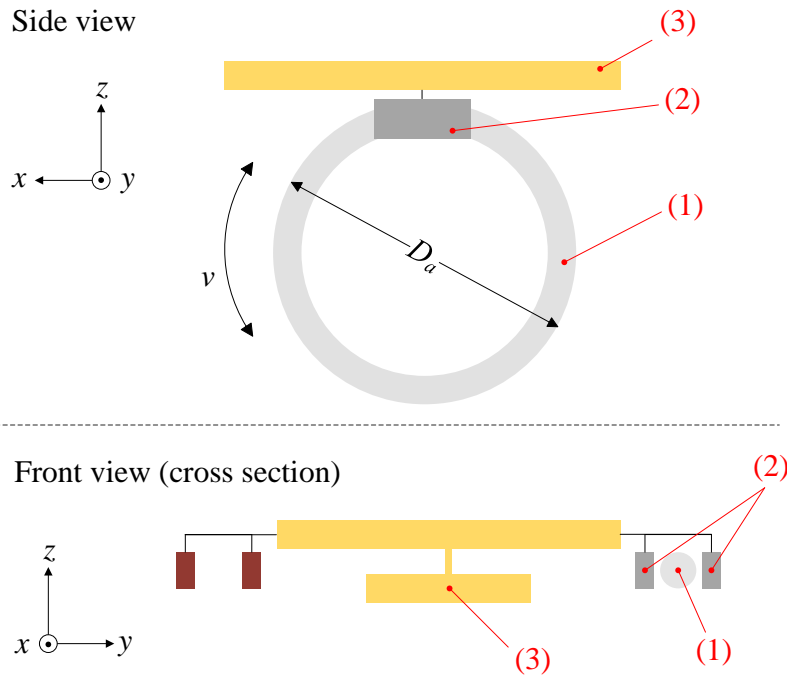


Figure 7.1: Replacement experimental facility with annular pipe to carry out semi-dry calibration. (1) Annular pipe; (2) Magnet system; (3) TFMS.

Appendix A Calibration of the NI9239

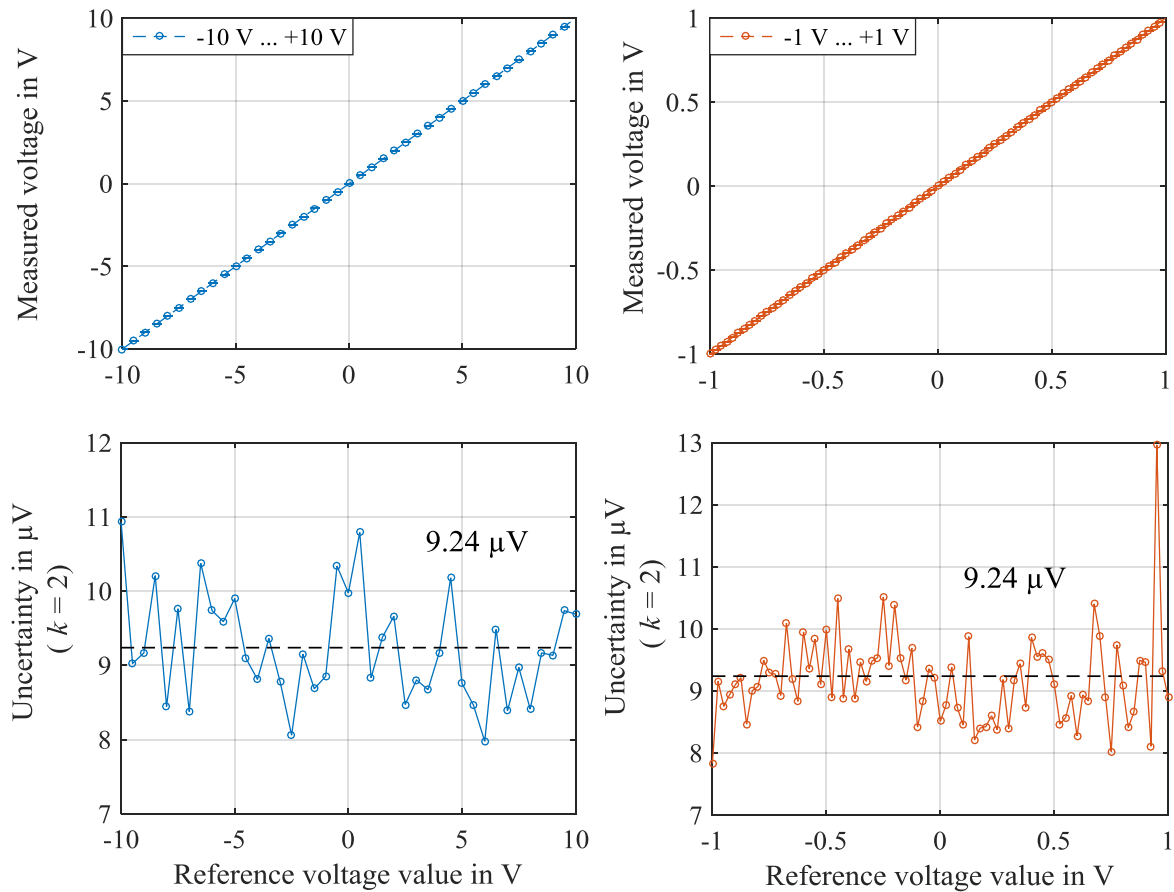


Figure A1: Calibration of the NI voltage module according to the reference voltage values provided by multi-function calibrator. Stepwise signals are generated in the range of ± 10 V (left, blue) and ± 1 V (right, red). At each step 9000 values are recorded during 30 minutes, from which the mean value and the uncertainty of the voltage step are determined. Then as shown in the two bottom figures, the mean value of the uncertainties of all the steps is calculated as $9.24 \mu\text{V}$ for each of the two measuring ranges.

Appendix B Geometrical parameters

Some geometrical parameters are indicated here for calculating the maximal and minimal achievable tilt angles of the TFMS working plane by using the adjustable feet.

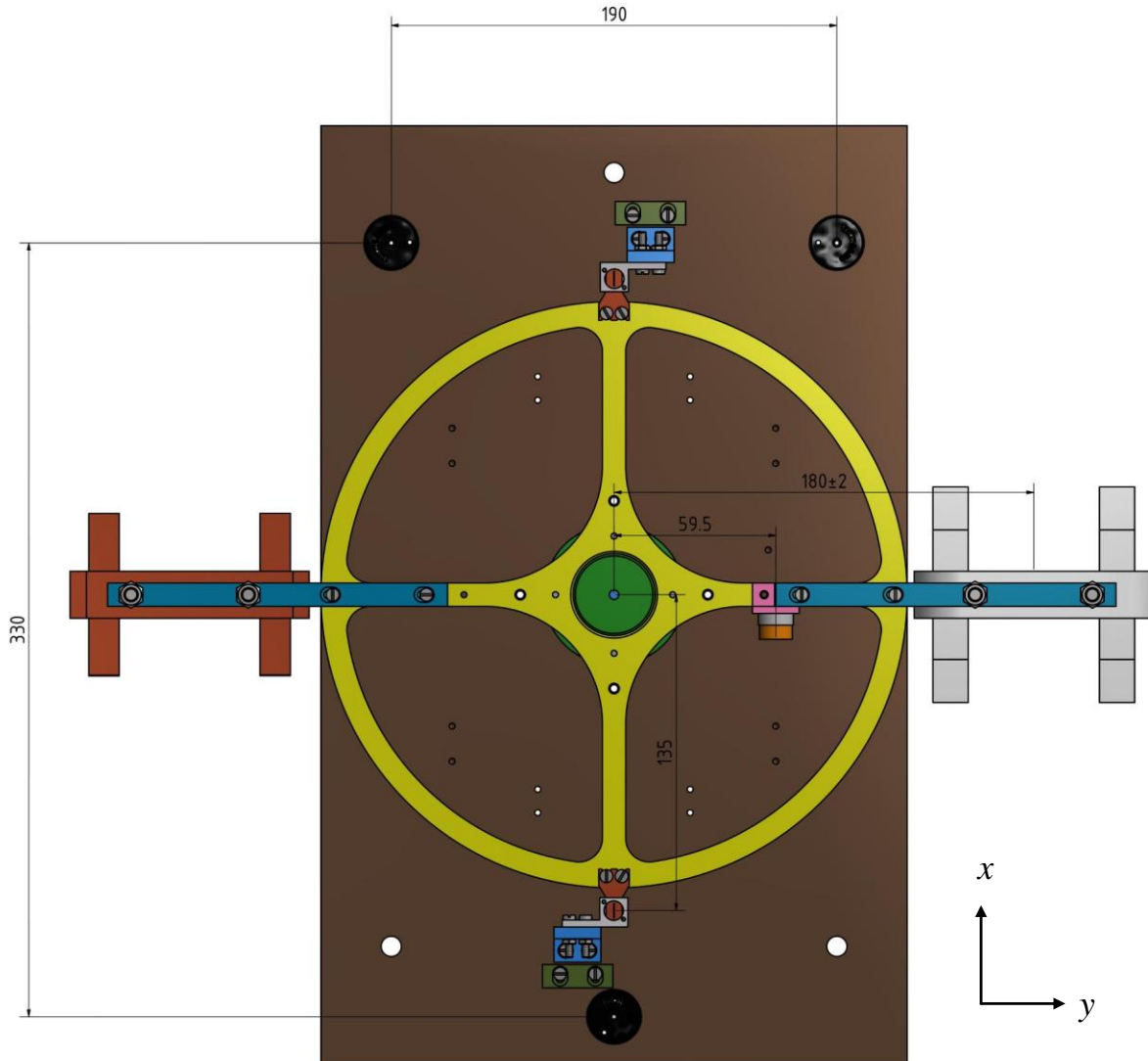


Figure B1: Some of the geometrical parameters of the TFMS, aiming to determine the achievable tilt angle by using the three adjustable feet.

The maximal achievable tilt angle around x -axis: $\alpha_{x_max} = \frac{50.8}{190} = 267 \text{ mrad}$

The maximal achievable tilt angle around y -axis: $\alpha_{y_max} = \frac{50.8}{330} = 154 \text{ mrad}$

Due to a full turn of the fine screws:

The minimal achievable tilt angle around x -axis: $\alpha_{x_min} = \frac{0.25}{190} = 1.32 \text{ mrad}$

The minimal achievable tilt angle around y -axis: $\alpha_{y_min} = \frac{0.25}{330} = 0.76 \text{ mrad}$

Further smaller tilt angles are achievable by turning the screws by $1/2$ turn and $1/4$ turn.

Bibliography

- [1] A. Thess, E. Votyakov, Y. Kolesnikov. Lorentz Force Velocimetry. *Phys. Rev. Lett*, 96 164501, 2006.
- [2] Y. Kolesnikov, C. Karcher, A. Thess. Lorentz force flowmeter for liquid aluminum: Laboratory experiments and plant tests. *Metallurgical and Materials Transactions B*, 42(3):441–450, 2011.
- [3] A. Wegfrass, C. Diethold, M. Werner, C. Resagk, T. Fröhlich, B. Halbedel, A. Thess. Flow rate measurement of weakly conducting fluids using Lorentz force velocimetry. *Measurement Science and Technology*, 23(10):105307, 2012.
- [4] C. Weidemann. Design and laboratory test of a Lorentz force flowmeter for pipe flows. *PhD thesis*, Technical University of Ilmenau, 2013.
- [5] C. Heinicke, A. Thess. Electromagnetic force on a magnetic dipole inside an annular pipe flow. *Physics of Fluids*, 25(9), 2013.
- [6] C. Heinicke, A. Thess, I. Rahneberg. Towards local resolution measurements in turbulent liquid metal duct flows. *Journal of Physics: Conference Series*, 318(7):072029, 2011.
- [7] B. Halbedel, C. Resagk, A. Wegfrass, C. Diethold, M. Werner, F. Hilbrunner, A. Thess. A novel contactless flow rate measurement device for weakly conducting fluids based on Lorentz force velocimetry. *Flow, Turbulence and Combustion*, 92(1-2):361–369, 2014.
- [8] A. Wegfrass, C. Diethold, M. Werner, T. Fröhlich, B. Halbedel, F. Hilbrunner, C. Resagk, A. Thess. A universal noncontact flowmeter for liquids. *Applied Physics Letters*, 100, 194103, 2012.
- [9] B. Hartmut, K. Porzig, J. Mengelkamp, M. Carlstedt, M. Ziolkowski, H. Toepfer. Lorentz force eddy current testing: a novel nde-technique. *COMPEL- The international journal for computation and mathematics in electrical and electronic engineering*, 33(6):1965–1977, 2014.
- [10] M. Werner. Design, Optimierung, Realisierung und Test von passive Magnetsystemen für die Lorentzkraftanemometrie an Electrolyten. *PhD thesis*, Technical University of Ilmenau, 2013.
- [11] I. Sokolov, Y. Kolesnikov, A. Thess. Experimental investigation of the transient phase of the lorentz force response to the time-dependent velocity at finite magnetic Reynolds number. *Measurement Science and Technology*. 25(12):125304, 2014.
- [12] J. R. Pratt, J. A. Kramar, D. B. Newell, D. T. Smith. Review of SI traceable force metrology for instrumented indentation and atomic force microscopy. *Measurement Science and Technology*. 16 2129–2137, 2005.

- [13] D. B. Newell, J. A. Kramar, J. R. Pratt, D. T. Smith, E. R. Williams. The NIST Microforce Realization and Measurement Project. *IEEE Transactions on Instrumentation and Measurement*, 52:508, 2003.
- [14] G. A. Shaw, J. Stirling, J. A. Kramar, A. Moses, P. Abbott, R. Steiner, A. Koffman, J. R. Pratt, Z. J. Kubarych. Milligram mass metrology using an electrostatic force balance. *Metrologia*, 53 A86-A94, 2016.
- [15] R. Leach, D. Chetwynd, L. Blunt, J. Haycocks, P. Harris, K. Jackson, S. Oldfield, S. Reilly. Recent advances in traceable nanoscale dimension and force metrology in the UK. *Measurement Science and Technology*, 17 467-476, 2006.
- [16] J Stirling, G. A. Shaw. Realising traceable electrostatic forces despite non-linear balance motion. *Measurement Science and Technology*, 28-055003, 2017.
- [17] M. Kim, J. R. Pratt, U. Brand, C. W. Jones. Report on the first international comparison of small force facilities: a pilot study at the micronewton level. *Metrologia*, 49-1, 2011.
- [18] L. Song, Y. Zheng, G. Hu, J. Ma, T. Werner, M. Zhao, F. Fang. Highly sensitive, precise, and traceable measurement of force. *Instrumentation Science and Technology*. 44, NO.4,386-400, 2016.
- [19] C. Diethold, M. Kühnel, T. Ivanov, I. W. Rangelow. T. Fröhlich. Determination of AFM-Cantilever spring constants using the TU Ilmenau force displacement measurement device. In *Proceedings of the XXI IMEKO world Congress*, S.175-180, 2015.
- [20] M. Kühnel, M. Rivero, C. Diethold, T. Fröhlich. Precise tiltmeter and inclinometer based on commercial force compensation weigh cells. In *Proceedings of IMEKO International TC3, TC5 & TC22 Conference*, 2014.
- [21] T. Quinn, C. Speake, H. Parks, R. Davis. The BIPM measurements of the Newtonian constant of gravitation, *G. Philosophical Transactions of the Royal Society A*, 372:2014032, 2014.
- [22] S. J. Chen, S. S. Pan. Nanonewton Force Generation and Detection Based on a Sensitive Torsion Pendulum. *IEEE Transactions on Instrumentation and Measurement*, 58-4, 2009.
- [23] T. A. Wagner. Rotating Torsion Balance Tests of the Weak Equivalence Principle. *PhD thesis*, University of Washington, 2014.
- [24] S. Schlamminger. Determination of the Gravitational Constant using a Beam Balance, *PhD thesis*, University of Zürich, 2002.
- [25] H. V. Parks, J. E. Faller. Simple Pendulum Determination of the Gravitational Constant. *Physical Review Letters*, 105, 110801, 2010.
- [26] V. Nesterov, M. Mueller, L.L. Frumin, U. Brand. A new facility to realize a nanonewton force standard based on electrostatic methods. *Metrologia*, 46 277-282, 2009.

- [27] C. Diethold. Lorentzkraft-Anemometrie von elektrisch schwach leitfähigen Fluiden. *PhD thesis*, Technical University of Ilmenau, 2015.
- [28] P. Sun, M. Zhao, J. Jiang, Y. Zheng, Y. Han and L. Song. The Differential Method for Force Measurement Based on Electrostatic Force. *Journal of Sensors*, 1857920, 2017.
- [29] S. Vasilyan. High Precision Force Measurements in Horizontal Direction in Combination with High Dead Loads: Non-contact Flowmeter for Low Conducting Electrolytes. *PhD thesis*, Technical University of Ilmenau, 2015.
- [30] S. Vasilyan, M. Rivero, J. Schleichert, B. Halbedel, T. Fröhlich. High-precision horizontally directed force measurements for high dead loads based on a differential electromagnetic force compensation system. *Measurement Science and Technology*, 27-045107, 2016.
- [31] S. Vasilyan, R. Ebert, M. Weidner, M. Rivero, B. Halbedel, C. Resagk, T. Fröhlich. Towards metering tap water by Lorentz force velocimetry. *Measurement Science and Technology*, 26-115302, 2015.
- [32] S. Vasilyan, T. Fröhlich. Direct Lorentz force compensation flowmeter for electrolytes. *Applied Physics Letters*, 105,223410, 2014.
- [33] M. Kühnel, M. Rivero, C. Diethold, F. Hilbrunner, T. Fröhlich. Dual axis tiltmeter with nano resolution based on commercial force compensation weigh cells. In *Proceedings of 58th Ilmenau Scientific Colloquium*, 2014.
- [34] **N. Yan, S. Vasilyan, M. Kühnel, T. Fröhlich. Investigation to the tilt sensitivity of the Lorentz force velocimetry system for the flow rate measurement of low conducting fluids. In Proceeding of IMEKO TC3, TC5 and TC22 Conferences, 2017.**
- [35] M. Rivero, M. Kühnel, T. Fröhlich. High precision dual axis tilt stage. In *Proceedings of 58th Ilmenau Scientific Colloquium*, 2014.
- [36] H. Cavendish. Experiments to determine the Density of the Earth. *Phil. Trans. R. Soc. Lond*, vol. 88 469-526, 1798.
- [37] C-Flex Bearing. Design Guide: <https://c-flex.com/pivot-bearings/design-guide/> (accessed 29. Oct. 2018).
- [38] C. Diethold, T. Fröhlich, F. Hilbrunner, G. Jäger. High precision optical position sensor for electromagnetic force compensated balances. In *Proceeding of IMEKO TC3, TC5 and TC22 Conferences*, 2010.
- [39] Datasheet analoge input module NI9239: http://www.ni.com/pdf/manuals/375939b_02.pdf (accessed 29. Oct. 2018).
- [40] Haag-Streit AG, Elcomat 3000: <https://www.haag-streit.com/de/moeller-wedel-optical/produkte/elektronische-autokollimatoren/elcomat-reihe/elcomat-3000/> (accessed 29. Oct. 2018).

- [41] N. Yan, M. Kühnel, S. Vasilyan, T. Fröhlich. **Torsion balance-based system for high-precision force measurement in horizontal plane; part I. Development concept.** *Measurement Science and Technology*, 29 084001, 2018.
- [42] Organisation Internationale de Métrologie Légale 2004 Weights of classes E₁, E₂, F₁, F₂, M₁, M₁₋₂, M₂, M₂₋₃ and M₃, Internal Recommendation OIML R111-1
- [43] Result of the absolute gravitational acceleration measurement at the Technical University of Ilmenau.
- [44] N Yan, M. Kühnel, S. Vasilyan, T. Fröhlich. **Calibration of the torsion force measurement system for the Lorentz force velocimetry application.** In *Proceedings of 59th Ilmenau Scientific Colloquium*, 2017.
- [45] Datasheet linear voice coil motor: <http://moticont.com/pdf/lvcm-016-010-01.pdf> (accessed 29. Oct. 2018).
- [46] Datasheet Universal source 3245A: <http://www.testequipmenthq.com/datasheets/Agilent-3245A-Datasheet.pdf> (accessed 29. Oct. 2018).
- [47] C. Diethold, F. Hilbrunner. Force measurement of low forces in combination with high dead loads by the use of electromagnetic force compensation. *Measurement Science and Technology*, 23 074017, 2012.
- [48] O V. Vakaliuk, M D. Ainslie, B. Halbedel. Lorentz force velocimetry using a bulk HTC magnet system: proof-of-concept. *Supercond. Sci. Technol.* 31 084003. 2018.
- [49] Data sheet HIOKI Impedance analyzer IM3570: <https://www.hioki.com/file/cmw/hdCatalog/4765/pdf/?action=browser&log=1&lang=en> (accessed 29. Oct. 2018).
- [50] F. Hilbrunner, I. Rahneberg, T. Fröhlich. Wattwaage mit Hebelübersetzung auf Basis eines kommerziellen EMK-Wägesystems. *Technisches Messen*, 2196-7113, 2017.
- [51] J. Lunze. Regelungstechnik 1. Springer Vieweg, ISBN 978-3-642-29533-1, 2014.
- [52] S. Davidson, M. Perkin, M. Buckley. The Measurement of Mass and Weight. *Measurement Good Practice Guide No.71*. 2004.
- [53] Hamming R.W. Numerical Methods for Scientist and Engineers Dover Publications. Inc., New York, ISBN 0-486-65241-6, 1962.
- [54] Y. Zheng, M. Zhao, P. Sun, L. Song. Optimization of Electrostatic Force System Based on Newton Interpolation Method. *Journal of Sensors*. Article ID 7801597, 2018
- [55] S. Chen, S Pan. A force measurement system based on an electrostatic sensing and actuating technique for calibrating force in a micronewton range with a resolution of nanonewton scale. *Measurement Science and Technology*, 22 045104, 2012.

- [56] A. Wegfraß. Experimentelle Untersuchungen zur Anwendbarkeit der Lorentzkraft-Anemometrie auf schwach leitfähige Fluid. *PhD thesis*, Technical University of Ilmenau, 2013.
- [57] THORLABS fine Hex Adjuster:
https://www.thorlabs.com/newgrouppage9.cfm?objectgroup_id=1205 (accessed 29. Oct. 2018).
- [58] V. Minchenya, C. Karcher, Y. Kolesnikov, A. Thess. Dry calibration of the Lorentz force flowmeter. *Magnetohydrodynamics* Vol.45. pp 569-578, 2009.
- [59] Datasheet Brushless DC-Servomotor:
https://www.faulhaber.com/fileadmin/Import/Media/EN_3056_B_FMM.pdf (accessed 29. Oct. 2018).
- [60] Conductivity ordering guide:
<http://myweb.wit.edu/sandinic/research/conductivity%20v%20concentration.pdf> (accessed 29. Oct. 2018).

Erklärung

Ich versichere, dass ich die vorliegende Arbeit ohne unzulässige Hilfe Dritter und ohne Benutzung anderer als der angegebenen Hilfsmittel angefertigt habe. Die aus anderen Quellen direkt oder indirekt übernommenen Daten und Konzepte sind unter Angabe der Quelle gekennzeichnet.

Bei der Auswahl und Auswertung folgenden Materials haben mir die nachstehend aufgeführten Personen in der jeweils beschriebenen Weise unentgeltlich geholfen:

- **Prof. Dr.-Ing. habil. Thomas Fröhlich** --- Fachliche Betreuung während der Promotionszeit.
- **Dr.-Ing. Suren Vasilyan** --- Vorstellung des FMSs und Strömungskanals (entwickelt und verwendet von den ersten und zweiten Generationen des Projektes Lorentz Force Velocimetry and Lorentz Force Eddy Current Testing) im Jahr 2016 beim Beginn dieser Arbeit.
- **M. Sc. Ivan Horodyskyi** --- Studentische Hilfskraft: Durchführung der Messungen in Abschnitten 4.1 und 4.2.
- **Frau Mengchen Yan** --- Sprachkorrektur; Ausschließlich Bearbeitung von Rechtschreibung und Grammatik. Es wurden keine inhaltlichen Änderungen, Ergänzungen oder weitere Beiträge durch sie vorgenommen

Weitere Personen waren an der inhaltlich-materiellen Erstellung der vorliegenden Arbeit nicht beteiligt. Insbesondere habe ich hierfür nicht die entgeltliche Hilfe von Vermittlungs- bzw. Beratungsdiensten (Promotionsberater oder anderer Personen) in Anspruch genommen. Niemand hat von mir unmittelbar oder mittelbar geldwerte Leistungen für Arbeiten erhalten, die im Zusammenhang mit dem Inhalt der vorgelegten Dissertation stehen.

Die Arbeit wurde bisher weder im In- noch im Ausland in gleicher oder ähnlicher Form einer Prüfungsbehörde vorgelegt.

Ich bin darauf hingewiesen worden, dass die Unrichtigkeit der vorstehenden Erklärung als Täuschungsversuch bewertet wird und gemäß § 7 Abs. 10 der Promotionsordnung den Abbruch des Promotionsverfahrens zur Folge hat

Ilmenau, 05.11.2018

Na Yan